ENERGY DISSIPATION IN ORTHOGONAL ULTRAPRECISION MACHINING OF GERMANIUM

By

CHARLES G. BABCOCK

Bachelor of Science

Oklahoma State University

Stillwater, Oklahoma

1992

Submitted to the Faculty of the
Graduate College of the
Oklahoma State University
in partial fulfillment of
the requirements for
the Degree of
MASTER OF SCIENCE
July, 1995

ENERGY DISSIPATION IN ORTHOGONAL ULTRAPRECISION MACHINING OF GERMANIUM

Thesis Approved:

Don A. Lucca
Thesis Adviser

C E Quine

10 Spitler

Thomas C. Collins
Dean of the Graduate College

ACKNOWLEDGMENTS

I express my deep gratitude and appreciation to my advisor Dr. D. A. Lucca for his guidance, support (both monetary and personal) and encouragement. My sincere appreciation also goes to Dr. Yongwie Seo for his kind attention, friendship, and invaluable help with far too many things to list here, and to the irrepressible Dr. C. E. Price for his advice, support, and for serving on my committee. I also express my humble appreciation to Dr. Jeff Spitler for being kind enough to serve on my committee.

I thankfully acknowledge Dr. R. Komanduri for allowing access to his SEM and Mr. Johnny Hixson for his kind help in using the instrument. Special thanks to my longtime friend, Ms. Leah Zachary, for editing help and matters of English. Thank you also to my colleagues who have provided their help in one way or another over the course of this work (e.g., Jonathan Jones, Jean Zoppe, N. Moss and Craig Dickson).

I would like to extend a special thanks to the many friends and family members who have provided me with their support, encouragement and love; especially my mother Susan Babcock, my father Stewart Goldsmith, my grandmother Marie Mathews, and my friends Craig Ware, Mark Mitchell, and Jeff and Amy Ferguson.

This work has been supported in part with funding from the National Science Foundation, Division of Design and Manufacturing Systems, and the Oklahoma Center for the Advancement of Science and Technology.

TABLE OF CONTENTS

LIST OF TABLES

LIST OF FIGURES

Nomenclature

R_a	roughness average
RMS	root mean square
t_o	uncut chip thickness
α	rake angle
r_e	tool edge radius
F_c	cutting force
F_t	thrust force
θ	direction of resultant force vector

CHAPTER I

INTRODUCTION

1.1 Problem Definition

Manufacturing processes that can produce accurate form and finish on micron and submicron scales are essential. Processes fulfilling these criteria are called ultraprecision engineering, where the term 'ultraprecision' refers to the highest dimensional accuracy that can be achieved, relative to the capabilities at a given time. Perhaps, the most important such process for attaining high form and finish accuracy at a submicron scale is 'ultraprecision' machining, where form accuracies on the submicron level and surface roughnesses in the nanometer range can be produced [Lucca and Seo 1993, Taniguchi 1983, Seo 1993, Ikawa et al. 1991].

Further improvement in ultraprecision machining is dependent on our ability to understand the fundamental behavior of the process. The process physics, at very small uncut chip thicknesses, is not well understood. Most of the current research has dealt with ductile materials such as copper and aluminum, with only cursory attention being paid

to other less traditional materials. Brittle materials, for the most part, have been neglected.

Topics that have been researched using ductile materials are energy dissipation in ultraprecision machining, the effect of the tool edge profile during the machining process, effect of cutting speed, temperature effects due to the process, the behavior of forces as a function of uncut chip thickness, and the depth of the subsurface damaged layer.

Some studies using brittle materials are investigations into the crystal orientation dependence of machining damage by Blackley and Scattergood [1990], single point diamond turning of glasses by Puttick et al. [1989], and the effect of material properties on the process by Furukawa [1988]. Other works include that presented by Nakasuji et al. [1990] who published investigations on the diamond turning of brittle materials, the documentation of the apparent ductile transition in the facing of Si by Taylor et al. [1987], as well as Blake and Scattergood's study of ductile regime machining of Ge and Si [1990].

Most studies have utilized a three dimensional cutting geometry, such as facing. This type of geometry does not allow for the isolation of the force system and makes determination of the uncut chip thickness problematic. These are necessary data for determining the process energies and isolating the effects of parameters such as the tool edge profile and cutting speed. These are important for determining the fundamental process physics at very small uncut chip thicknesses where, unlike traditional cutting, sliding at the flank face and plowing at the tool edge have been cited as dominate mechanisms rather than conventional chip formation [Moriwaki 1989, Lucca and Seo 1991]. Using an orthogonal cutting geometry results in a two dimensional stress state

which allows the force system to be isolated and its components accurately measured, as well as ensuring a constant uncut chip thickness. This is the same technique used by Lucca and Seo [1991] in their studies of energy dissipation in ultraprecision machining of oxygen free high conductivity (OFHC) copper.

Data, where the forces generated at a known uncut chip thickness are known, have not been presented for brittle materials. This lack of accurate force data prevents the development of stress models for the cutting process. The aim of the research reported here is to conduct energy dissipation experiments using a brittle rather than a ductile material. Germanium has been selected as the material for the experiments because of its use for infrared optical components, which provides a frame of reference whereby the results of the research achieve both a practical as well as a theoretical relevance.

1.2 Background

To date, there have been significant contributions by Donaldson et al. in the area of chip science and by Ikawa et al. on the effects of the diamond tool on the process [Lucca and Seo, 1991]. Moriwaki [1989] has reported findings on the machinability of copper in ultraprecision machining and presented work in which he proposed a conceptual model for low uncut chip thicknesses. In Moriwaki's model, the material is pushed with a large negative rake angle, which results in a process dominated by plastic deformation associated with rubbing or burnishing of the surface rather than by chip formation, as shown in Figure 1. This occurs when the relative size of the tool edge is large as

compared with the uncut chip thickness, such that even a very sharp tool appears blunt. His experimental results suggest that the transition from a conventional chip removal process to a plastic deformation dominated process takes place at a uncut chip thickness on the order of 0.1 μm.

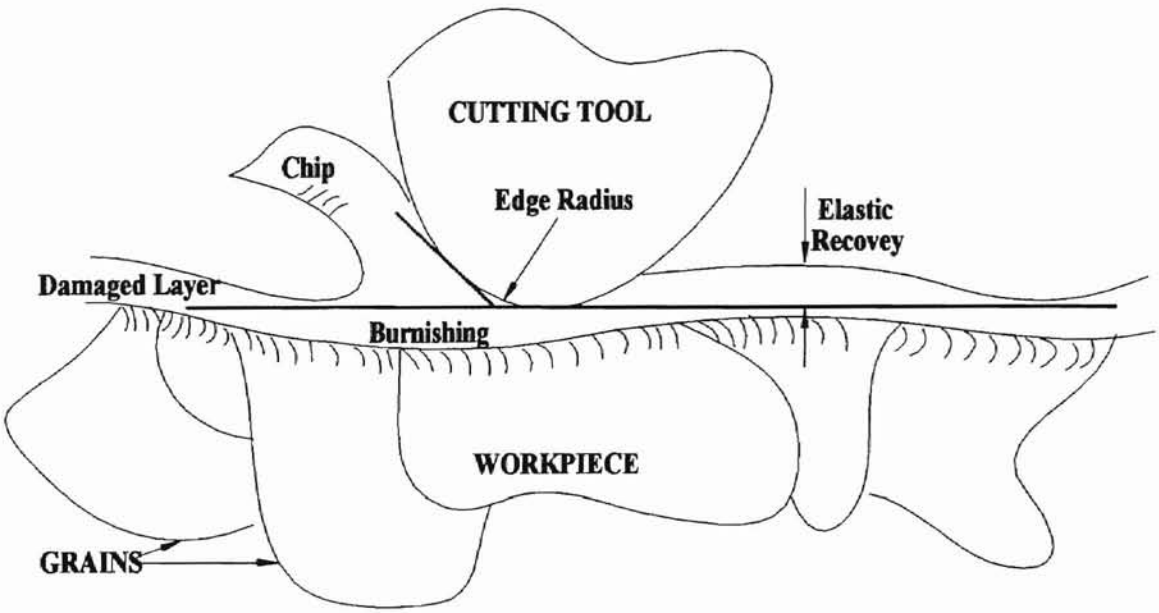

Figure 1. Moriwaki's conceptual model for machining at low uncut chip thicknesses. Note how the effective, negative rake angle pushes rather than cuts the material. Elastic recovery behind the tool nose leads to a portion of the tool acting as a slider along the workpiece surface.

Lucca and Seo [1993] established the tool edge size effect in ultraprecision machining. While their work does not prove the dominant mechanism, their data provided significant evidence that a different mechanism is dominant at very low uncut chip thicknesses. They found that an overall energy balance indicated that shearing in the shear zone, a process responsible for as much as 80% of the energy dissipated in conventional cutting, was unable to account for the observed energies. These phenomena were

consistent with plowing at the tool edge and sliding at the tool workpiece interface (due to elastic recovery) which accounts for a significant portion of dissipated energy and, hence, the higher observed values for forces and energies. Lucca and Seo [1993] have also pointed out the significance of the tool edge profile in determining machining behavior. They have shown that macroscopically similar tools with differing tool edge profiles provided significantly different forces and energies during machining.

Furukawa [1988] has shown the effects of material properties, such as workpiece structure, on ultraprecision machining. He established that a significant difference exists in the behavior of polycrystalline, single crystal, and amorphous materials and has determined the effect of grain boundaries on microcutting behavior. He, also, showed that the assumption of macroscopic properties consistent with the continuum mechanics approach is not valid in the ultraprecision machining of polycrystalline materials. Because, as the length scale of the process is reduced, the uncut chip thickness approaches the grain size of the material, and the material encountered by the tool becomes a series of single crystals of varying orientation, rather than a homogeneous continuum. Other studies have reported on the partition of energies in the process [Lucca and Seo, 1989], aspects of surface generation such as the depth of the plastically deformed layer at the workpiece surface [Lucca and Seo, 1994], and issues regarding tool edge characterization [Lucca and Seo, 1993]. Also noteworthy is work presented on the mechanisms of microchip formation [Nishiguchi et al, 1988], the effect of crystallographic orientation on chip formation [Lee and Zhou, 1992], and tool wear in the single point diamond turning of aluminum [Sugano et al, 1987].

Critical work in the ultraprecision machining of brittle materials has been done, most notably that by Blake [1990], Blackley and Scattergood [1990], Puttick et al. [1989], Furukawa [1988], Taylor et al. [1987], and Nakasuji et al. [1990]. Each of these studies addresses the apparent ductile behavior at low uncut chip thicknesses of otherwise brittle materials. This phenomenon had been in evidence as long as forty-five years when E. W. Taylor [Puttick, 1989] made apparently crack free scratches in glass in 1949. Among others to note the apparent transition between brittle and ductile behavior were Taylor and colleagues [1987] who noted the ostensible brittle-ductile transition in the facing of single crystal Si and characterized the transition in terms of the surface quality of the Si. Examination along the shoulder of a cut, resulting from interrupted machining, revealed a severely fractured area at the shoulder which transitioned to a much smoother, less damaged surface at the tool nose. This transition, from damaged to undamaged behavior, was taken to indicate a change in removal mechanism from fracture dominate to deformation dominate.

Blackley and Scattergood [1990] showed the dependence of machining damage on crystal orientation of Ge and proposed a simple force system model to explain and predict the orientation dependence of the damage. They performed face cutting experiments on single crystal wafers of Ge that were in good agreement with predicted results. They concluded that fracture damage was the result of tensile stresses behind the tool tip and that the orientation dependence could be attributed to the amplitude of these resolved tensile stresses on the cleavage plane of the material.

Nakasuji [1990] proposed a model for the brittle to ductile transition in chip formation and a parameter for determining brittle mode behavior. He took into account the effect of resolved stresses on the cleavage plane, as well as the material's relative defect density and the relative size of the stress field at the tool tip. The major difference between the models of Blackley and Nakasuji is the roll of the critical stress field and the relative defect density in the latter's work. Nakasuji pointed out that as the volume of material removed decreases (and hence as the uncut chip thickness decreases) the relative incidence of defects encountered by the stress field at the tool tip also decreases. With fewer defects present to be encountered by the stress field and hence initiate fracture, plastic deformation becomes more likely (Figure 2). The relative size of the stress field also plays an important role; at low uncut chip thickness, the stress field is small and therefore less likely to encounter defects and initiate fractures.

The role of the volume size effect in ultraprecision machining was one of the focuses of the work of Puttick et al. [1989]. They suggested that "brittle-ductile transitions were the result of size effects due to the nongeometrical scaling laws of brittle fracture." They proposed that below a critical dimension of stressed volume of material, yielding rather than fracture would occur and that this critical dimension was a function of the elastic modulus and yield stress of the material and the specific work per unit area required to propagate a crack. Their criteria were validated for several situations including compression and indentation. They used this relationship to make an order of magnitude prediction of the critical depth of cut in the single point diamond machining of glasses with a Vickers indenter.

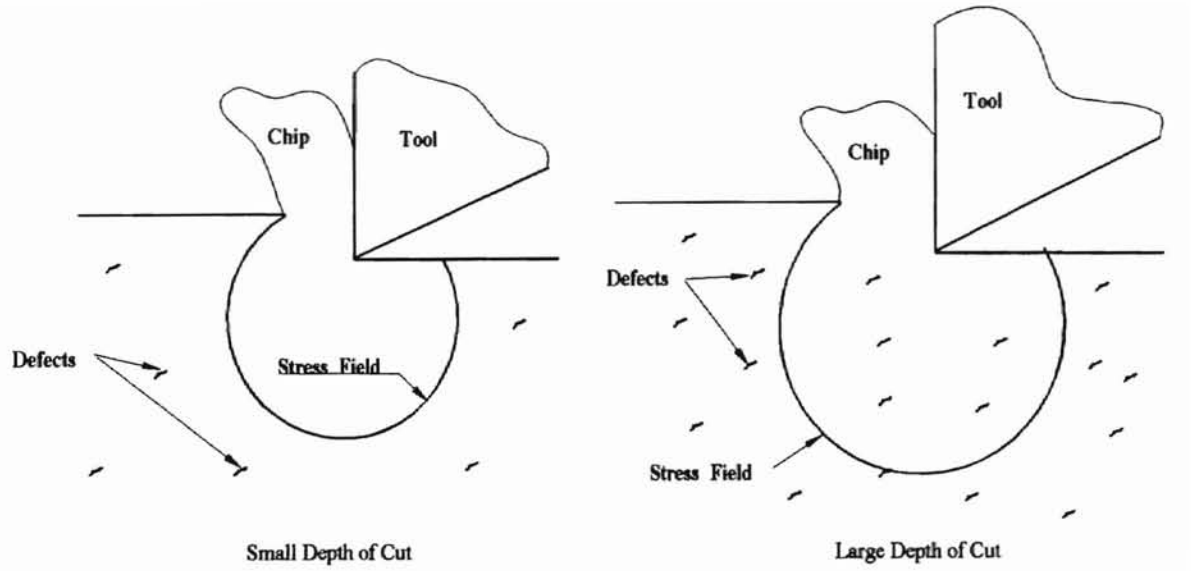

Figure 2. Illustration showing the effect of defect density. Small DOC's produce correspondingly small stress fields. If the stress field is small enough and the defect density is low, then the likelihood of the stress field encountering defects is very small and hence the possibility of initiating fractures is low. Contrast this with the case for large uncut chip thicknesses where the larger stress field greatly increases the possibility of initiating fractures.

The importance of the volume size effect was noted by Blake and Scattergood [1990], who presented work on ductile-regime machining of Ge and Si. They investigated the ductile-regime in ultraprecision machining and used a critical depth parameter for determining where the transition from ductile material removal to fracture material removal would take place. The critical depth parameter was a function of the material's hardness, fracture toughness, and elastic modulus, and was developed from principles for indention fracture mechanics. Here, again, the argument for ductile behavior is integral to the concept of the volume scale effect for fracture initiation. Plastic deformation energy scales with volume, while fracture energy scales with crack surface area; hence plastic deformation becomes favorable as the scale of deformation decreases. Eventually, a threshold volume is reached where the material will plastically deform but not fracture.

Furukawa [1988] reported work on the effect of material properties on ultraprecision machining, which included both ductile and brittle materials. He suggested the dependence of the process behavior on the crystallographic orientation of the workpiece, in addition to establishing the effect of grain boundaries on ultraprecision machining. This is not surprising, since it is well known that single crystal materials exhibit considerable anisotropic behavior.

CHAPTER II

EXPERIMENTAL CONFIGURATION FOR THE STUDY OF ORTHOGONAL FLYCUTTING OF SINGLE CRYSTAL GERMANIUM

2.1 Introduction

The objective of this work was to obtain accurate thrust and cutting force data for the condition of orthogonal ultraprecision machining of Ge. Cutting and thrust forces are of primary importance because they are direct indicators of the governing physical phenomena. Information was also collected to establish the surface quality of the machined specimens. Tool edge characterizations were performed to determine the tool edge radius and profile, and chips were collected and studied to catalogue the morphologies encountered during the experiments. In this chapter, the experimental setup for studying orthogonal flycutting of single crystal Ge is described including descriptions of the tool, workpiece, machine tool, surface characterization equipment, and data acquisition system.

Although most practical cutting operations utilize a three dimensional cutting geometry, they are also very complicated and thus difficult to study. Utilizing a two dimensional cutting geometry allows for the isolation of cutting and thrust forces and a more accurate assessment of the uncut chip thickness, thereby making the process much easier to analyze and quantify. Flycutting was selected over plunge cutting because it allowed for more accurate force measurement [Seo, 1993].

2.2 Experimental Setup

The same experimental configuration reported by Lucca and Seo [1991, 1993] is used except for changes made to account for brittleness of the Ge, e.g., the specimen holding configuration was changed since clamping the Ge coupons caused them to fracture. Throughout the experiments, a Rank Pneumo diamond turning machine was used. Several of the fixtures employed for holding the tool and workpiece had to be designed and fabricated; these consisted of an aluminum chuck plate, a workpiece holder, a tool holder, a dynamometer holding block, and a specimen coupon holder. The setup used for the experiments is shown in Figure 3.

The single crystal, flat nosed diamond tool was clamped into the tool holder which was in turn bolted to the aluminum chuck plate such that the tool sat 76.2 mm off of the spindle axis. The chuck plate was held by the vacuum chuck and covered its entire face thereby ensuring the maximum holding force. For this cutting geometry and setup, the tool rotated while the workpiece remained stationary. Rotation of the spindle provided

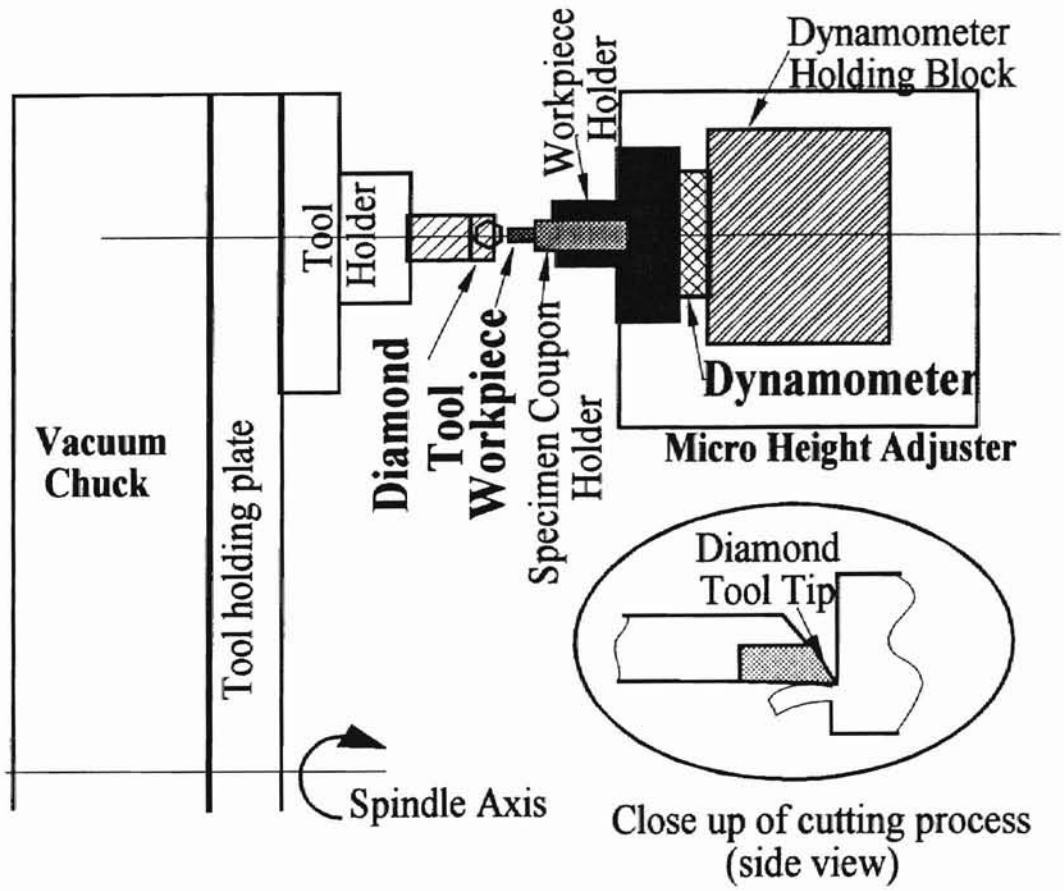

Figure 3. Schematic of the experimental setup used for orthogonal flycutting of Ge.

the desired cutting motion while constant z-axis motion or infeed produced the required uncut chip thickness. The constant infeed ensured a known uncut chip thickness independent of any elastic recovery behind the tool edge. The rectangular workpiece was held in the specimen coupon holder with a hard wax. The specimen coupon holder was clamped in the workpiece holder which was in turn clamped directly to the dynamometer and dynamometer holding block using a dynamometer clamping bolt. This allowed for the direct measure of the two dimensional force components during the flycutting operation. The force signals from machining were sent into a set of amplifiers, one for each component, and from there sent to the oscilloscope for storage and processing. The

interrupted nature of the cutting process avoided any problems associated with the DC drift of the force signals during cutting by providing a constant zero force base line. This setup afforded the orthogonal flycutting of a stationary workpiece and the acquisition of cutting and thrust force data from the machining process [Seo, 1993].

Characterizations of the machined surfaces were done using a Zygo laser interferometric microscope and in some cases a Nikon optical microscope. Chips collected during the machining process were studied using scanning electron microscopy. Prior to machining, the single crystal diamond tool was characterized using atomic force microscopy to determine the tool edge radius and profile. The procedure and characterization were done according to Lucca and Seo [1994].

2.3 Diamond Turning Equipment

2.3.1 Machine Tool

A submicron diamond turning and grinding machine, Rank Pneumo Model ASG-2500, was used for all of the machining experiments in this study. Appropriate features and specifications for turning are listed below in **Table 1** .

TABLE 1: FEATURES AND CAPABILITIES OF THE ASG-2500 SUBMICRON DIAMOND TURNING AND GRINDING MACHINE[1]

Description		Feature/Capability
Control System		Allen Bradley Series 8200 CNC
System Resolution		10 nm (0.4 μin)
Vibration Isolation		Passive Air Isolator (3 points)
Feedback System (Closed Loop)		Hewlett Packard Model 5518 Laser Interferometer
Slideways	Design Slideway Travel Spindle Travel Velocity	Hydrostatic Oil Bearing 254 mm (10 in) 152 mm (6 in) 0.25~760 mm/min. (0.01~30 in/min.)
Spindle	Design RPM Range Load Capacity	Air Bearing 100~2400 450 N (100 lb.)
Maximum Workpiece Dimensions	Diameter Length	304 mm (12 in) 152 mm (6 in)
Required Utilities	Air Supply Electrical Power	0.7 MPa (100 psi); 15 CFM 230 VAC; 3 KVA
Required Floor Space		1.83 x 2.74 m (72 x 108 in)

2.3.2 Diamond Tool

A flat nosed, single crystal diamond tool made by Norton Co. was used in the experiment. The diamond was vacuum brazed to a carbon steel shank. The diamond tool edge was approximately 2 mm in length with a gross tool edge radius, r_e, of 0.23μm and an as measured edge radius of 60-70 nm. The tool had a nominal rake angle, α, of 0.5°. The diamond was oriented so that rake face was a (110) plane with a (100) plane parallel

[1] [Rank Pneumo 1990, Seo 1993]

to the cutting direction. The tool was scanned, using atomic force microscopy, prior to each experiment to determine the actual tool edge radius and profile.

2.3.3 Workpiece

The workpiece consisted of a specifically selected orientation of single crystal Ge provided by Eagle Picher. The coupon of Ge was a rectangle measuring 15 mm long, 12 mm wide, and 1 mm thick. The workpiece dimensions were selected to allow for the orthogonal flycutting geometry. The workpiece occupied 11.28° of the circle mapped by the tool's rotational path which had a radius of 76.2 mm. The Ge orientation was such that cutting was on the (001) face in the [$\bar{1}$00] direction (see Figure 4). This orientation was selected to provide the smallest propensity for pitting damage, based on the results reported by Blackley and Scattergood [1990]. Their results showed that pitting damage varied with cutting direction in the machining of single crystal Ge wafers; the selected direction of [$\bar{1}$00] on the (001) face provided the least propensity for pitting.

The workpiece overhang was approximately 2 mm of the specimen's 12 mm width, with the remainder of the specimen sealed into the specimen coupon holder with wax and then clamped into the workpiece holder. The dimensions of the workpiece, as compared to the off axis dimension, provided for planing of the workpiece.

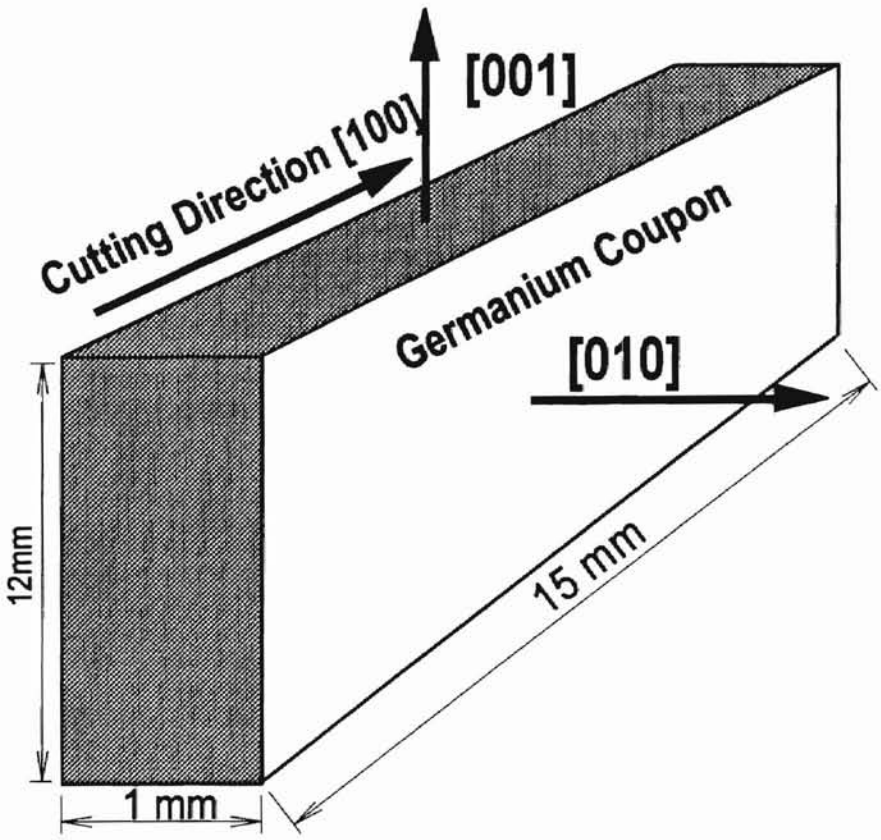

Figure 4. Shown here is a schematic detailing the workpiece dimensions and orientation

2.4 Data Acquisition Equipment

2.4.1 Force System Acquisition Equipment

2.4.1.1 Dynamometer

A Kistler 9251A piezoelectric dynamometer was placed directly behind the workpiece holder to measure the two dimensional forces, cutting and thrust forces, during the cutting process. The transducer was heavily loaded to ensure that the cutting forces

would be transmitted through the friction at the mounting interface. It is recommended that the preload exceed the maximum expected force by at least a factor of 10. A thin coating of lubricant was applied to each side of the dynamometer prior to mounting to allow the transmission of high frequency forces [Seo, 1993].

2.4.1.2 Oscilloscope

The force signals were displayed on a Nicolet Pro 10 oscilloscope via the amplifier. The oscilloscope was used to observe, measure and store the two dimensional force signals. The force signals were stored using the oscilloscope's floppy drive.

2.4.1.3 Charge Amplifiers

A Kistler 5004 dual mode signal amplifier was used for each force signal from the dynamometer. The maximum specified DC drift of the amplifier was 0.03 pC/sec. Each amplifier was reset prior to storage of the force traces to eliminate DC drift.

2.4.2 Microscopic Characterization Equipment

2.4.2.1 Atomic Force Microscope for Tool Edge Characterization

Prior to each experiment the diamond tool was characterized using a Nanoscope III Stand Alone Atomic Force Microscope (SAAFM) model number SAAFM/1. The SAAFM provides three dimensional surface characterization with subnanometric resolution. The SAAFM is able to map surface topography by utilizing the van der Waals force between the cantilever tip and the specimen surface. The SAAFM uses a 120μm

long triangular cantilever which is controlled by a piezoelectric tube. The cantilever is placed in contact with the surface to be mapped and raster scanned across the surface by applying voltages to the tube. Changes in the surface topography cause deflections in the cantilever as it is scanned across the specimen. These deflections are sensed by using laser light which is deflected off of the back of the cantilever onto a laser diode. The deflections are transmitted to the controlling computer where they are converted into a three dimensional topographical map of the specimens surface [Digital Instruments, 1993].

2.4.2.2 Zygo Laser Interferometric Microscope for Characterizing Machined Surfaces

To characterize the diamond turned surfaces, a Zygo Maxim 3D No. 5700 laser interferometric microscope was used. All images were made using a 40X Mirau objective which provided an optical magnification of 640X. This gave a scan size of 245 x 255 μm and a lateral resolution of 0.77 μm. The laser interferometric microscope operates by using a polarized laser beam which is split into two beams. One of the beams is reflected off a reference surface while the other beam is reflected off the sample. The polarization of the reference beam is rotated such that it is out of phase with the beam reflected off the sample. The two beams are then recombined and the distance to the sample surface is computed for each point in the surface to provide the resulting three dimensional topographic image [MetroPro™ User's Guide, 1991].

2.4.2.3 Nikon Optical Microscope and Scanning Electron Microscope for Surface, Chip and Tool Characterizations

A Nikon optical microscope (M easurescope model MM-11) was used to study and view specimens, tools and chips. Surfaces were often viewed using Nomarski prisms to give an indication of the surface depth and features prior to investigation using the Zygo laser interferometric microscope. An ABT scanning electron microscope (model ABT-32) was used to analyze various chip features and types.

CHAPTER III

EXPERIMENTAL PROCEDURE

3.1 Introduction

This chapter describes the procedures followed during all phases of the experiments including data acquisition, workpiece surface and tool characterization, data reduction, and chip inspection. Careful attention was employed during each phase of the experiments to ensure the greatest accuracy and repeatability of the data.

Prior to beginning the experiments, several parameters were selected including the tool, workpiece orientation, number and placement of the data points, method of data acquisition, and type of data desired. To help in these determinations, several shakedown experiments were performed. Information from the shakedown experiments was used to help select tools for the main experiments. Additional information for tool selection was obtained from tool edge profiles obtained by atomic force microscopy. These profiles furnished information about the tool edge features as well as the radius of the tool edge.

Looking at trends in the preliminary data, a schedule was chosen so that more data points would fall in areas where changes in behavior were indicated. The uncut chip

thickness was limited to increments of 5 nm due to limits in the resolution of the machine tool. Other decisions based on shakedown data included where and when to take surface characterization data. The time needed to characterize a surface and the desire to save characterized specimens for future reference precluded surface characterization at every data point. Several specimens were saved with their machined surfaces intact for later investigations into the depth of the subsurface damage layer and possible quantification of pit density.

3.2 Tool Edge Characterization

Prior to each experiment, the diamond tool was characterized using atomic force microscopy. The same technique as that reported by Lucca and Seo [1993]was used for the tool characterizations and is only briefly described here. The procedure involves positioning the tool, which is secured to a coarse positioning stage underneath the SAAFM (Stand Alone Atomic Force Microscope), where the SAAFM cantilever is raster scanned over a section of the tool. One square micrometer scans were done at three locations along the tool edge. Images from atomic force microscopy suffer from distortion when the sharpness of the object being scanned is on the order of the radius of the cantilever tip. This distortion can be alleviated to some degree if the cantilever tip radius is known.

To determine the radius of the cantilever tip the cantilever was scanned over a specially prepared microsphere standard. Since the size of the microspheres is established

(519 nm with a standard deviation of ± 7 nm), the cantilever tip radius can be determined by measuring the difference between the measured bead dimensions and the actual bead dimensions. Once the cantilever tip radius was known, the image data could be processed and the cantilever tip radius deconvolved from the data to provide a true measure of the tool edge radius. This method only works for the tool edge radius at present, as there currently is no determined method to allow the effects of the cantilever tip to be deconvolved from the entire image.

3.3 Diamond Turning Operation

3.3.1 Fixture Assembly

Prior to the start of any of the cutting experiments the apparatus was assembled following a carefully coordinated series of procedures to reduce the likelihood of errors. The first step in the series was to turn on the oscilloscope, amplifiers, and vacuum pump to allow them to warm up for a period of thirty minutes before the experiments began. Actual assembly began by bolting the micro-height adjuster to the machine tool slideway. The micro-height adjuster was kept square by aligning it with the slideway edge. The dynamometer holding block was then bolted to the top of the micro-height adjuster. The next step in assembly was to attach the workpiece holder and dynamometer. To ensure proper contact and alignment, the mating surfaces of the fixtures were lapped using a No 3600 abrasive paste. A thin film of lubricant (type 1063 provided by Kistler) was applied

to both mating surfaces of the dynamometer to ensure the transmission of high frequency forces and prevent sticking due to the high preload used. Then, the workpiece holder and dynamometer were loosely clamped to the dynamometer holding block using the dynamometer clamping bolt. The bolt went through the center holes of the dynamometer holding block and the dynamometer to the workpiece holder where it threaded into a blind hole in the workpiece holder. For additional information refer to the assembly schematic shown in Figure 3.

Dynamometer connections were made to the amplifiers and the amplifier settings were adjusted according to the specifications provided with the dynamometer. The sensitivity setting on the amplifier was set to 1 N/V. Connections were then made between the oscilloscope and the amplifiers.

Oscilloscope settings were chosen to allow the two force signals to fit on screen simultaneously, while preserving the greatest resolution possible. The setting for the time axis was set to 5 ms/division which gave a signal that took up forty percent of the axis. Unlike the time setting, the voltage settings could be set differently for each channel. Initially each channel was set to 1.5 V/division but these settings were adjusted during the experiment, as necessary, to accommodate the changing signal level and maintain resolution. Triggering levels were chosen and set but were occasionally changed between, and even during, experiments. Generally triggering was done off the upslope of channel one, which was the channel designated for the cutting force. Once settings were fixed and connections were made, the cutting force amplifier was turned off and the sensitivity for

the thrust force amplifier was set to 1000 N/V so that the dynamometer could be preloaded.

To preload the dynamometer the dynamometer, clamping bolt was tightened until a 4000 N axial load was achieved. The preload level was set using the signal output from the force transducer during the clamping procedure. The applied load was approximately three orders of magnitude greater than the largest expected force. This large preload assured that the cutting force would be transmitted through the friction at the mount interface, and that the system stiffness would be adequate. During the tightening of the dynamometer clamping bolt, a square level gauge was used to hold the workpiece holding block square so that the length of the workpiece would be perpendicular to the slideway surface. This ensured workpiece tool alignment such that the desired cutting direction would be achieved. After setting the preload, the amplifier sensitivity was turned down to 1 N/V and both of the amplifiers were reset.

Next, the vacuum chuck was lightly stoned with an ultra-fine stone to remove nicks and surface debris. The tool holding plate with tool holder attached was mounted on the vacuum chuck and the vacuum was turned on. The vacuum pressure was checked and maintained at -21 in. Hg. The workpiece was mounted into the specimen coupon holder using a hard wax, see Appendix A for procedure. The specimen coupon holder was then fastened into the workpiece holder. Prior to mounting, the mating surfaces of the specimen coupon holder were lapped to remove any residual wax and debris. The specimen coupon holder was held by two hex bolts which were carefully tightened to prevent the holder from becoming angled. First the top bolt was tightened until the

specimen coupon holder was lightly held, then the bottom bolt was likewise tightened. The bolts were then slowly tightened one after the other until completely tight. The next step was to mount the diamond tool into the tool holder. The diamond tool fastened into the tool holder using three set screws which were tightened in succession, a little at a time, to ensure that the tool remained straight rather than becoming misaligned.

The final operation, before machining could begin, was alignment of the workpiece and tool. The tool and workpiece were aligned to allow the diamond tool to cut the 1 mm wide workpiece along its entire 15 mm length. The alignment procedure consisted of both the positioning of the tool and workpiece and the setting of zeroes to indicate relative position for the machining program. The tool and workpiece were brought as close as possible with the aid of a magnifying monocle and this position was set as the z-axis zero position. The use of the monocle cut down on dead time, where the tool was cutting only air as it approached the workpiece, because it enabled closer positioning than the naked eye.

3.3.2 Ultraprecision Machining Procedure

With alignment and assembly finished the machining process can begin. Machining was done automatically by the machine tool according to a simple program. The program allowed the control of the process including spindle speed, positioning, and the feed rate which corresponded to the uncut chip thickness. A set of headphones was used during the process to indicate when the tool and workpiece were in contact. This was necessary,

especially at the beginning of a data series or experiment, because often the oscilloscope would not register every cut. Knowing that contact had been made, allowed the oscilloscope settings to be adjusted so the force trace for every cut appeared on screen.

The first series of cuts on a newly mounted specimen were done in order to clean up the surface of the specimen, level it out until the entire specimen length was contacted by the tool, and shake down the setup to make sure everything was properly assembled and connected. The 'cleanup' cuts were usually done at 40 nm or 50 nm; a low enough uncut chip thicknesses so that the surface was not significantly damaged and high enough so that the operation could be finished in a short amount of time.

Once the specimen was 'cleaned up' the data series could begin. The uncut chip thickness corresponded to the machine tool infeed. To change the infeed, the control program had to be edited and the corresponding line changed to reflect the new infeed. The infeed for these experiments ranged from 10 nm up to a maximum of 1500 nm.

The amount of material removed was likewise controlled and was never less than five microns, prior to recording data at any given uncut chip thickness, thus ensuring that the damaged layer generated by the previous cut was completely removed. The amount of material removed was often two orders of magnitude greater than the depth of the previous cut, with three orders of magnitude being the greatest margin and greater than one order being the smallest margin. At the highest uncut chip thicknesses, it was typical to run a 40 nm cleanup cut prior to taking the next cut to further reduce the depth of subsurface damage. It is reasonable to assume that all surfaces generated, and on which data was taken, were completely due to the given uncut chip thickness, since all previous

damage had been removed. This is in good agreement with findings by Lucca et al. [1995], which indicated that the depth of sub surface damage for a Ge surface generated at a 400 nm uncut chip thickness was less than 2 μm, well below the 5 μm threshold set for the experiments. It should also be noted that at the highest uncut chip thicknesses (i.e., 1500 nm) as much as 20 μm of material were removed prior to taking data.

3.3.3 Ultraprecision Machining Variables

All experiments employed a 15 mm x 1 mm rectangular coupon of single crystal Ge as the workpiece. The workpiece was oriented such that cutting took place in the (001) plane in the [$\bar{1}$00] direction (refer back to Figure 4 for an illustration explaining the workpiece orientation). The experiments utilized a single point orthogonal flycutting geometry. A single crystal diamond tool was used for all experiments, that had a nominal rake angle, α, of 0.5°, a clearance angle of 5°, a gross tool edge radius of 0.23 μm, and a measured tool edge radius of 60-70 nm, indicating a sharp tool. The tool had been previously used, thus ensuring that a dramatic amount of tool wear associated with the initial use period (known as 'breaking in') would not occur during the experiments. This was an important consideration, since an unstable tool edge would produce data that were difficult to interpret due to the changing character of the tool during the experiment. Cutting took place in air with no lubricant at a constant speed of 48 m/min. Uncut chip thicknesses ranged from 10 nm up to 1500 nm.

3.4 Data Acquisition

The data acquisition system consisted of a dynamometer, two charge amplifiers, and an oscilloscope. The dynamometer fed the orthogonal force components to the amplifiers, which applied a gain set at 1 N/V and fed the signal into the oscilloscope. The oscilloscope was used to view, store, and measure the force traces. Settings on the oscilloscope were adjusted so that the thrust and cutting forces could be viewed simultaneously with the greatest possible resolution. As many as seventeen consecutive force traces of each component could be saved or stored in the oscilloscopes memory at one time. From these seventeen traces, the most consistent eight traces would be saved onto a floppy disk for measurement.

Consecutive traces were rarely consistent in the middle region of the series (approximately 40-120 nm), whereas traces at the low and high ends of the series were generally the same. This created a dilemma as to which traces to save in the middle region of the series. In this region a somewhat repetitive cycle in behavior was evident. A relatively low level trace would often be followed by a significantly higher trace which would then be followed by two consecutively lower traces, after which the cycle would repeat. The cycle was not always consistent and, often, it was interrupted. In cases where the force level was so erratic, the objective was to select a baseline trace level that presented the highest likelihood of repeatability. For instance, it was rare for a high or low trace to be followed by another high or low trace but a middle trace would occasionally repeat. These repeating middle level traces were selected as the baseline or

most consistent traces. Typical cutting and thrust force traces are shown in Figure 5 and Figure 6 below. Together, these traces are representative of the appearance of the traces over the majority of the data range with the exception of the highest uncut chip thicknesses.

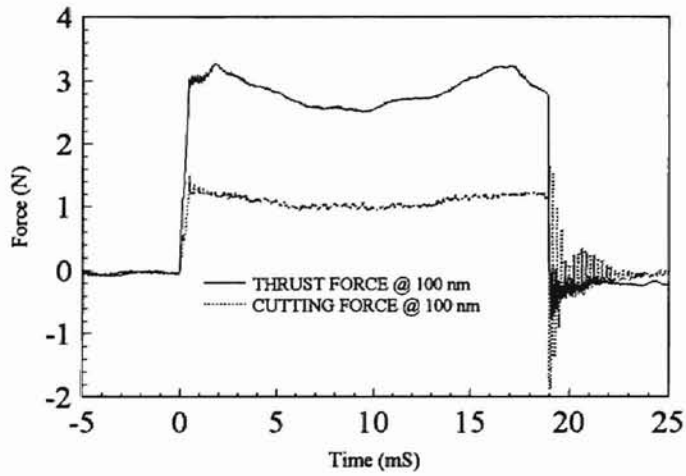

Figure 5. Typical cutting and thrust force traces at a uncut chip thickness of 100 nm. These traces are representative of the middle range of uncut chip thicknesses.

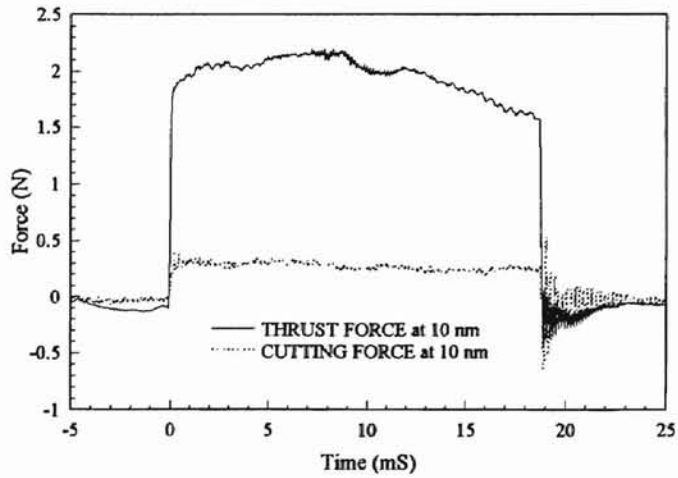

Figure 6. Typical thrust and cutting force traces for a 10 nm uncut chip thickness. These traces are representative of traces seen at the lower uncut chip thicknesses.

Another problem, with the middle range of uncut chip thicknesses in the series, was the appearance of step events where part of a force trace would register at one force level while the remainder would register at another. These traces were frequently followed by another trace displaying a step that was the negative image of the previous trace (i.e. a high-low trace followed by a low-high trace). Since these traces presented unique problems in measuring, and were at best questionable for purposes of this study, they were not used in the determination of reported force values.

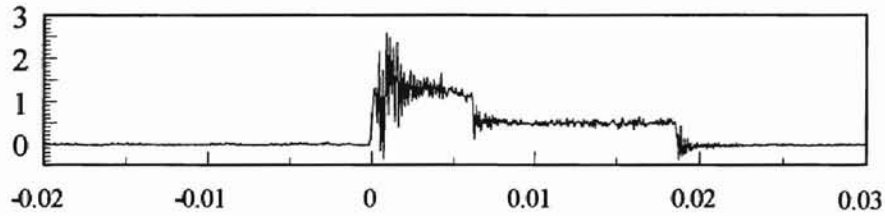

Figure 7. A typical cutting force trace showing a stepped event. These traces were not used for data determination because of their questionable nature and the difficulty measuring them.

At the end of a series, the traces that had been saved were recalled and measured. The measurement of the forces was done in a systematic way to ensure that each trace was measured the same way. This was especially important because a change in the measurement method could result in widely varying data. Figure 8 illustrates the measuring method used to determine the force level reported for a given trace. Only the approximate middle third of the trace was considered for measurement, since the further the tool is from the center of the workpiece the greater the deviation from both the ideal orthogonal cutting geometry and the prescribed cutting direction. The increased likelihood of developing a three dimensional state of stress at the tool entry and exit points

was emphasized by the chipping and cracking of the workpiece that typically occurred at these points.

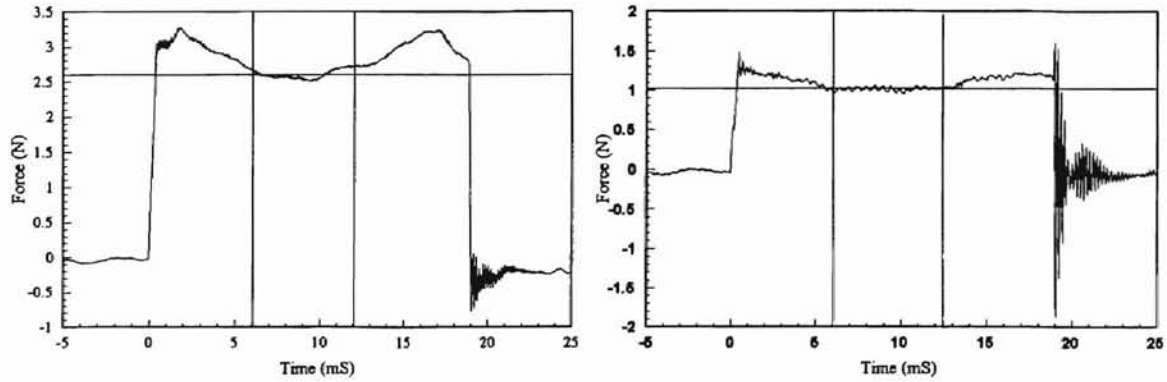

Figure 8. Only the middle third of a trace was considered for force measurement. The force level was determined by the best fit of a horizontal line to this middle third of the trace. These traces were taken using a 100 nm t_o. The force on the left is the thrust force while the force on the right is the cutting force.

For each uncut chip thickness, the measurements for the thrust and cutting force components from each of the eight saved trace pairs, F_c and F_t, were entered into a data table. These measurements were then transferred into an Excel spreadsheet where the eight measurements for each component were averaged together to give the average component value for that uncut chip thickness. These values were then used to compute cutting energies and ratios for each uncut chip thickness in the series. The final step in the data reduction process was to import the various data into Stanford Graphics to construct a series of plots showing the experimental behavior of the process. Plots were created for each series showing the behavior of the force components, specific energy (U), and force ratio (F_t/F_c), as functions of uncut chip thickness.

3.5 Surface Characterization

Surface characterization was done primarily using the Zygo laser interferometric microscope. Prior to inspection using the Zygo, surfaces were often viewed using a Nikon optical microscope with Nomarski capability. When appropriate, micrographs were taken to further verify surface condition. Zygo plots give a topographical three dimensional representation of the surface as well as standard surface roughness measurements, such as RMS, R_a, and PV (peak to valley). Surfaces were then inspected for evidence of pitting and sharp changes in surface roughness measures.

Initially, shakedown experiments were performed to help identify uncut chip thicknesses and uncut chip thickness ranges where behavior appeared to be changing, as based on force trace behavior. During these experiments, the sample was removed after each cut, with careful attention being paid to handling the specimen to prevent damage to the newly generated surface, and placed under the Zygo for examination of the surface. Preceding examination surfaces were cleaned using a solution of 70% methanol and 30% ethanol and blown dry with ultra-filtered canned air. During examinations, the specimen was oriented so that the cutting direction was from left to right to permit comparison of plots (see Figure 9 for more details). A Zygo plot was taken at each point noted in Figure 9. Plots were concentrated on the middle region of the specimen where experimental conditions were closest to the ideal orthogonal cutting geometry. The tool entry and exit points were the furthest from the ideal geometry and cutting direction and thus were not relevant to the experiments.

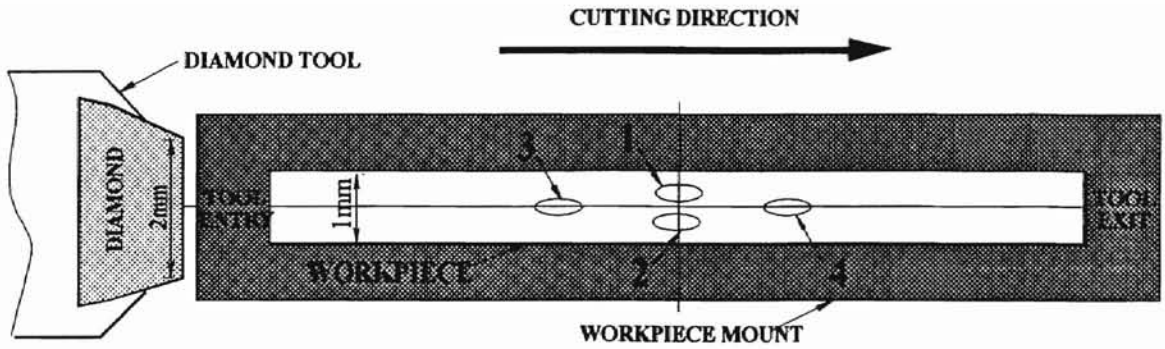

Figure 9. Shown here is a schematic of the Zygo characterization method. The numbered positions show the approximate location of regions where Zygo data was taken for each specimen. Position 1 is top center, position 2 is bottom center, position 3 is right center, and position 4 is left center. The specimen is always oriented with respect to the tool entry and exit points so each position represents the same area on any specimen.

Using the results from the shakedown experiments, specific regions were identified for further study. During the following experiments, specific uncut chip thicknesses were chosen to represent the surfaces in a given range with particular attention paid to identifying transitional surfaces where changes from one behavior to another were noticeable. For each selected uncut chip thickness, the sample was removed and cleaned using dry lens paper and blown clear using ultra-filtered canned air. This method was used because the cleaning solution used in the shakedown experiments frequently left a residue on the specimen's surface. Since the specimen surface was newly generated and special care was taken not to touch the surface or otherwise damage it through mishandling the sample, a solvent was not needed and the purpose of the cleaning was only to remove dust that had collected from the air and chip particles that had clung to the specimen surface. The samples were then characterized using the same method followed in the shakedown experiments.

3.6 Chip Collection and Study

The importance of chip structure as an indicator of machining behavior is well established. To provide additional evidence of the machining behavior during the experiments, chips were collected and observed visually throughout the experiments. Special attention was paid to defining specific chip appearances, or variations, and noting where in the series they were likely to occur. During the final experiment, chips were collected at 10, 40, 45, 55, 60, 65, 70, 80, 85, 90, 100, 110, 120, 130, 140, 150, 160, 400 nm uncut chip thicknesses. These chips were mounted on metal disks, with adhesive, and viewed using an SEM. SEM micrographs were taken of many of the specimens and are presented in Chapter 4.

Initially, the chip samples were left uncoated during the SEM examination, however charging of the chips often increased the difficulty of obtaining steady images. Several micrographs were taken of uncoated chips but eventually the chip samples were coated and the majority of the micrographs were taken of the coated chips. The specimens were coated, with gold palladium for 15 to 30 seconds at a plasma current ranging from 15-20 mA. This resulted in coating thicknesses ranging from 4 to 10 nm. Coating thicknesses can be computed using the following relation:

$$d = KIVt$$

where d is the coating thickness in angstroms, K is a material constant (approximately .17 for gold-palladium), I is the plasma current in mA, V is the sputter-coat voltage in KV, and t is the coating time.

CHAPTER IV

RESULTS

4.1 Introduction

Using the procedure detailed in Chapter 3, experiments were run using a number of different tools. Four of these series of data were generated using Tool CD5400-2 and these are the data series that have been selected for presentation here. Parameters for the four experiments reported here are summarized in **Table 2**.

4.2 Tool Scan Data

Characterization of Tool CD5400-2 revealed a tool edge radius of 60-70 nm. The variation between scans at various positions along the tool was ±10 nm, see Figure 10, which is in very good agreement with Lucca and Seo [1993]. Figure 10 shows cross-sectional profiles of the tool edge taken from various points along the tool edge. These have not been adjusted to account for the distortional effects that exist when the radius of

TABLE 2: **PARAMETERS FOR EXPERIMENTAL DATA SERIES 12, 14, 16, AND 17**

Variables	Data Series			
	D. S. 12	D. S. 14	D. S. 16	D. S. 17
Tool Used	CD5400-2	CD5400-2	CD5400-2	CD5400-2
Lubricant	NONE	NONE	NONE	NONE
Number of Points	35	34	35	35
Point Range	10-1500 nm	10-800 nm	10-1000 nm	10-1000 nm
Material	Ge	Ge	Ge	Ge
Orientation	(001) [100]	(001) [100]	(001) [100]	(001) [100]
Tool Edge Scanned?	NA*	NA	NA	YES
Surfaces Characterized?				YES
	Surfaces Characterized at These t_o's			
				10, 20, 40, 65, 150, and 400 nm

the cantilever tip used to scan the image is on the order of the scanned object. The radius of the cantilever tip used for these scans was approximately 220 nm and, hence, would presumably distort the size of objects of that order or less in magnitude. For this reason, the actual dimensions are less than they appear in the figure.

The actual tool edge radius, 60-70 nm, was determined by deconvolving the effects of the cantilever tip radius from the measured tool edge radius (280 nm), as shown in Figure 12. The cantilever tip radius was resolved by scanning a specially prepared microsphere standard, with the cantilever used to scan the tool, as described in the works

* NA: Not Available

of Lucca and Seo [1993, 1994]. Comparison of the measured sphere diameter with the known diameter indicated a cantilever tip radius of 220 nm, which was used to determine the actual tool edge radius as shown in Figure 11 and Figure 12.

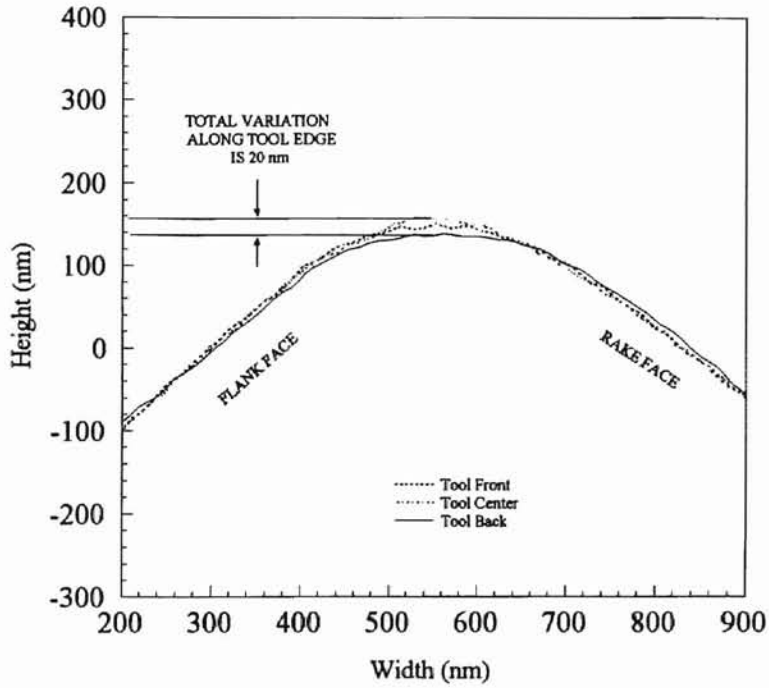

Figure 10. Tool Profiles from AFM scans of Tool CD5400-2. Each profile comes from a scan of a different area of the tool. Three scans were done; one for each of three different tool sections: front, center, and back. Note that the variation between these scan profiles is approximately ±10 nm before adjusting for the cantilever tip radius. The data reported here was taken from scanned images of the tool done between data series 16 and 17.

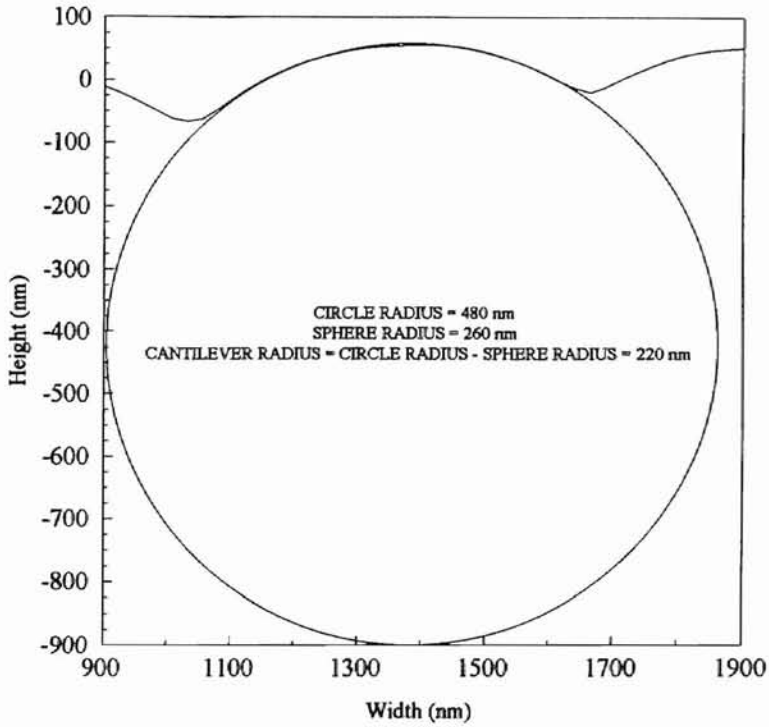

Figure 11. Cross-section of a scan of the carboxylate microsperes used to determine the radius of the cantilever tip. The microsperes are 519 nm with a standard deviation of 7 nm. The diameter of the microspheres in the scan was determined by the best fit circle. The actual sphere diameter then implied a cantilever radius of 220 nm as shown.

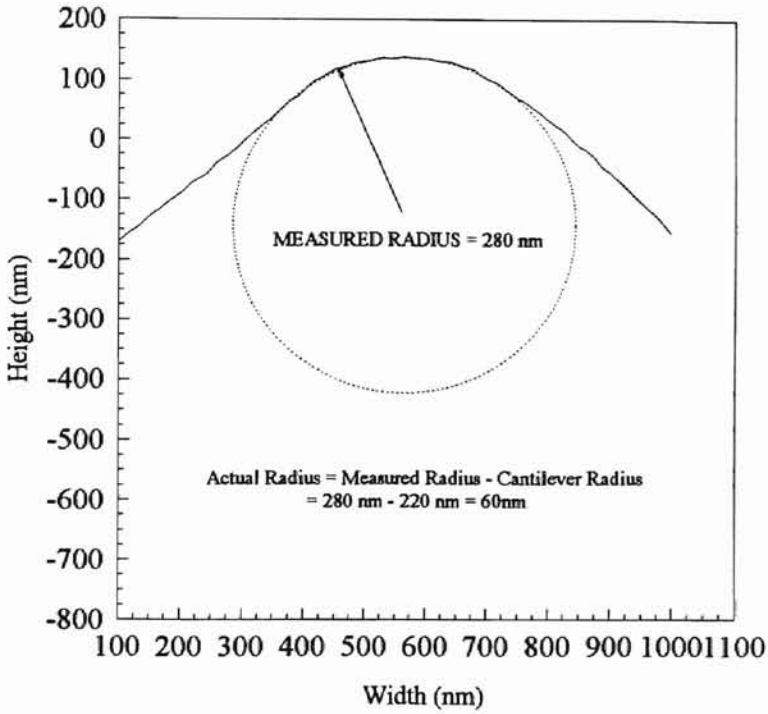

Figure 12. The measured radius prior to deconvolution was determined by measuring the diameter of the best fit circle. The actual radius was calculated using the cantilever tip radius shown in Figure 11. The resulting tool edge radius was 60 nm. Additional scans and calculations revealed a range between 60 and 70 nm for the actual tool edge radius.

Figure 13 shows the local geometry at the tool nose. The profile suggests the appearance of an apparent wear flat on the flank face side of the tool. The measured length of the wear flat is approximately 140 nm; however, the actual value is expected to be less due to the distortion caused by the cantilever tip radius. Features of the tool edge are especially important due to their possible effect on the cutting process and will be discussed in more detail in the following chapter. Figure 14 is an idealization of the tool workpiece interaction due to a tool edge geometry similar to that found for Tool CD5400-2 (see Figure 10). The data reported here were taken from scanned images of the tool done between data series 16 and 17.

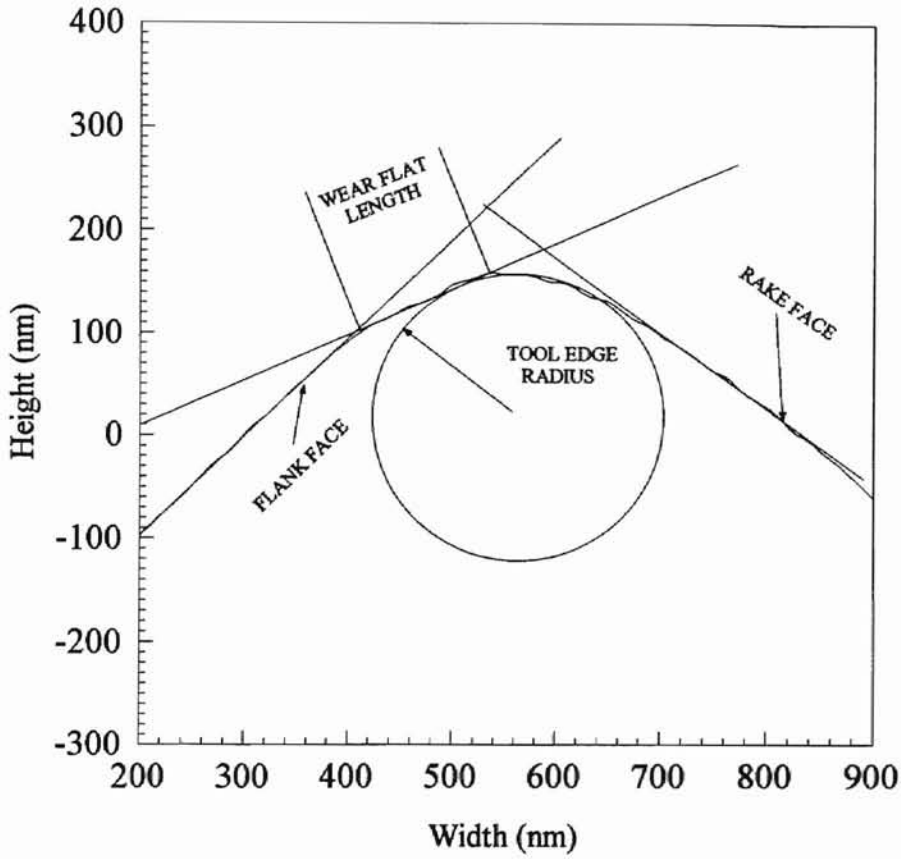

Figure 13. Cross-sectional profile of Tool CD5400-2 taken from the center of the tool. The cross-section shows an apparent wear flat as well as the 'local' tool geometry in the vicinity of the tool nose. The length of the wear flat, not accounting for distortion, is approximately 140 nm.

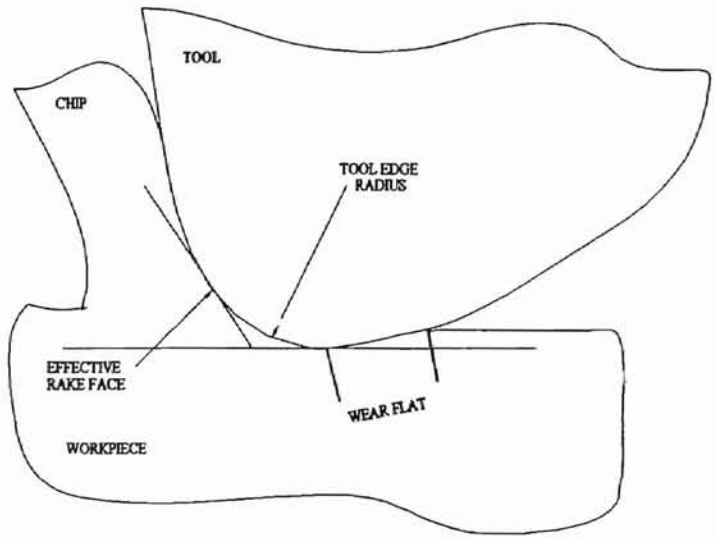

Figure 14. The development of the effective negative rake angle at low uncut chip thickness, as well as plowing at the tool edge, and sliding and wear on the flank face due to elastic recovery of the material. The latter results in a wear flat feature on the flank face of the tool.

4.3 Force System Data

4.3.1 Cutting and Thrust Force Data

Cutting and thrust force data were obtained by averaging the forces obtained from eight representative traces, for each uncut chip thickness in a given experiment. The data reported here cover four separate experiments each of which is designated as a distinct data series (12, 14, 16, and 17 respectively). All of these experiments were performed under the same cutting conditions followed the same experimental procedure and used the same tool. Figure 15 gives a comparison showing the variability between typical traces taken at the same uncut chip thickness. The typical variation within a series of data, at a given uncut chip thickness was 35%. This was determined by the difference between the highest and lowest force divided by the average force.

Figure 16 and Figure 17 present plots of the cutting and thrust force components measured during each of the four experiments. These four plots show the force components for each series as functions of the uncut chip thickness. They present the force magnitudes for all the data as well as the averaged force magnitudes, which are later used to compute the specific energy and force ratio for each series. Each averaged point represents eight traces taken at the given uncut chip thickness which were measured and then averaged together.

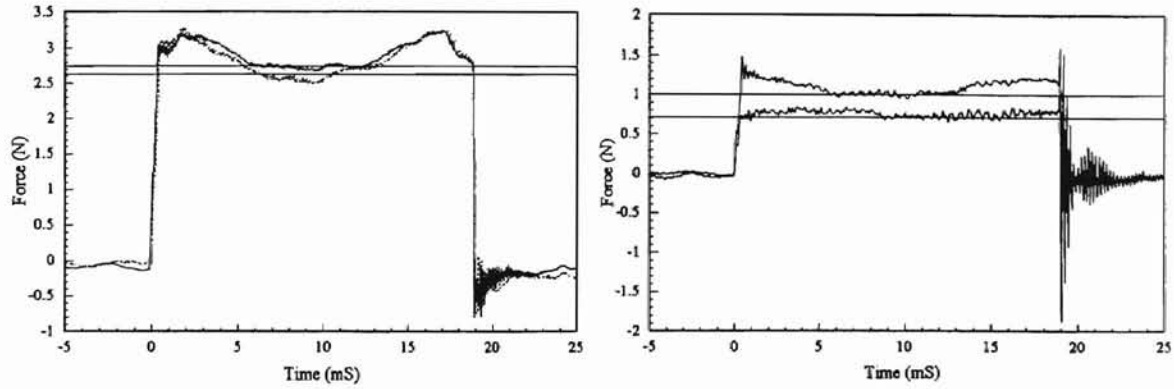

Figure 15. Comparison of thrust and cutting force traces taken at 100 nm uncut chip thickness. This illustrates the typical agreement between force traces taken at the same uncut chip thickness. The thrust forces, on the left, are generally in greater agreement than the typical cutting force, as shown on the right, where the difference between the two traces is 35%.

In general, the forces at the lower uncut chip thicknesses are in greater agreement than those at higher uncut chip thicknesses (note Figure 16 and Figure 17). For each series, the spread in the cutting force data is much greater than for the thrust force data (e.g., refer back to Figure 15). The typical spread in the data for the thrust force component is less than 10% of the averaged value. Even when the spread is at its maximum the value rarely exceeds 20% of the averaged value.

Figure 18 is a comparison of the average cutting force from each series. The series all follow the same general trends; a steady rise from the smallest uncut chip thicknesses up to the highest uncut chip thicknesses, where the force levels begin to drop rapidly. The repeatability between different series is of the same order as the repeatability of the data within the same series. At the greatest spread, discounting forces taken at uncut chip thicknesses at or above 600 nm, the percent difference between the series is less than 30%. This is well within the typical spread between forces at the same uncut chip thickness in

the same series. When the forces are taken at or above a uncut chip thickness of 600 nm, where the force levels fall off dramatically, the percent difference is over 100%.

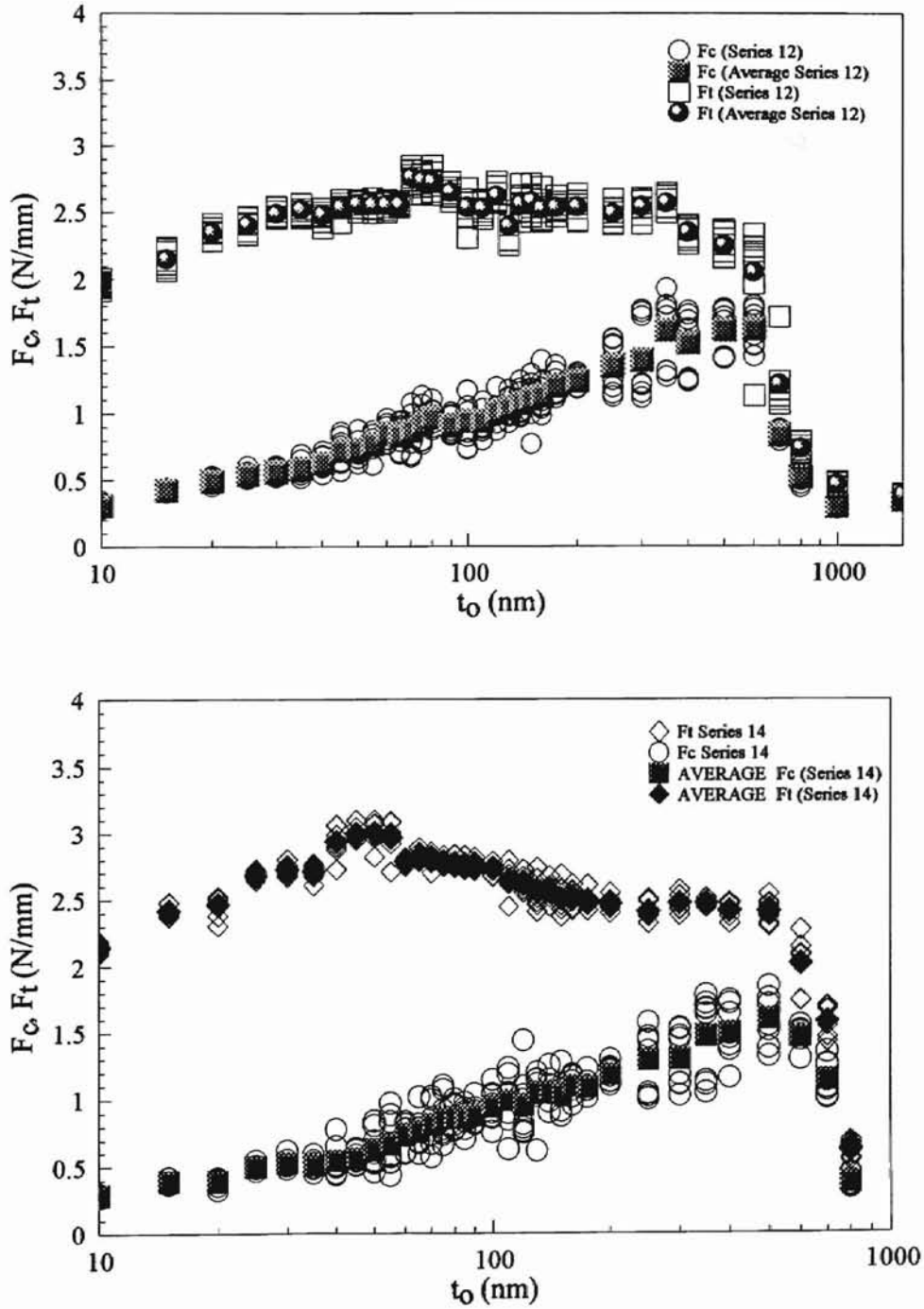

Figure 16. Scatter plots for series 12 and 14. These plots show the spread in the data for the cutting and thrust forces for each series as well as the points for the averaged force values.

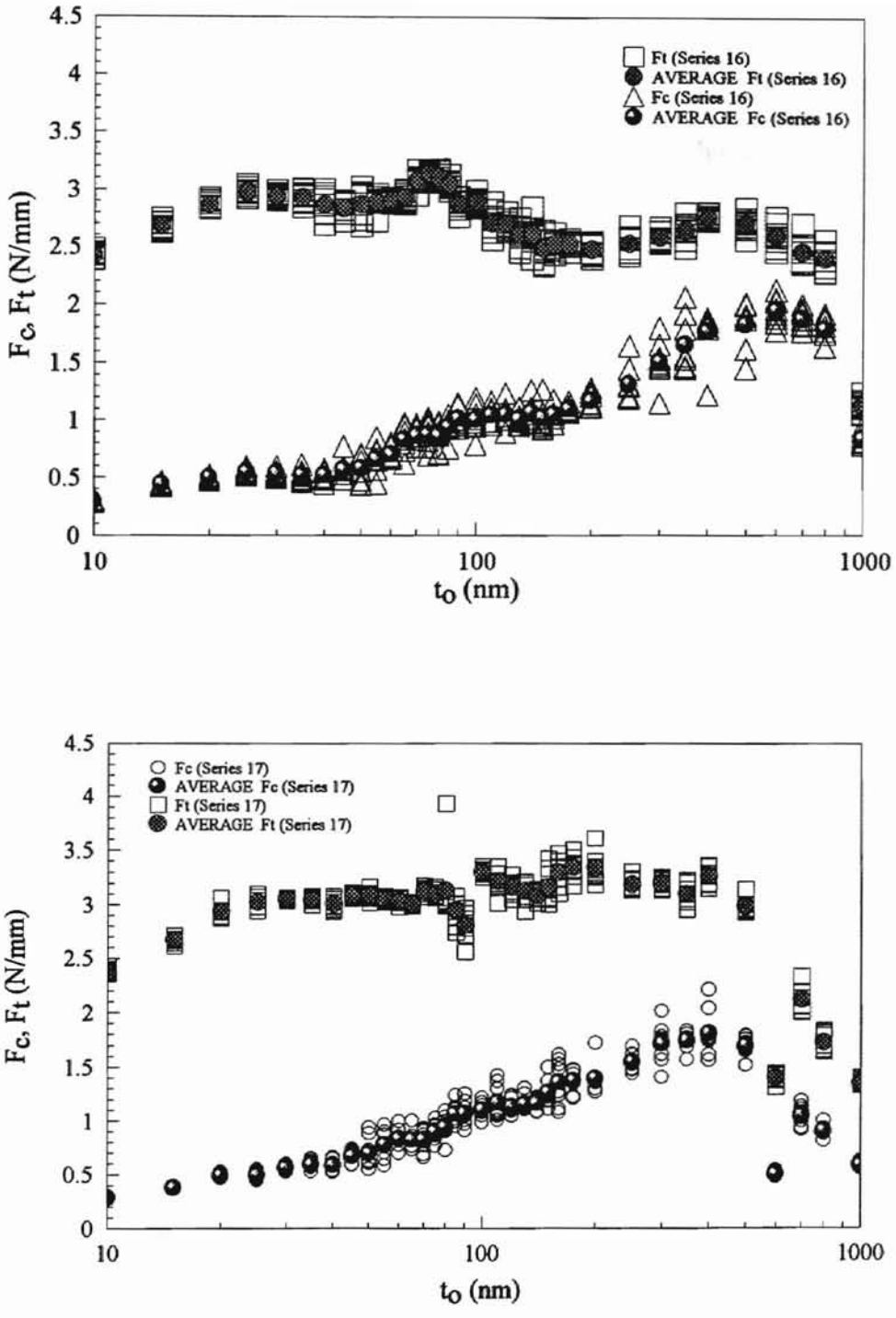

Figure 17. Scatter plots for series 16, top, and 17, bottom, showing the spread in cutting and thrust force data for each series.

The thrust force components follow a different trend as illustrated in Figure 19. Here the repeatability between different series is approximately 30% at the greatest point. This is surprising considering the repeatability between traces at the same point within the same series is far greater for the thrust force components than for the cutting force components. A notable trend seen in the thrust force data, that is not in evidence in the cutting force data, is the steady increase in force levels at the same point between successive experiments. This increase is seen at every uncut chip thickness but is most pronounced at the lower uncut chip thicknesses. These increases from one series to another may be an indication of tool wear.

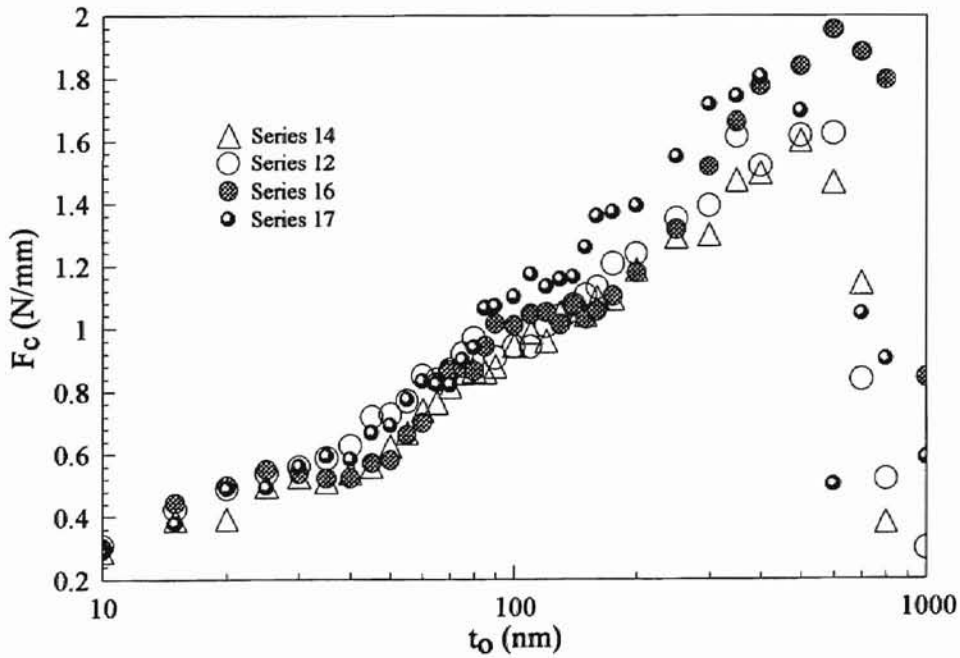

Figure 18. Comparison of cutting force as a function of uncut chip thickness, t_o, for each data series. The differences between the sets are of the same order as the scatter of the data within each series.

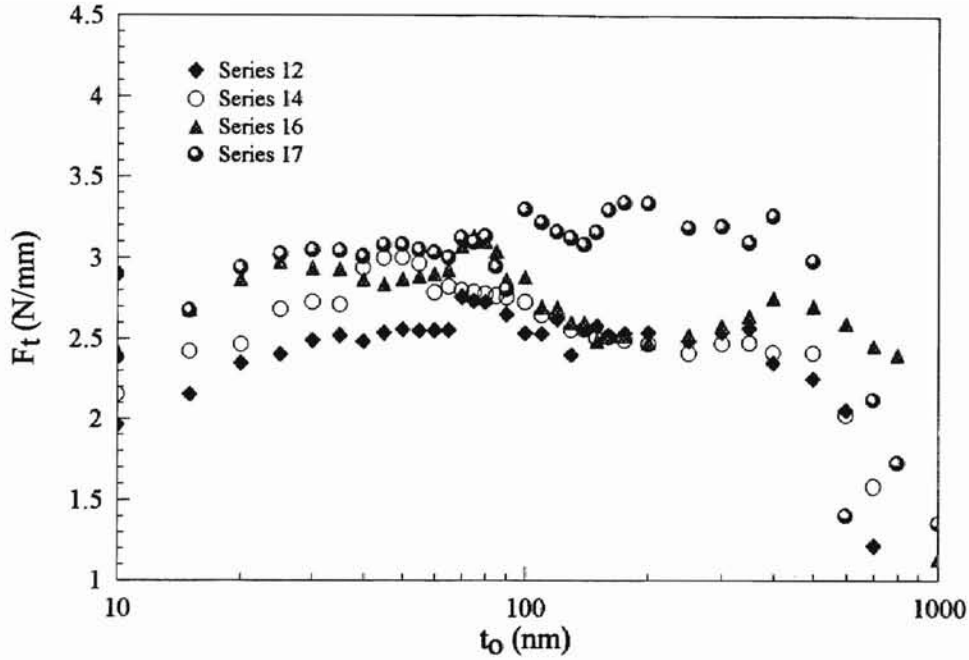

Figure 19. Comparison of thrust force data between series 12, 14, 16, and 17. The percent difference between the data from each series is approximately 30% at the point of the greatest spread in the data. Note the increase from series to series, 12 to 17 respectively, possibly indicating tool wear.

4.3.2 Specific Energy and Force Ratio

The force magnitudes from each series were used to compute the specific cutting energy and cutting force for each point in a given series. The equations for specific energy and force ratio, respectively, are:

$$\text{Specific Energy} = u = \frac{F_c}{wt_o},$$

$$\text{Force Ratio} = \frac{F_t}{F_c}$$

The specific energy is the amount of energy required to remove a given volume of material and is fundamentally a measure of the efficiency of the removal system. The

general trend found for ductile materials is a sharp rise at the lower uncut chip thicknesses due to energy dissipated in subsurface deformation, plowing, and sliding (Lucca and Seo, 1991). The data shown here display the same rise in specific energy at low uncut chip thicknesses that is reported for ductile materials (see Figure 20). This correspondence in the data trend suggests a similarity in cutting behavior for both ductile and brittle materials. This will be addressed in more detail in Chapter 5.

The force ratio is an indicator of the dominant action in the cutting process. A high force ratio indicates that the thrust force is dominating the process while a low force ratio indicates that the process is dominated by cutting. Figure 21 compares the force ratio between each data series as a function of t_o. The angle of the resultant force vector is determined from the inverse tangent of the force ratio. A plot of the angle of the resultant force vector as a function of the uncut chip thickness, for data series 17, is given in Figure 22. The direction of the resultant force is of particular interest when studying the subsurface deformation of the workpiece. This will be especially important for studying brittle materials since the direction of the resultant force may help predict the possibility of opening fractures or pits during the cutting process. This is indicated in work published by Blackley and Scattergood [1990] where they suggested that pitting of the surface in machined Ge was due to the development of subsurface tensile stresses in the workpiece behind the tool. The character of these stresses is indicated by the direction of the resultant force vector. As the resultant force rotates into the material, and hence as the process becomes thrust dominated, the formation of tensile stresses behind the tool ceases.

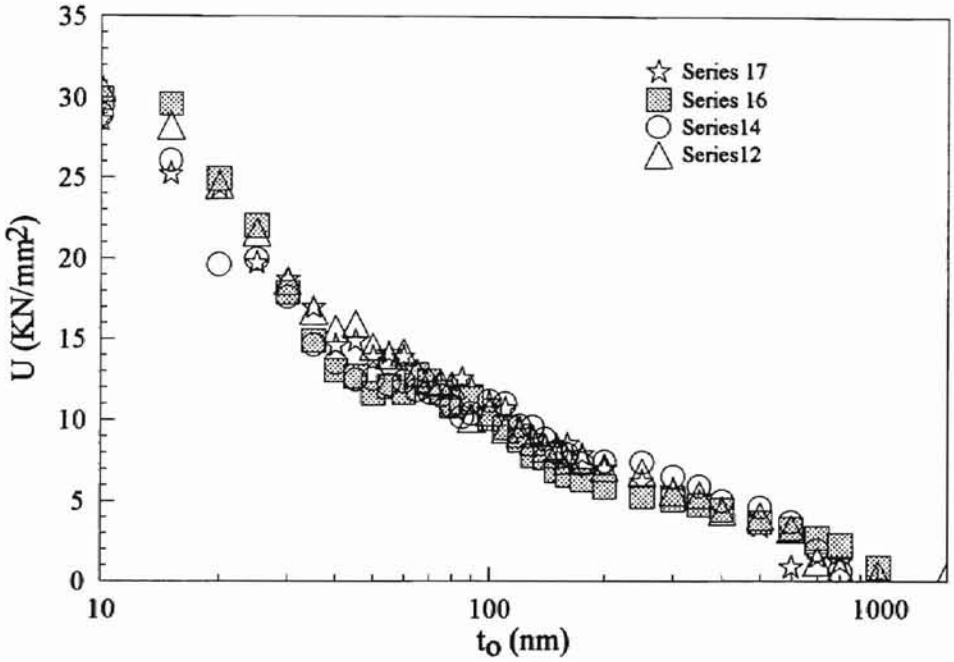

Figure 20. Specific energy versus uncut chip thickness for Data Series 12, 14, 16, and 17.

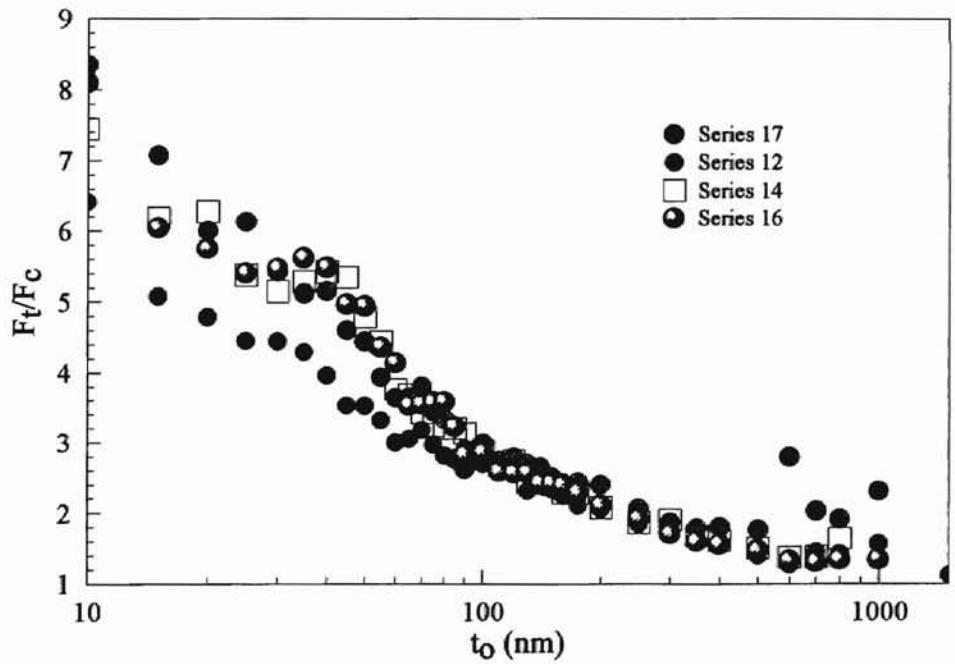

Figure 21. Comparison of the force ratio for each series as a function of uncut chip thickness.

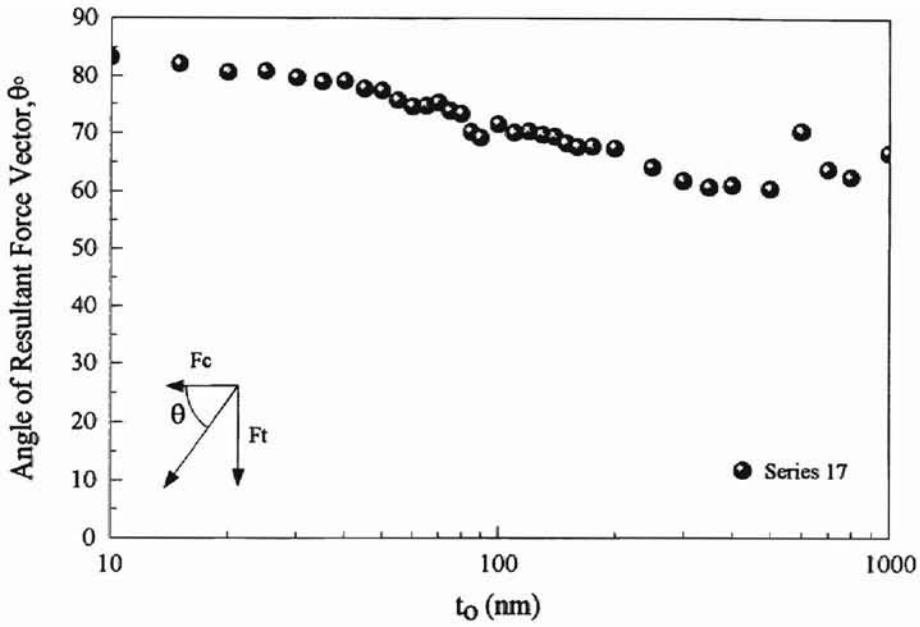

Figure 22. Angle of resultant force vector for Data series 17.

4.4 Surface Characterization Data

4.4.1 Image Analysis

All surface characterizations were done using a Zygo laser interferometric microscope. Surface plots were taken at four different points on six different specimens whose surfaces were generated at known uncut chip thicknesses. Surface plot data, much like the force measurement data, were taken in the central third of the Ge coupon (see Figure 9 for point placement and methodology). The purpose of the surface plots was to

analyze the surface character and determine if, and at what t_o's, the generated surface evidenced pitting damage. The Zygo software provided a variety of analysis options for the image data. Typical surface measurements such as PV, rms, and Ra, as well as data manipulation capabilities that allowed the removal of a surface from the image data, were available as options. Since various surface measurements were easily skewed by the global specimen geometry, it was necessary to remove a plane from the image data so that the slight incline of the specimen surface would not obliterate the smaller local roughness features. The Zygo software capabilities also allowed the analysis of a slice of the image data in any given direction. Specimens were oriented such that the cutting direction was from left to right in the Zygo images. With this orientation, the 'knife marks' from nicks in the tool edge were also predominately in the images x-direction (in some images the marks are noticeably angled due to the arced path followed by the tool). This precluded taking cross-sectional slices in the y-direction since the larger features from the knife marks obscured the smaller surface features.

The prominence of knife marks concealed the underlying surface data in any analysis applied to the entire image (e.g. note the lack of a trends in the surface data shown in **Table 3**). To alleviate this problem, two tactics were employed. The first was to take all slices in the x-direction, and thus within the grooves of the surface, thereby avoiding the obscuring effect of the large knife features. The second tactic was to use an image analysis option that allowed the x and y slopes of a surface to be mapped separately. This had the effect of essentially separating the data due to the knife marks, whose slopes were predominately in the y-direction, from the remaining surface data. Without the

camouflaging effect of the knife marks, the x-slope image yielded a better opportunity for analyzing the surface character of the specimen. Using these two tactics the additional data summarized in **Table 3** were collected.

4.4.2 Surface Plots

Six specimens were analyzed using the laser interferometric microscope. These specimens were machined during data series 17 at 10, 20, 40, 65, 150, and 400 nm uncut chip thicknesses respectively. The surface plots were analyzed to determine if any indications of pitting were discernible. Specimens machined at a t_o of 50 nm or less exhibited no evidence of pitting damage. Specimens machined at a t_o greater than 90 nm displayed increasing amounts of pitting damage as t_o increased. The middle range between 40 and 90 nm gave varying results. Usually, there was no evidence of pitting for specimens up to approximately 70 nm and, conversely, the surfaces generated at uncut chip thicknesses greater than 70 nm typically evidenced some pitting damage. Occasionally, however, the reverse would be true and slight pitting would at times be discernible at a t_o as low as 60 nm or a non-pitted surface would be generated at a uncut chip thickness as high as 85 nm.

A comparison of roughness measures, obtained from x-slice and x-slope analyses of the laser interferometer images, is shown in Figure 23, for x-slice data, and in Figure 24, for x-slope data. The general trend shows increasing roughness values for increasing uncut chip thicknesses. This trend is the same for both the x-slice and x-slope data. There

is a greater spread in the x-slice data than for the x-slope data which is computed over the whole image rather than over one slice of the image.

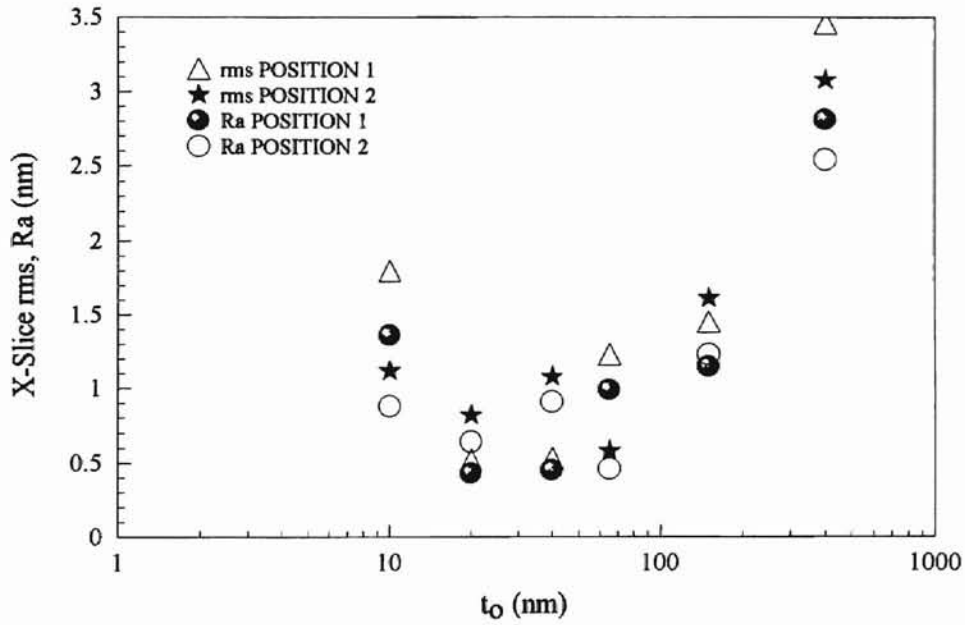

Figure 23. X-Slice data from Table 3 plotted as a function of uncut chip thickness.

TABLE 3: **SUMMARY OF ZYGO CHARACTERIZATION DATA FOR EACH SPECIMEN AT POSITIONS 1[1] AND 2[2]**

t_o	10 nm		20 nm		40 nm		65 nm		150nm		400nm	
Position	**1**	**2**	**1**	**2**	**1**	**2**	**1**	**2**	**1**	**2**	**1**	**2**
Surface												
PV (nm)	29.91	48.87	17.87	48.35	24.18	29.14	43.07	22.57	47.7	46.23	132*	380*
rms (nm)	3.88	8.18	2.8	7.6	3.65	4.72	6.57	3.25	6.13	3.88	6.27	12.68
Ra (nm)	3.07	6.10	2.25	5.57	2.88	3.75	4.92	2.53	4.66	2.99	4.81	8.92
X-Slice[3]												
PV (nm)	9.8	5.57	2.4	3.84	2.28	4.49	5.95	3.24	7.62	9.69	18.00	14.15
rms (nm)	1.8	1.12	.52	.82	.53	1.08	1.23	.58	1.45	1.61	3.46	3.08
Ra (nm)	1.36	.88	.43	.64	.45	.91	.99	.46	1.15	1.23	2.81	2.54
X-Slope[4]												
rms (μm/mm)	.34	.17	.13	.19	.14	.25	.26	.24	.63	.85	2.23	3.09
Ra (μm/mm)	.27	.21	.11	.15	.11	.20	.20	.19	.45	.60	1.70	1.81

[1] Position 1 is top center. See Figure 9.

[2] Position 2 is bottom center. See Figure 9.

* These data are rounded to the nearest whole number.

[3] X-Slice is a cross-sectional profile of the surface in the x-direction.

[4] X-Slope is a map of the slope in the x-direction for the entire surface plot

Examples of some of the images obtained from the laser interferometric microscope are shown in the following figures. These are examples of the surface plots as well as the corresponding x-slope plots . The surface profile is obtained from a cross-sectional slice of the surface image. The values listed below surface plots and surface profile plots are the data summarized in **Table 3**. The image of the surface generated at a t_o of 20 nm is representative of the unpitted surfaces seen at the lower uncut chip thicknesses while Figure 26 illustrates surfaces typical of those generated at the higher uncut chip thicknesses in the experiments.

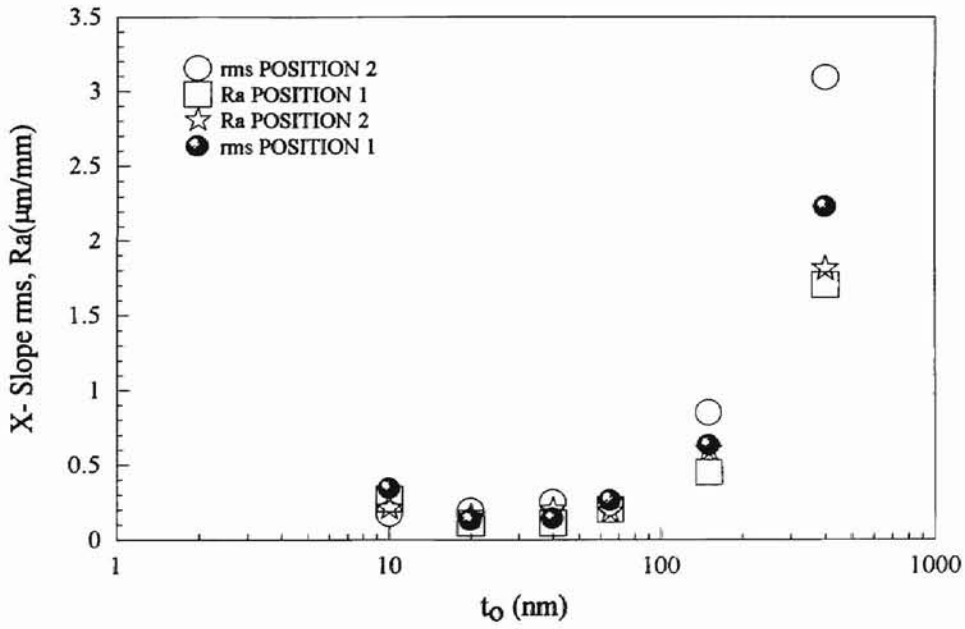

Figure 24. X-slope data values for positions 1 and 2 plotted as a function of t_o. As illustrated there is considerable repeatability between values taken from images of the same specimen.

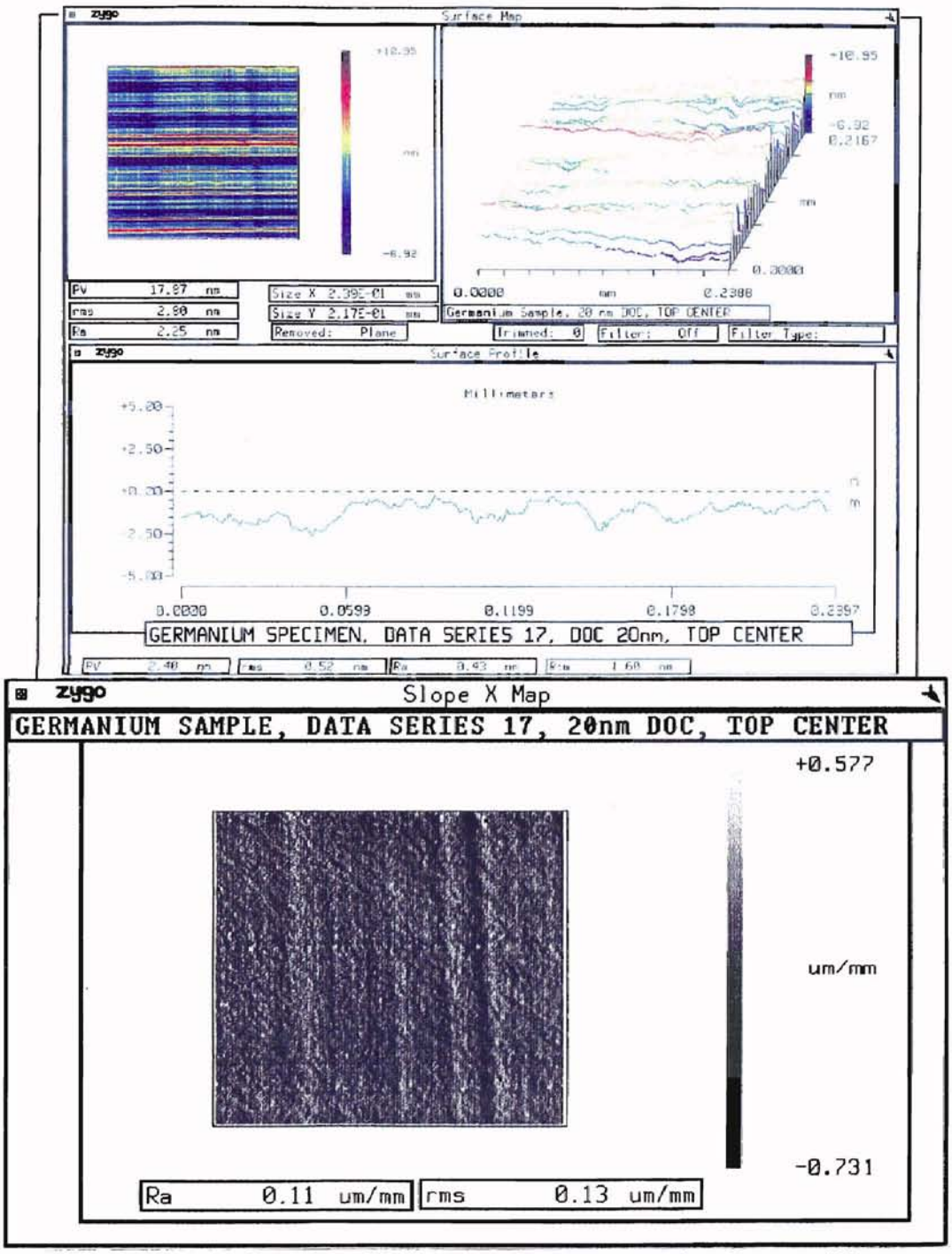

Figure 25. Zygo surface plot and X-Slope map for specimen machined at a t_o of 20 nm. This image was taken from the top center position of the Ge specimen (see Figure 9). Note the lack of 'knife marks' on the X-Slope plot.

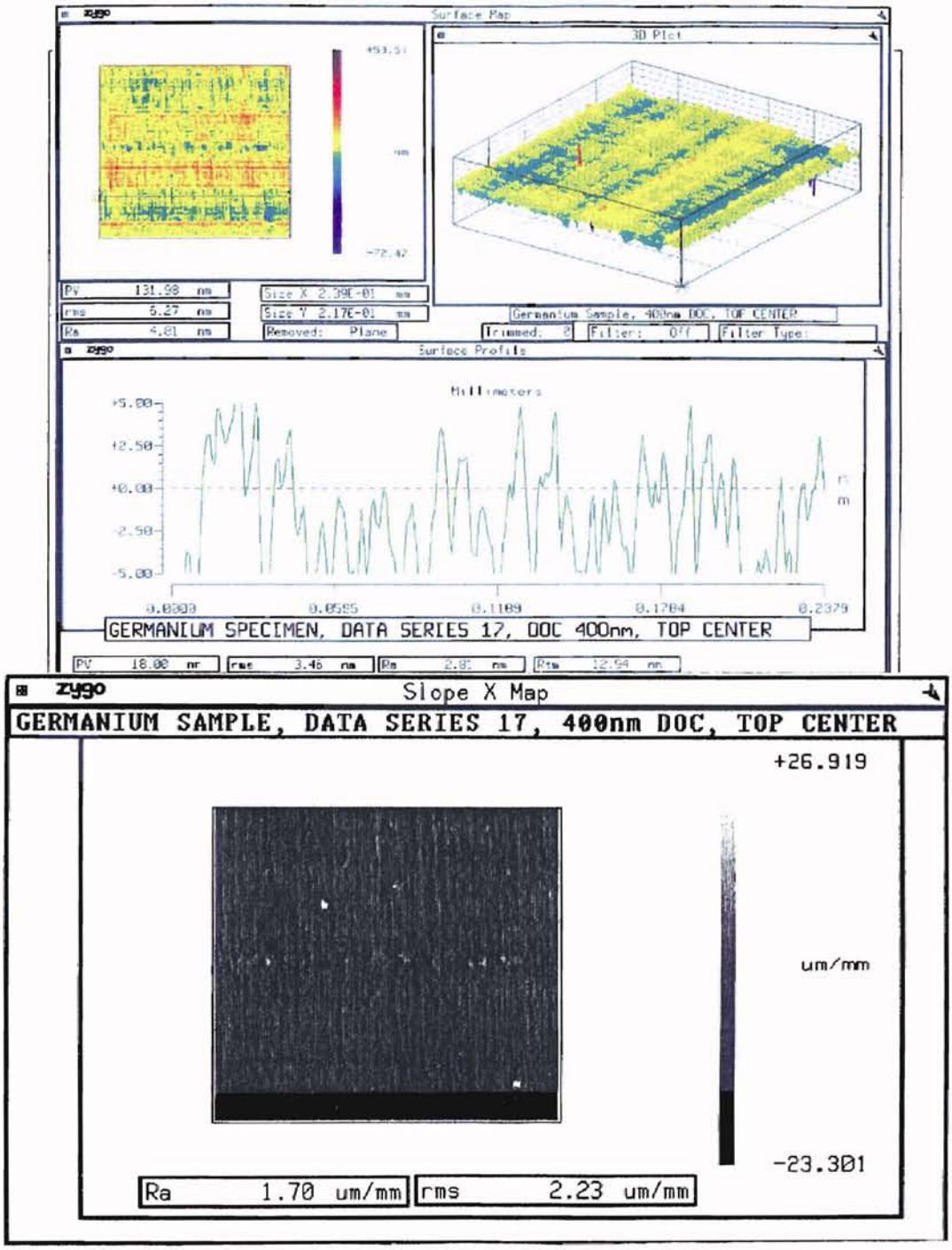

Figure 26. Zygo images for a surface generated at 400 nm. The top plot is the Surface Map while the bottom plot is the X-Slope Map. Pitting is noticeable in both plots. These plots were taken at the top center position of the specimen

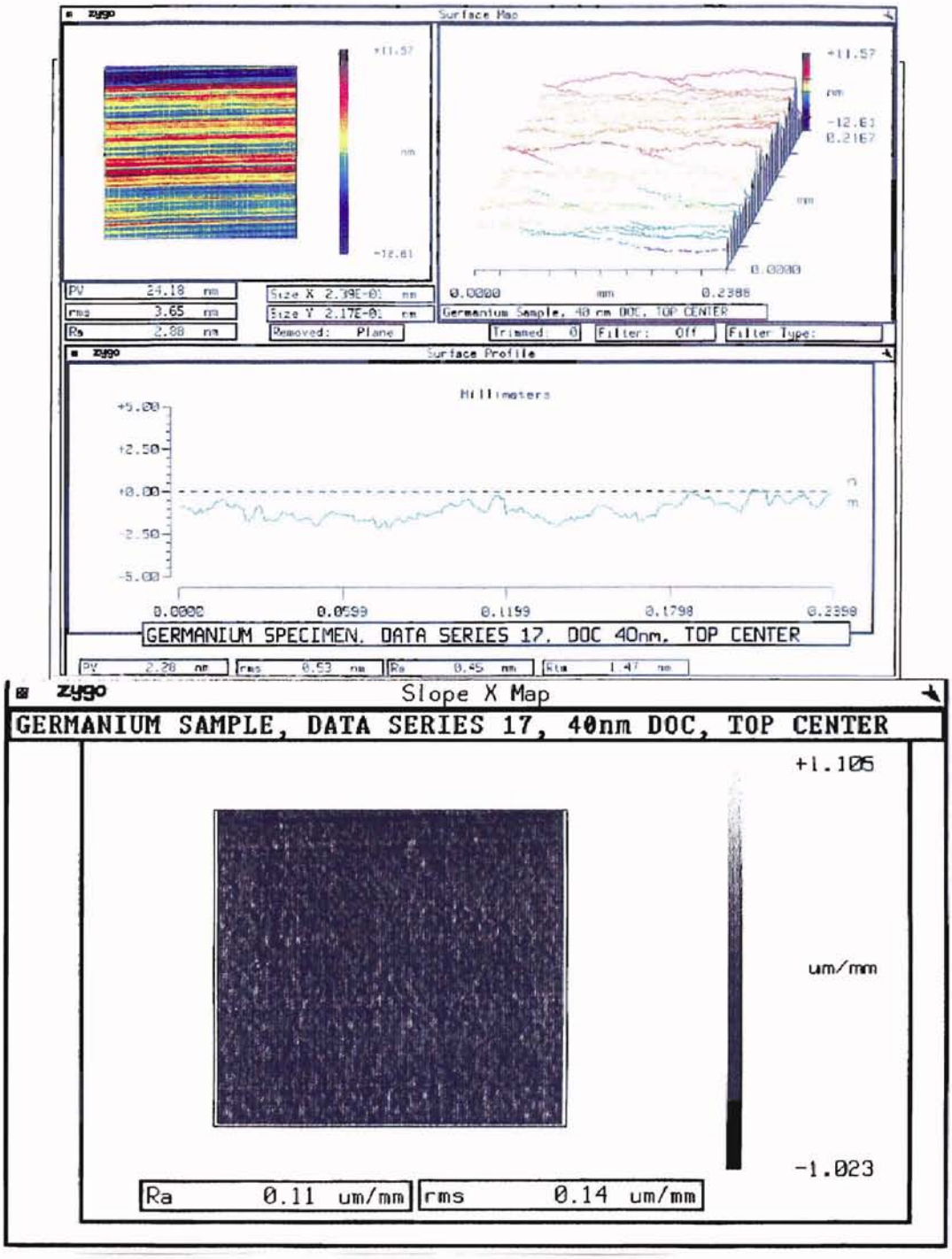

Figure 27. Zygo images for surface generated at a uncut chip thickness of 40 nm.

4.5 Chip Appearance Data

The importance of chip appearance in characterizing the cutting process is long established. The formation and structure of the chip is integral to the cutting process and, as such, provides a convenient method of characterizing it. For this reason, chips were inspected visually throughout all four series of experiments. These observations were recorded and are summarized in **TABLE 4**. Three distinct chip morphologies became apparent during the first experiment and consistently reappeared during successive experiments. Here, rather than referring to established chip types, morphologies simply refer to the structure and appearance of the chip. The chip morphologies were segregated into uncut chip thickness ranges, suggesting that the predominate mechanism for material removal was changing over the cutting range. During the final experiment, chips were collected at various uncut chip thicknesses covering the entire range of uncut chip thicknesses for inspection using scanning electron microscopy. Some of the micrographs from this investigation are presented in this section; additional micrographs are presented in Appendix A.

Initial inspections using the scanning electron microscope were done on uncoated chips. All images of the coated specimens were taken at less than 1000x magnification. As a result, observable chip features in the images are on the order of a micrometer. The maximum coating thickness for the coated specimens is less than 15 nm, therefore, the coating thickness is not great enough to impact the image features. This is further

supported by comparing several of the images of uncoated chips with those of similar but coated chips[1].

4.5.1 Chip Structures

Three distinct chip morphologies and an additional three intermediate chip morphologies, that appeared to be transitional in nature, were observed during the cutting process. The distinct morphologies were called Forms A, B, and C. The first three micrographs illustrate the appearance of the major chip forms. The Form A chips are apparently continuous ribbons of material that hold their structure after cutting. These chips were coiled at the lowest uncut chip thicknesses but as t_o increased the chips became loose ribbons, as shown in Figure 28. The corrugated texture of the chip may be due to buckling of the weak chip.

The second chip form had a tubular construction. These chips were curled about their longitudinal axis forming a long tubular strand as illustrated in Figure 29. The fractures noticeable in the micrograph are perpendicular to the cutting direction. The third chip form first appeared at an uncut chip thickness of 80 nm and was not a chip so much as the lack of a discernible chip. Form C chips were composed of increasingly discontinuous powdered workpiece material which prevented the collection of a distinct chip for study at high uncut chip thicknesses. At lower uncut chip thicknesses, the Form

[1] For example, compare the coated chip pictured in Figure 33 and the uncoated chip in Figure 34.

C chip consisted of a collection of loosely associated particles that held together in a distinctive bundle shape and under SEM inspection resembled fragments of Form B chips.

Transitional chip types were also observed, for example, one transitional chip had a structure between that of Form A and Form B. This chip was a ribbon with slightly curled edges or at times a ribbon where one portion of the chip was curled similar to a Form B chip while the remainder of the chip exhibited the same structure as a Form A chip. The remaining transitional chips were composed of structures between those of Form B and Form C. They appeared to represent a series of successive steps in the degeneration of the Form B chip into the Form C chip[1].

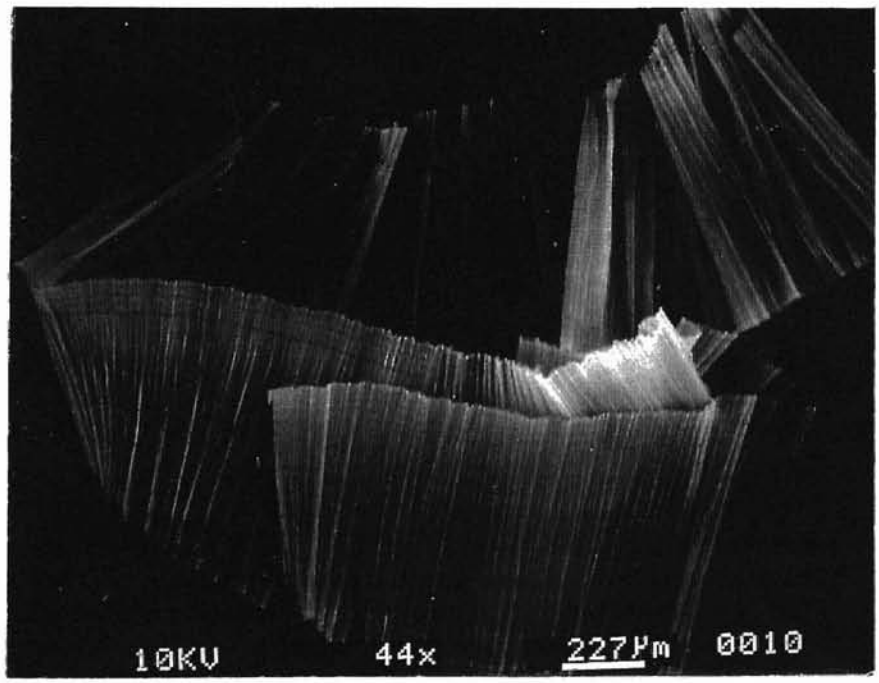

Figure 28. Definitive example of the Form A chip morphology. This chip was generated at a t_o of 10 nm and is magnified 44 x. Note the corrugated appearance of this chip as compared to the image in Figure 41 of another Form A chip which was generated at 40 nm. The majority of the chips collected at the 10 nm uncut chip thickness were tightly coiled. This specimen is coated.

[1] For example, see Figure 30 and Figure 34.

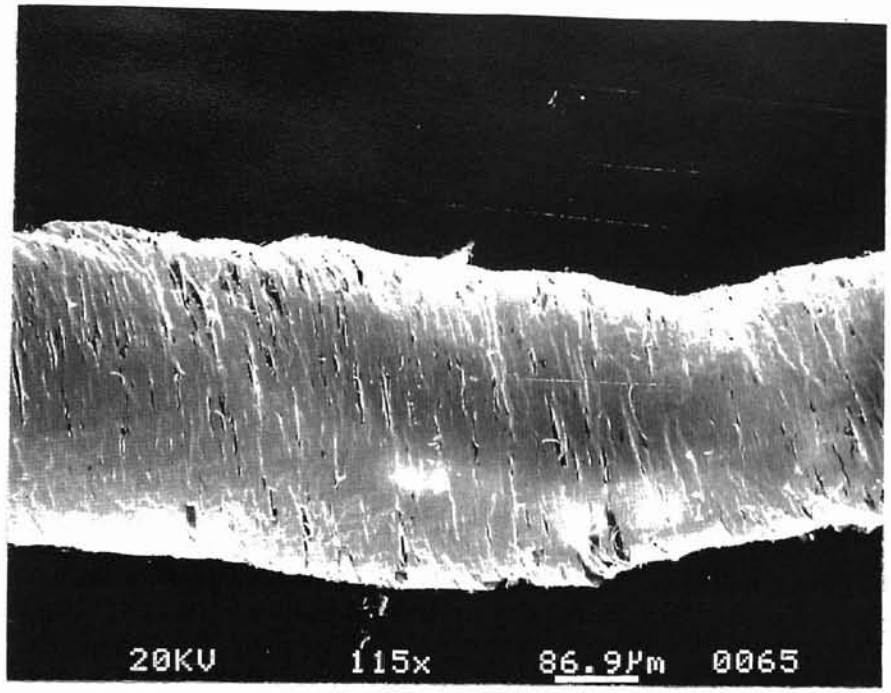

Figure 29. This is the back view of a Form B chip magnified 115X. The chip has curled about its longitudinal axis (the axis in the cutting direction) forming a tubular strand. This particular specimen was collected at a t_o of 65 nm and was coated with AuPd prior to examination.

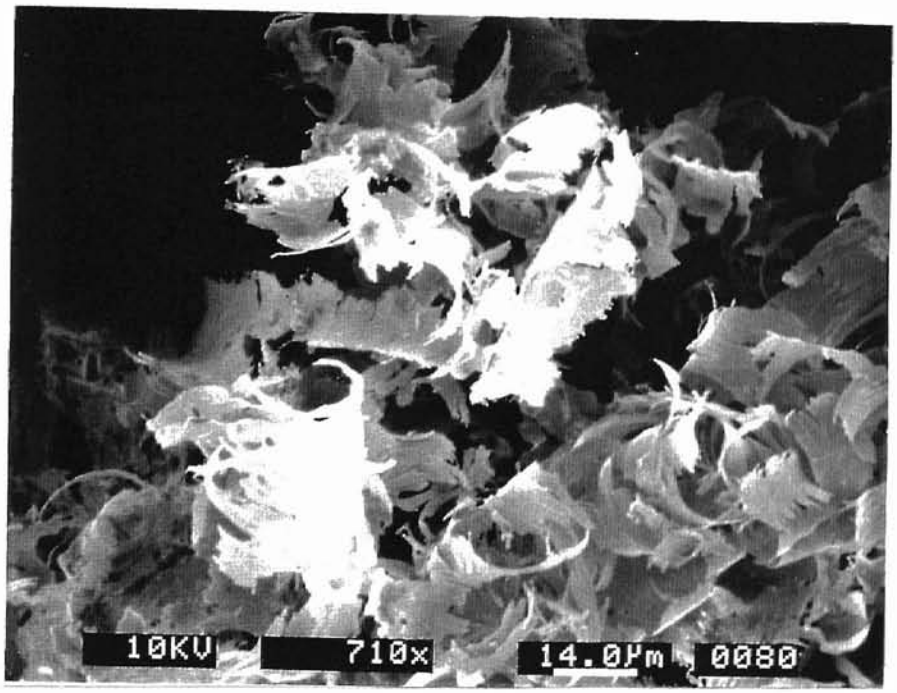

Figure 30. This is the third and final chip morphology magnified 710X. Form C chips are composed of completely disassociated powder and as such were difficult to collect. This chip taken at a uncut chip thickness of 80 nm is a loosely associated collection of particles that has a fragile but distinctive bundle configuration. Notice how the pieces resemble fragments of a Form B chip (see Figure 46 for comparison). This specimen was coated.

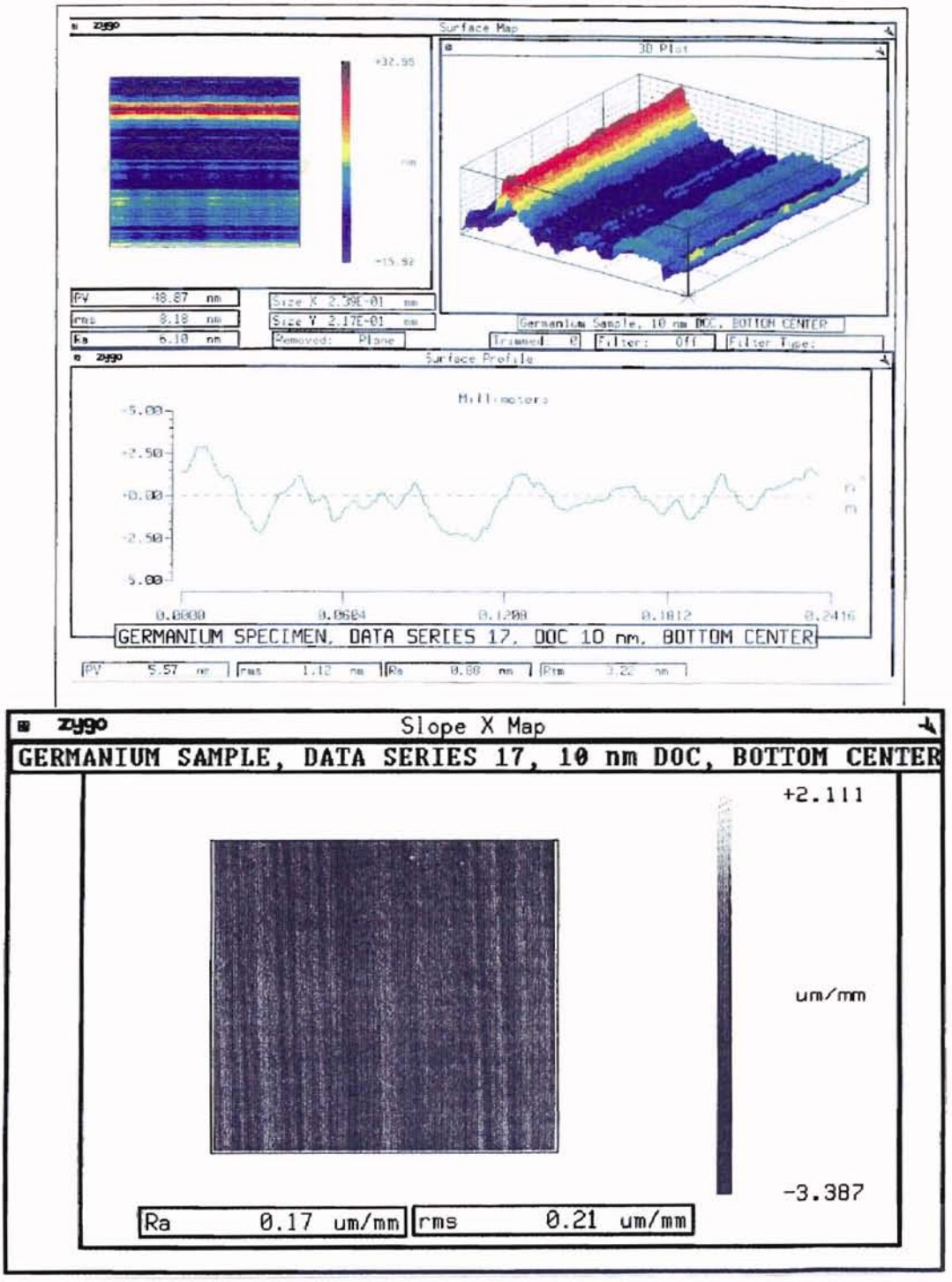

Figure 31. Zygo image and X-Slope map of surface generated using a 10 nm uncut chip thickness. These images are particularly interesting when compared with the images of the chips generated from this surface. The large knife mark seems to coincide with the prevalent longitudinal band seen in the chip in Figure 32. Furthermore, the X-Slope plot shows a corrugated texture that resembles the appearance of the 10 nm chip seen in Figure 32.

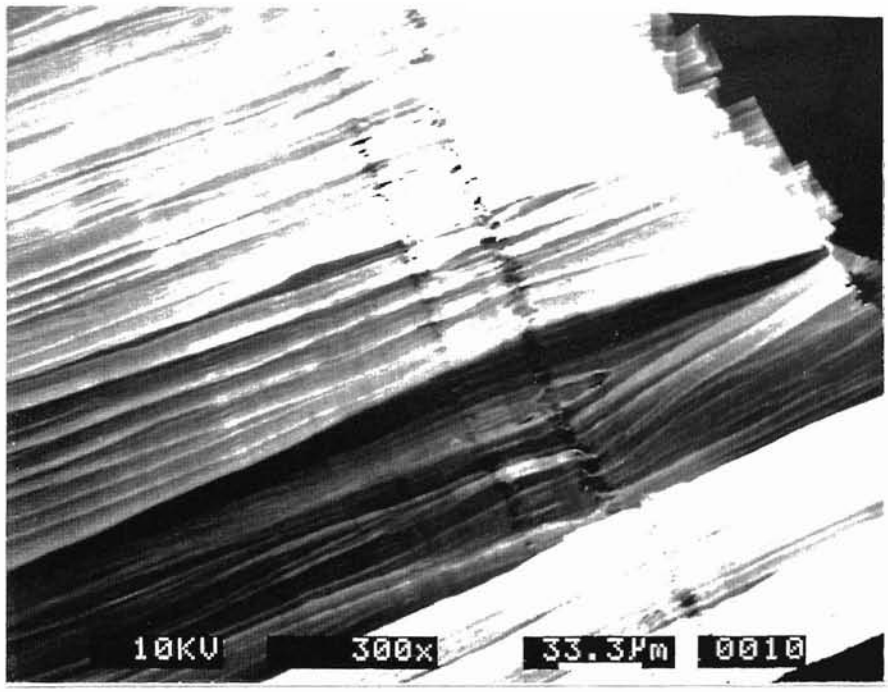

Figure 32. Form A chip generated at a 10 nm uncut chip thickness magnified 300X. Note the corrugated texture of the specimen, which may be the result of either chatter or grabbing during the experiment or buckling of the weak chip. The longitudinal bands, especially on the far right, may be due to a large chip in the tool. This compares well with the Zygo images in Figure 31 of the surface generated during the experiment from which this chip specimen was taken.

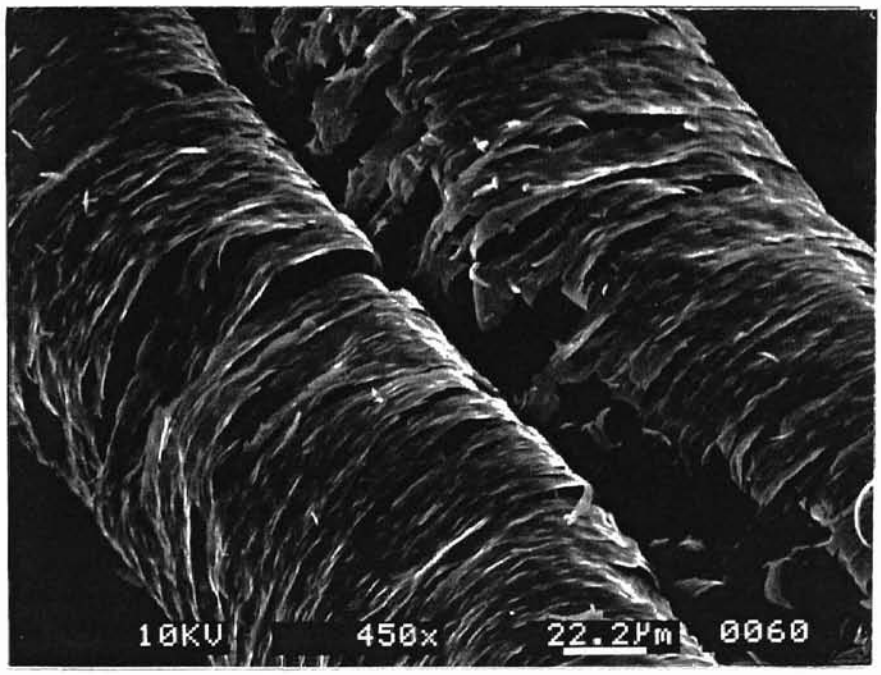

Figure 33. Form B chip from the front. Here the way the edges of the chip have curled inward can clearly be seen. The chip was generated at a t_o of 60 nm. The fractures in the chip are perpendicular to the cutting direction. The specimen was coated with AuPd prior to examination. The micrograph is at a magnification of 450X.

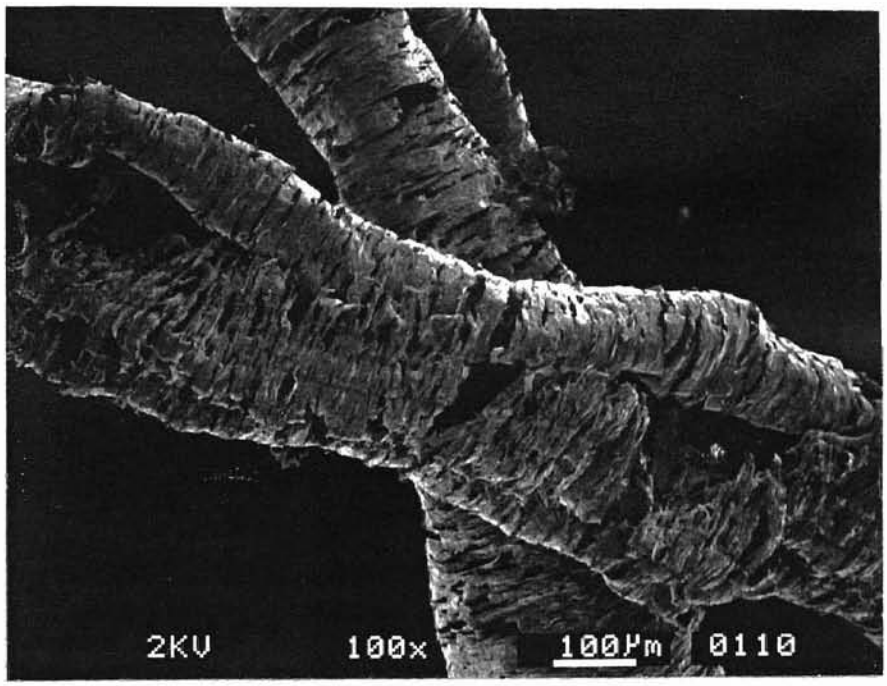

Figure 34. Uncoated Form B chips collected at a t_o of 110 nm magnified 100X. Comparison with the previous micrograph of a similar, but coated, chip clearly illustrates that at these magnifications coating the chips had no discernible effect (also compare with micrographs in Appendix A). The severely fractured appearance suggests the continued disintegration of the Form B chip into the Form C chip (compare with Figure 29 and Figure 33).

TABLE 4: **CHIP MORPHOLOGY BY UNCUT CHIP THICKNESS**

UCT (nm)	CHIP TYPE	COMMENTS
10	CHIP A[1]	Tightly coiled
10-40	CHIP A	After 15 nm chips are no longer tightly coiled
40	CHIP A	Loose
45	CHIP A	Loose
55	CHIP A & B	First String chips, also noticeable is a transitional chip that is somewhere between Form A and B
60	CHIP A & B	Same as 55 nm
65	CHIP A & B	Fewer Form A chips, greater number of transition chips
70	CHIP A & B	No transition chips, more Form A than Form B
80	CHIP A, B, & C	First significant appearance of Form C chips. Form B chips in greatest quantity, Form A chip least frequent.
85	CHIP A, B, & C	Quantities of Form B and C chips increase, Form A decreases.
90	CHIP A, B, & C	Almost equivalent amounts of Form B and C chips-slightly more Form B, very few Form A.
100	CHIP A, B, & C	Same as 90 nm
110	CHIP B & C	Same as 90 nm
120	CHIP B & C	Form C is now dominate chip form.
130	CHIP B & C	Frequency of Form B chip decreasing, almost no Form A chips
140	CHIP B & C	Same as 130 nm
150	CHIP B & C	Few Form B chips, almost no Form A
160	CHIP C	Few Form B chips, almost no Form A
160-400	CHIP C	Form C, note: increasingly less cohesion between particles.
400	CHIP C	Form C with no cohesion between particles.
>400	CHIP C	Form C with no cohesion between particles.

[1] See Figure 28, Figure 29, and Figure 30 for an explanation of chip types.

4.5.2 The Correlation Between Surface Quality and Chip Morphology

The correlation between chip structure and the surface generated at a particular uncut chip thickness is shown in the following plots. Figure 35 indicates the surface quality as a function of the uncut chip thickness. The possible range of for generating a non-pitted surface extends to a uncut chip thickness of approximately 100 nm. The likelihood of generating a non-pitted surface decreases with increasing uncut chip thickness; however, below an uncut chip thickness near 50 nm a non-pitted surface is always generated. The possible range of for generating a pitted surface extends from close to 50 nm up to the maximum uncut chip thickness. Above an uncut chip thickness in the range of 140 nm only a pitted surface can be generated for the given conditions. A mixed region, where both surfaces are possible at a given uncut chip thickness, exists between 50 and 90 nm. Specimens where the surface was characterized are noted in the figure to give an indication of the range of the data. Prior experience has shown that these specimens were representative of surfaces within the given ranges.

The ranges of chip morphologies as a function of uncut chip thickness is illustrated in Figure 36. The three chip forms have distinct ranges where they are generated. The Form A chip has the narrowest range extending only up to 110 nm; however, at uncut chip thicknesses at or below 50 nm only the Form A chip is formed. The Form B chip can be generated within the range of 50-160 nm which corresponds to the entire mixed chip region. The Form C chip is the only chip produced at uncut chip thicknesses greater than 160 nm but its range extends down to as low as 80 nm. The likelihood of producing a

Form C chip within the mixed range increases as the uncut chip thickness increases from 80 nm.

The correspondence between the surface generated at a given uncut chip thickness and the chip produced at that uncut chip thickness can be seen in Figure 37. The one to one correlation between chip and surface may prove useful for determining general surface quality in machining practice by observation of the chip structure. The determination of the ranges and zones for chip types and surface quality was made using chips collected

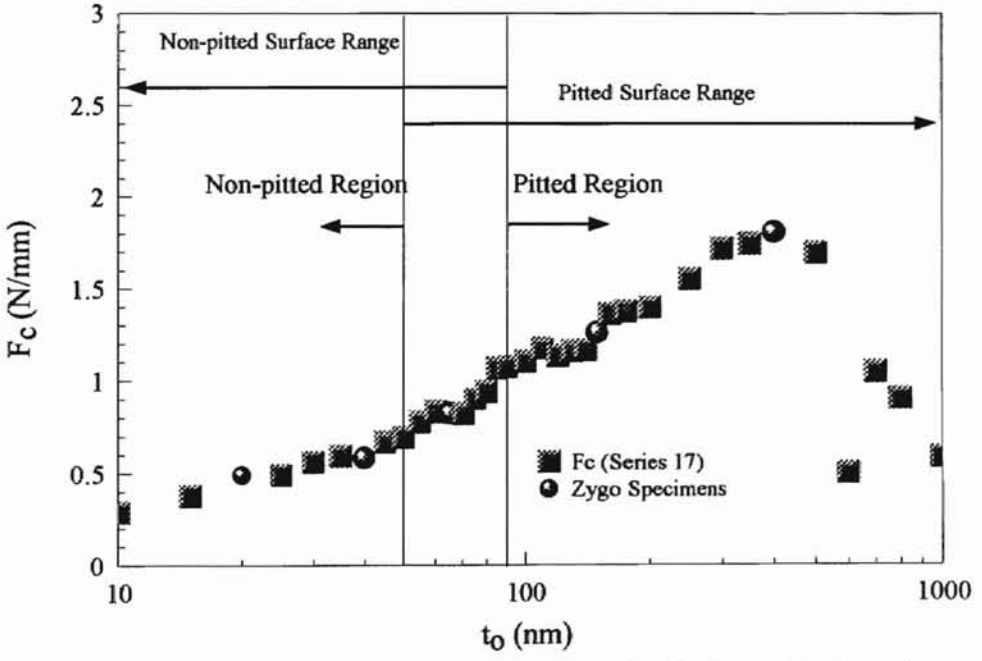

Figure 35. Relation between surface quality and uncut chip thickness. Surfaces that were inspected using the laser interferometric microscope are indicated on the plot. The non-pitted region extends down from an uncut chip thickness of approximately 50 nm while the pitted region extends upwards from an uncut chip thickness of approximately 90 nm. The middle region, 50-90 nm, is characterized by mixed behavior where either a pitted or a non-pitted surface is possible. The entire range of possible non-pitted behavior is indicated on the plot. The likelihood of a non-pitted surface in the mixed region decreases with increasing uncut chip thickness. The range of pitted surfaces extends from 50 nm to the maximum uncut chip thickness.

during the experiment 17 and surface characterizations done using a laser interferometric microscope. The ranges indicate the probability of encountering the specified surface quality or chip type not the possibility. As an example, a Form A chip might be produced at uncut chip thicknesses as high as 150 nm but only rarely, with perhaps one Form A chip being collected at that t_o during an experiment. In fact at uncut chip thicknesses lower than 150 nm there were instances where no Form A chips were produced. Based on these observations, the Form A chip range was selected to only include those uncut chip thicknesses where Form A chips were probable during the experiment as opposed to possible. The possibility of producing Form A chips extended through the entire mixed chip region.

The correlation between the range of the Form A chip and the range of non-pitted surfaces is evidence of a connection between the two. This interdependence suggests that Form A chips are only generated from non-pitted surfaces. The mixed chip region encompasses and extends beyond the mixed surface region. The mixed chip region is larger because there are three chip types as opposed to only two surface qualities.

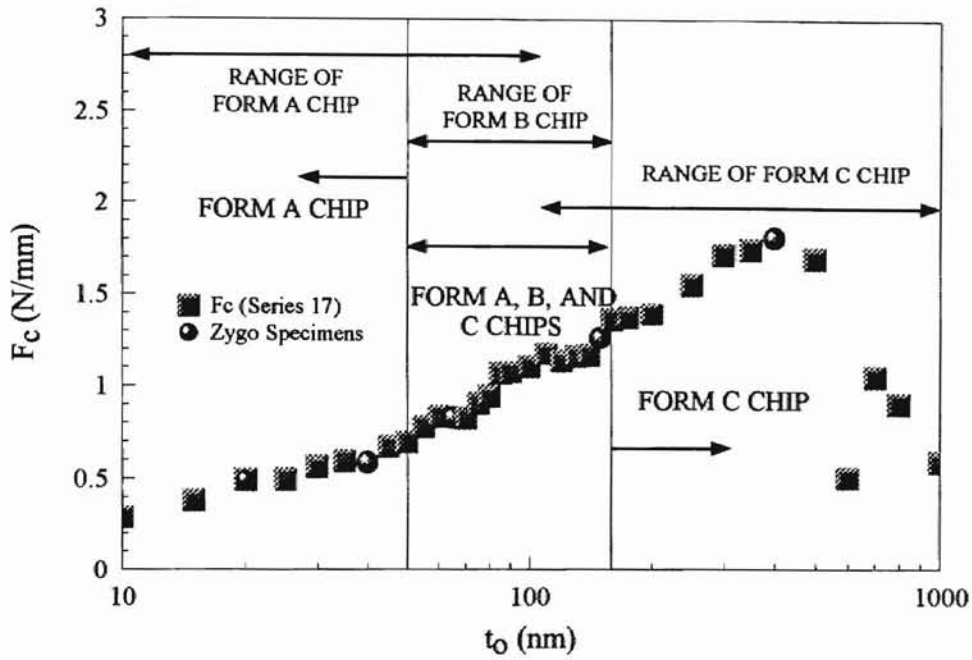

Figure 36. This figure shows the relation between chip types and uncut chip thickness. Specimens characterized using the laser interferometric microscope are also indicated. The Form A chip is the sole chip morphology in a uncut chip thickness range of or less than approximately 50 nm. The Form C powder chips are essentially the only chips that exist after a to of 160 nm. The middle region between 50 nm and 160 nm consists of both the Form A and Form C chips and is the sole range of the Form B chip. For an explanation of chip types see Figure 28 and Figure 30..

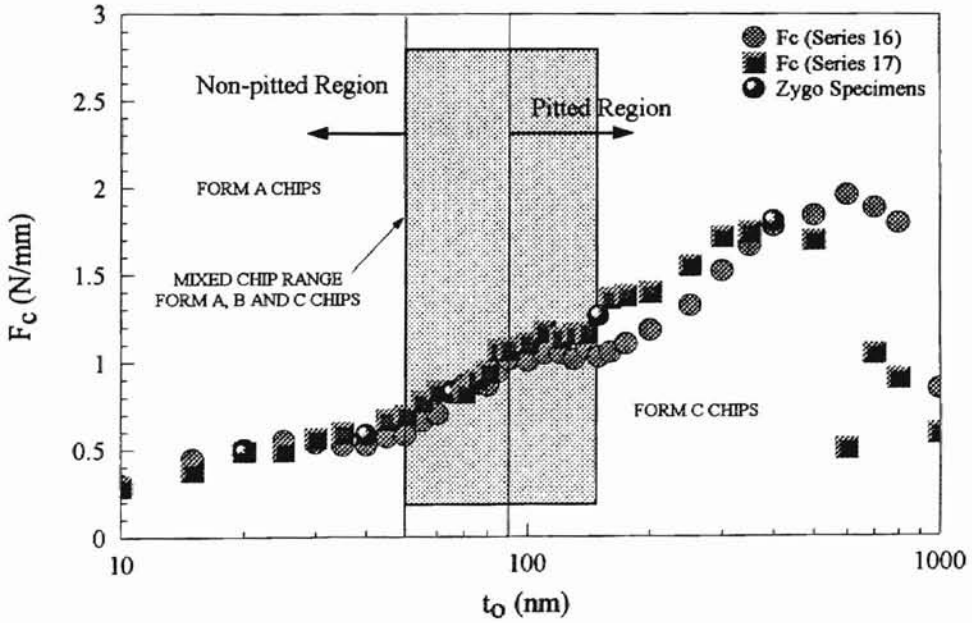

Figure 37. The correspondence between surface quality and chip morphology as a function of the uncut chip thickness. The large gray box indicates the range of the mixed chip morphology region which overlaps the mixed surface region as indicated. The Form A chip corresponds to the region of non-pitted surfaces while the Form C chip corresponds to surfaces that are pitted. As expected the mixed chip region corresponds to the mixed surface region with the major difference being the larger range of the mixed chip region. The range of the Form A chip ends at 100 nm, which roughly corresponds to the center of the mixed chip region.

4.6 Force Components as Functions of the Tool Edge Profile

The effect of tool geometry on the cutting process on a macroscopic scale is well understood, however, the effect of the local or effective tool edge geometry on cutting at very small uncut chip thicknesses is still under investigation. The effective rake angle resulting from machining at a t_o on the order of the tool edge radius has been shown to have a significant effect on the cutting process when cutting ductile materials as detailed by Lucca and Seo [1993]. Figure 38 is illustrative of the geometric effect of the relative magnitudes of the tool edge radius and the uncut chip thickness. The salient features of the tool edge profile are compared to the results obtained from the recorded force components in the series of plots presented in Appendix B. Although the speculative nature of these comparisons prevents their inclusion here, they suggest that the tool edge profile has a significant effect on the forces and energies in the cutting process.

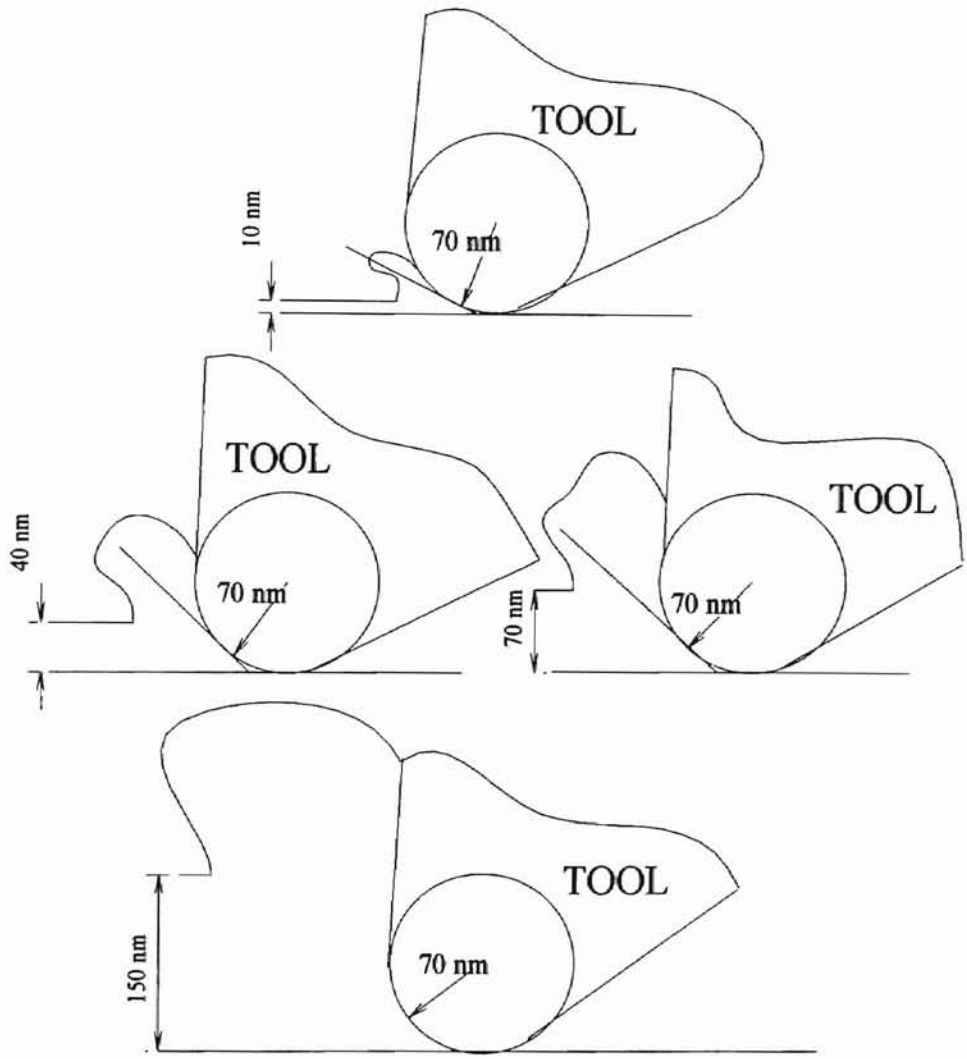

Figure 38. Schematic showing the relative comparison between the tool edge radius and the uncut chip thickness. The angled lines tangent to the tool edge represent the effective negative rake angle. Note that at a t_o that is approximately a factor of two times the tool edge radius the local tool edge geometry is clearly less of a factor as the global geometry of the tool becomes predominate. This figure is drawn to scale to give an accurate visualization of the process.

CHAPTER V

DISCUSSION OF RESULTS

The cutting process is defined by the interaction between the tool and workpiece. The forces, chip types, and resulting surface quality are results of this interaction and as such give clues to the process. Therefore, the correlation between features of the tool edge and events occurring in the force data, surface quality, and chip morphologies are important clues for determining the removal mechanism of the process.

5.1 Forces, Specific Energy, and Force Ratio

5.1.1 Cutting and Thrust Forces

For both the cutting and thrust force curves, events were consistently observed in Regions 1-3 (see Appendix B). Many of the specific events in these curves coincided with, or could be scaled to, features of the tool edge. The consistent occurrence of curve

features at points relating to the size of tool edge features is suggestive of the role the tool edge profile plays in the cutting process at small uncut chip thicknesses.

One of the most important trends in the force data is the increase in the magnitude of the thrust force at a given point from one series to the next series (refer to Figure 19). This may be explainable if one considers wear of the tool from one experiment to another. The difference is most pronounced at the lower uncut chip thickness range (below 100 nm) which is where small changes in the tool edge profile due to tool wear would be expected to have the greatest impact on the cutting process. That the wear in the tool was not evident in the cutting forces does not necessarily negate this explanation. Data reported by Lucca and Seo [1994] for ductile materials comparing forces taken using a well worn tool and forces taken using a new tool showed much smaller differences between cutting forces than between thrust forces. The differences, it would be would be even smaller here, perhaps small enough that they would be masked by the general spread in the data. This is especially so when considering the amount of wear expected from one series of cuts, where the typical cutting distance is less than 1 km.

5.1.2 Specific Energy

Specific energy has extensively been used to characterize the cutting process . In micro-cutting it has long been observed that for ductile materials the specific energy increases as the uncut chip thickness decreases. Lucca and Seo [1991], using a simple force balance, established that the observed energies were not accounted for by shearing in

the shear zone and rake face friction. Explanations for the observed behavior include the apparent increased importance of sliding on the flank face, due to the elastic recovery of the material behind the tool edge, and plowing at the tool edge due to the high effective negative rake angle that results when the uncut chip thickness is around or less than the tool edge radius. This behavior is illustrated in diagrams shown in Figure 14 and Figure 38, in Chapter 4.

Although similar behavior has been suggested for brittle materials (e.g., Furukawa, 1988), it has not been established conclusively because data reported in the literature only extend down to a t_o of 0.5 μm. There is similarity between the trends in specific energy reported by Furukawa [1988] and those shown here, with differences attributable to the polycrystalline Ge used by Furukawa. Clearly, from the data in Chapter 4, the trend noted for micro-cutting of ductile materials is also evident for Ge.

5.1.3 Force Ratio

The force ratio gives the direction of the resultant force vector during the cutting process and, as such, indicates whether the process is dominated by the thrust force component or the cutting force component. A force ratio greater than one is indicative of a thrust force dominated process while a ratio less than one is characteristic of a cutting force dominated process. A thrust force dominated process is suggestive of a process where plowing and sliding are major mechanisms of energy dissipation.

As the thrust force component becomes dominant, the resultant force vector rotates toward the workpiece, whereas when the cutting force dominates the resultant force vector rotates to the cutting direction. As the cutting force becomes dominant tensile stresses are developed in the workpiece behind the tool tip [Blackley and Scattergood, 1990]. This is of special concern when cutting brittle materials which are typically weak in tension. The appearance of tensile stresses behind the tool tip can lead to micro-cracks and pits which damage the surface quality of the final workpiece. It is for this reason that the force ratio is expected to be an important predictor of machining damage in machining brittle materials.

The arctangent of the force ratio gives the direction or angle of the resultant force vector. Here, an angle less than 45° denotes a process dominated by the cutting force and an angle greater than this indicates a process where the thrust force is dominate. Typically for ductile materials there is a shift from a thrust dominated process to a conventional material removal process, over the uncut chip thickness range from 10 nm to 20 μm as the resultant force vector rotates through the 45° angle denoting the transition point. This transition for ductile materials generally takes place at a t_o on or about 100 nm, as shown by Seo[1993].

Figure 22, in Chapter 4, indicates that by the above criteria the cutting process for Ge is thrust force dominated over the entire reported range since the angle of the resultant force vector never drops below 60°. This is in contrast to the typical behavior for ductile materials reported by Seo, where the angle of the resultant force vector rarely exceeded

70° and then only at the smallest uncut chip thicknesses. The domination of the cutting process by the thrust force component is consistent with the high indentation hardness of Ge (760 HV).

5.2 Surface and Chip Morphologies

5.2.1 The Correlation Between Surfaces and Chips

There is a close association between the surface quality and the chip morphology. The relation between the specimens surface and the chip generated is illustrated in Chapter 4, where features from a 10 nm chip (Figure 28) coincide with those seen on the surface which was generated at 10 nm (Figure 31). Regions of surface quality and chip ranges were identified in Chapter 4. The Form A chip clearly coincides with the generation of non-pitted surfaces; while, the Form C structure coincides with heavily pitted surfaces. Because of the instability in the mixed region it was not possible to clearly identify the surface quality associated with the Form B chip structure.

The mixed chip region extends from the end of Region 1 up to the approximate range of Region 3 and the corresponding mixed surface region extends from the end of Region 1 to just before the start of Region 3 (roughly 110 nm). These ranges may be significant in determining the behavior during the cutting process. The unstable surface character in the mixed zone and the changing chip morphologies in the corresponding mixed chip region clearly show that a transition is taking place. The reasons for the

instability are less definite, but that it so closely correlates with features of the tool edge is very suggestive of a process in transition due to a changing interaction between the workpiece and the cutting tool. It seems most likely that this changing interaction is the result of the size effect, when cutting at a uncut chip thickness much smaller than the tool edge radius up to a uncut chip thickness of approximately twice the value of the tool edge radius (refer to Figure 14 and Figure 38). As the uncut chip thickness approaches a value greater than twice the tool edge radius, signs suggest that the transition is from process dominated by the tool edge geometry to one dominated by the global tool geometry.

The occurrence of force fluctuations over a range of uncut chip thickness coincides with the unstable region of behavior. This suggests that the varying force levels are the result of the unstable interaction between the workpiece and tool which is consistent with the different chip morphologies and surfaces generated. The one to one correlation between chip morphology and surface quality suggests that the chip structure may be a useful tool for determining surface quality in machining practice thus eliminating the need for time consuming surface characterizations.

Surface ranges and chip ranges do not exactly match because of the unstable nature of behavior at uncut chip thicknesses in the transition region. If there is a direct correlation between the force level, the chip produced, and the surface generated, then the quality of the surface inspected at a given uncut chip thickness would depend on the last tool pass. This makes it possible to collect chips at a given uncut chip thickness that do not necessarily correlate with the surface eventually characterized at that uncut chip thickness. For this reason, the boundaries to chip and surface ranges are inexact which

explains why the non-pitted surface range ends at 90 nm while the range of Form A chips extends to 100 nm and have even been observed at higher uncut chip thicknesses. Additional vagueness is introduced by using discrete data points. The combination of unstable behavior and the use of discrete points makes it difficult to definitively pin down the behavior at a given uncut chip thickness, or range of uncut chip thicknesses, therefore statements are based on the probability of occurrence rather than the possibility.

5.2.2 Critical Uncut Chip Thickness

The existence of a critical uncut chip thickness is suggested by the correlation between force level, chip morphology, and surface quality. The critical uncut chip thickness is the highest uncut chip thickness where an apparently non-pitted surface can consistently be observed. The threshold or mixed behavior boundary value of 50 nm determined for these experiments may well represent the critical uncut chip thickness ; however, due to the instability in the transition zone, the actual critical uncut chip thickness was not determined. There is reasonable agreement between the threshold value determined here and the work reported by Blake and Scattergood [1990]. They indicated a critical or transitional depth of cut range of 20-300 nm for machining Ge on the (100) face with the exact value depending on factors such as nominal rake angle of the tool and feed rate. There is a great deal of latitude in these comparisons due to the large differences between the experiments in the geometry, tool, and workpiece but the correspondence is at least reasonable.

5.3 Tool Edge Profile

The correlation between events in the force curves, the variation in surface quality as a function of uncut chip thickness, the changing chip morphologies, and the size of features from the tool edge supports the hypothesis that the governing removal mechanism is changing as the uncut chip thickness increases from tens of nanometers to the micron order. The exact reasoning for the unstable behavior is not as evident; however, based on the data collected, it seems clear that the local characteristics of the tool edge have a definite effect on the cutting process. This can be seen in the consistency of events in the force data, the specific energy curves, and the force ratio curves (see Appendix B). In each case, specific events occur at uncut chip thickness values that can be linked to features of the tool, including the tool edge radius, twice the tool edge radius, and the estimated wear flat length. The consistency of events in Region 3 strongly suggests that this is the region where the dominance by the local tool edge geometry is giving way to the dominance of the global tool geometry. This is supported by the scaled drawing in Figure 38, in Chapter 4, showing the interaction between the tool and workpiece at various uncut chip thicknesses. Although the events observed in Region 3 cannot be attributed directly to either the effect of the estimated wear flat length, or a scaled value of the tool edge radius, the general reasoning of a transition in the importance of the tool edge geometry is still consistent since both of these factors relate to the local tool edge geometry.

CHAPTER VI

CONCLUSIONS AND RECOMMENDATIONS

6.1 Conclusions

Orthogonal cutting was performed enabling careful study of the force behavior. Machining was performed on the (100) plane in the [$\bar{1}$00] direction at a nominal speed of 48 m/min without a lubricant. Four series of cutting and thrust force data were taken and compared over a broad range of uncut chip thicknesses (10 nm - 1.5 μm). The single crystal diamond tool used in the experiments was characterized using atomic force microscopy to determine the tool edge profile. Generated surfaces were characterized using a laser interferometric microscope. Chips were collected and studied using scanning electron microscopy. The following conclusions were drawn:

1. The specific energy of the system was seen to increase dramatically at uncut chip thicknesses less than approximately 50 nm. The observed behavior is consistent with that reported in the literature by Furukawa et al. [1988] and is also consistent with behavior noted for ductile materials.

2. The tool edge radius has a significant effect on the force system behavior and the energy dissipated in the orthogonal ultraprecision machining of Ge. The tool edge radius, 60-70 nm, consistently correlated with features in curves presenting the measured force level as a function of uncut chip thickness.
3. Non-pitted surfaces were consistently generated at uncut chip thicknesses of or below 50 nm; whereas, surfaces generated at uncut chip thicknesses greater than 90 nm were marked by increasingly greater pitting damage. Behavior of the cutting process at uncut chip thicknesses in the range between 50 and 90 nm was unstable such that surfaces produced in this range were inconsistent from experiment to experiment. The unstable region may correspond to the transition from a process dominated by local tool edge features to a process dominated by global tool geometry.
4. Three chip structures were observed during the cutting process. These chips corresponded to the generated surfaces and are useful indicators of the quality of the generated surface.

6.2 Recommendations

This study was conducted using only one orientation of Ge and one tool. The next obvious step would be to reproduce these experiments using different tools to better assess the effect of the tool edge on the process. Preliminary experiments performed on a Ge specimen of unknown orientation produced comparably different results than those

reported here suggesting that further experiments on different orientations of the Ge workpiece would be valuable. Additionally, an effort should be made to develop a force model for two-dimensional cutting and correlate it with the forces reported here, as well as the model presented by Blackley and Scattergood [1990].

The depth of the subsurface damage generated in machined specimens is also of concern and should be investigated. Preliminary results on this topic using specimens generated during the experiments reported here have been reported by Lucca et al. [1995].

BIBLIOGRAPHY

1. Blackley, W. S. (1990), Single Point Diamond Turning of Brittle Materials, M. S. Thesis, North Carolina State University, Raleigh, NC.

2. Blackley, W. S., and Scattergood, R. O. (1990), "Crystal Orientation Dependence of Machining Damage--A Stress Model", J. Am. Ceram. Soc., Vol. 73, No. 10, pp. 3113-3115.

3. Blake, P. N., and Scattergood, R. O. (1990), "Ductile-Regime Machining of Germanium and Silicon", J. Am. Ceram. Soc., Vol. 73, No. 4, pp. 949-957.

4. Digital Instruments (1992), Nanoscope® III Scanning Probe Microscope Control System: User's Manual, Version 2.5, December.

5. Furukawa, Y., and Moronuki, N. (1988), "Effect of Material Properties on Ultra Precise Cutting Processes", Annals of the CIRP, Vol. 37, No. 1, pp. 113-116.

6. Ikawa, N., Donaldson, R. R., and Komanduri, R. (1991), "Ultraprecision Metal Cutting -- The Past, the Present and the Future", Annals of the CIRP, Vol. 40, No. 2, pp. 587-594.

7. Lee, W. B., and Zhou, M. (1993), "A Theoretical Analysis of the Effects of Crystallographic Orientation on Chip Formation in Micromachining", Inst. J. Mach. Tools Manufact., Vol. 33, No. 3, pp. 439-447.

8. Lucca, D. A., and Seo, Y. (1993), "Effect of Tool Edge Geometry on Energy Dissipation in Ultraprecision Machining", Annals of the CIRP, Vol. 42, No. 1.

9. Lucca, D. A., Rhorer, R. L., Seo, Y., and Komanduri, R. (1991), Energy Dissipation in Ultra-Precision Machining", Proceedings of the 1991 NSF Design and Manufacturing Systems Conference, University of Texas, Austin, TX, Jan 9-11, Society of Manufacturing Engineers, pp. 263-267.

10. Lucca, D. A., and Seo, Y. (1989), "Prediction of the Partitions of Energies and Temperatures in Orthogonal Ultraprecision Machining", The ASPE/5th International Precision Engineering Seminar, Monterey, CA, Sept. 18-22.

11. Lucca, D. A., and Seo, Y. (1994), "Aspects of Surface Generation in Orthogonal Ultraprecision Machining", Annals of the CIRP, Vol. 43, No. 1, pp. 43-46.

12. Lucca, D. A., Seo, Y., and Rhorer, R. L., (1994), "Energy Dissipation and Tool-Workpiece Contact in Ultra-Precision Machining", Tribology Transactions, Vol. 37, No. 3, pp. 651-655.

13. Lucca, D. A., Seo, Y., and Wang, Y. M. (1995), "Subsurface Damage of Ultraprecision Machined Germanium", Synopsis: International Tribology Conference, Yokohama, Japan.

14. Moriwaki, T. and Okuda, K. (1989), "Machinability of Copper in Ultra-Precision Micro Diamond Cutting", Annals of the CIRP, Vol. 38, No. 1, pp. 115-118.

15. Nakasuji, T., and Kodera, S. et al. (1990), "Diamond Turning of Brittle Materials for Optical Components", Annals of the CIRP, Vol. 39, No. 1, pp. 89-92.

16. Puttick, K. E., et al. (1989), "Single-Point Diamond Machining of Glasses", Proc. R. Soc. Lond. A, Vol. 426, pp. 19-30.

17. Rank-Pneumo (1990), "Operating and Maintenance Manual of ASG-2500 Aspheric Generator", Rank-Pneumo: A Division of Rank Taylor Hobson Inc., Keene, NH.

18. Seo, Y. (1993), Energy Dissipation in Orthogonal Ultra-Precision Machining, Ph.D. Dissertation, Oklahoma State University, Stillwater, OK.

19. Sugano, T., and Goto, T. (1987), "Diamond Turning of an Aluminum Alloy for Mirror", Annals of the CIRP, Vol. 36.

20. Syn, C. K., Taylor, J. S., and Donaldson, R. R. (1988), "Ductile Brittle Transition of Cutting Behavior in Diamond Turning of Single Crystal Si", 1988 Annual Spring Meeting of the Japan Society of Precision Engineering, Meiji University, Kawasaki, Japan, March 16-18.

21. Taylor, J. S., Syn, C. K., and Donaldson, R. R., (1987), "Observations of Brittle-to-Ductile Cutting Mode Transition During Diamond Turning Tests of Single Crystal Silicon", Presented at the 2nd Ann. ASPE Conf., Columbus, OH.

22. Zygo (1992), MetroPro™ User's Guide OMP-0289C, July.

APPENDIX

Appendix A: Micrograph Gallery

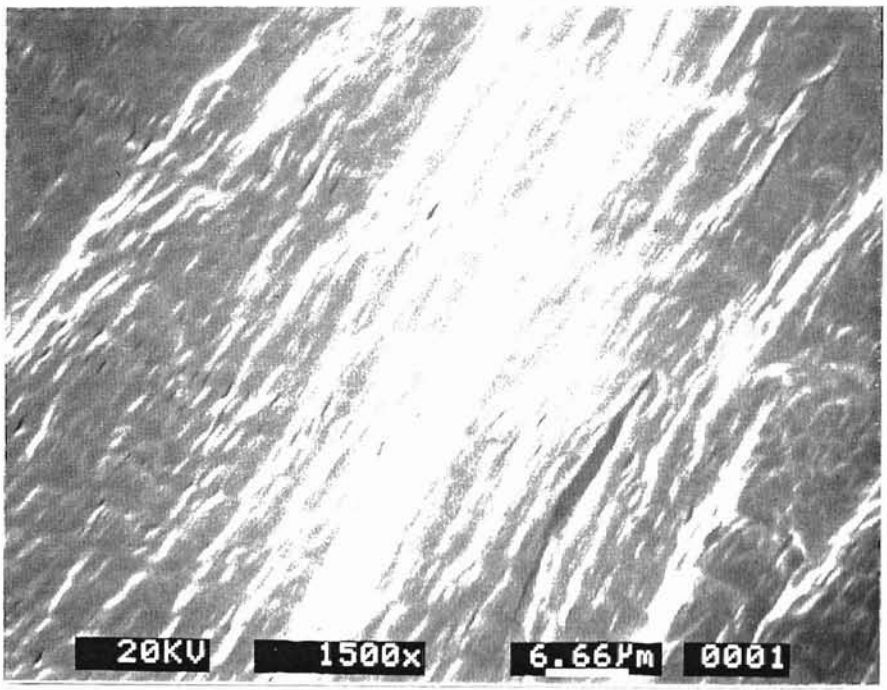

Figure 39. Uncoated Form A chip at 1500X magnification. The chip was generated at a t_o of 45 nm. Compare this figure with Figure 40 of a coated chip generated at a t_o of 40 nm. The similarity in structure between this chip and the 40 nm chip, which is magnified 800X, suggests that the coating of AuPd on the later chip has had a negligible effect on the image.

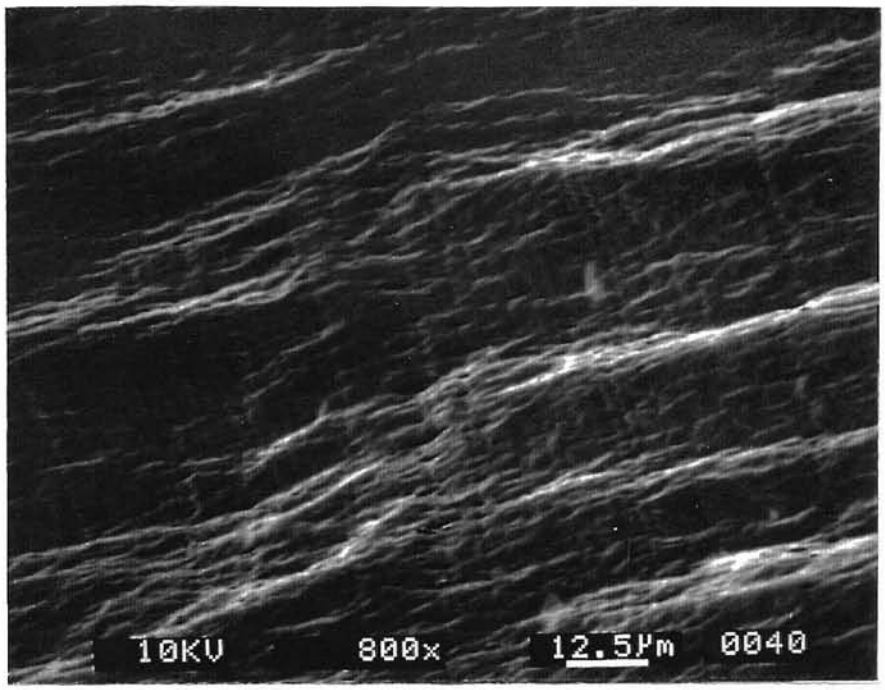

Figure 40. 40 nm Form A chip at 800X magnification. This is an image of the center portion of the chip. Note the numerous fractures perpendicular to the cutting direction. This chip was coated prior to SEM examination. Compare with the features of the chip in Figure 39.

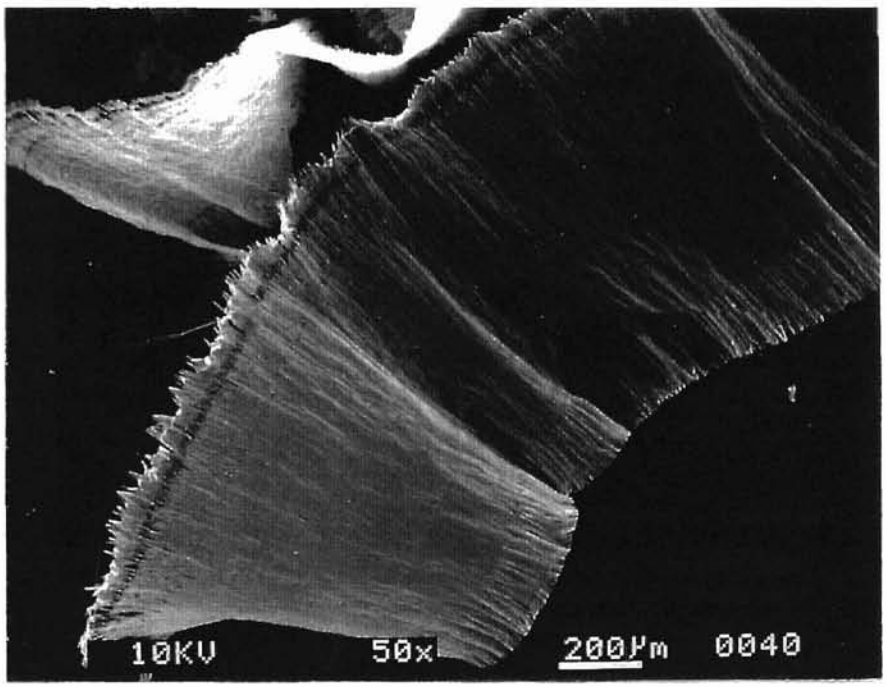

Figure 41. Form A chip generated at a 40 nm uncut chip thickness magnified 50X. Compare with Figure 28 which is of a 10 nm chip. Chips generated at a t_o greater than 20 nm are not as corrugated or as tightly wound as those chips generated at lower t_o. This specimen was coated prior to examination.

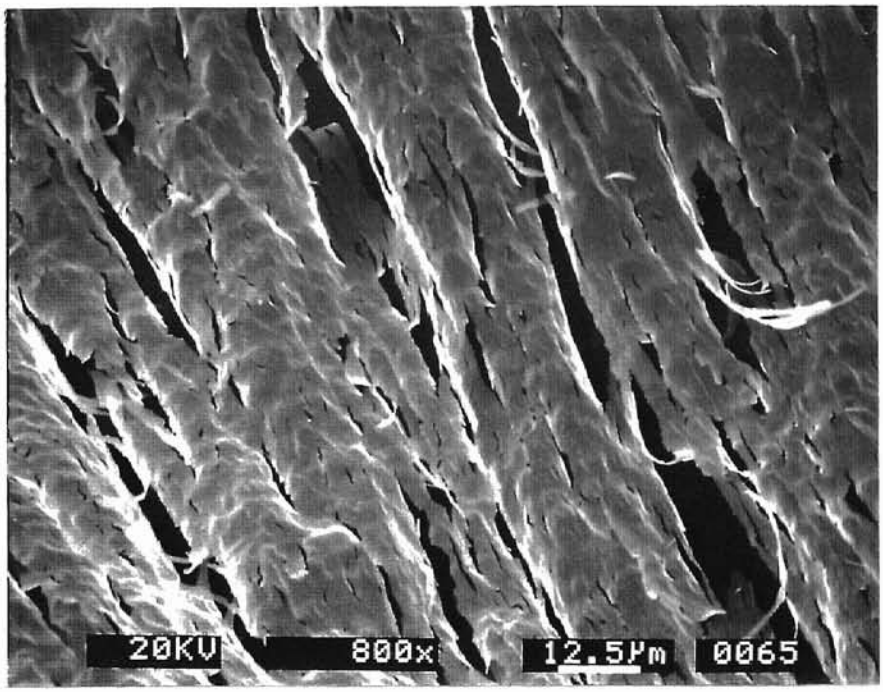

Figure 42. A Form B chip generated at a uncut chip thickness of 65 nm magnified 800X. This image is of the back of the chip. The numerous fractures are perpendicular to the cutting direction. The chip was coated prior to inspection.

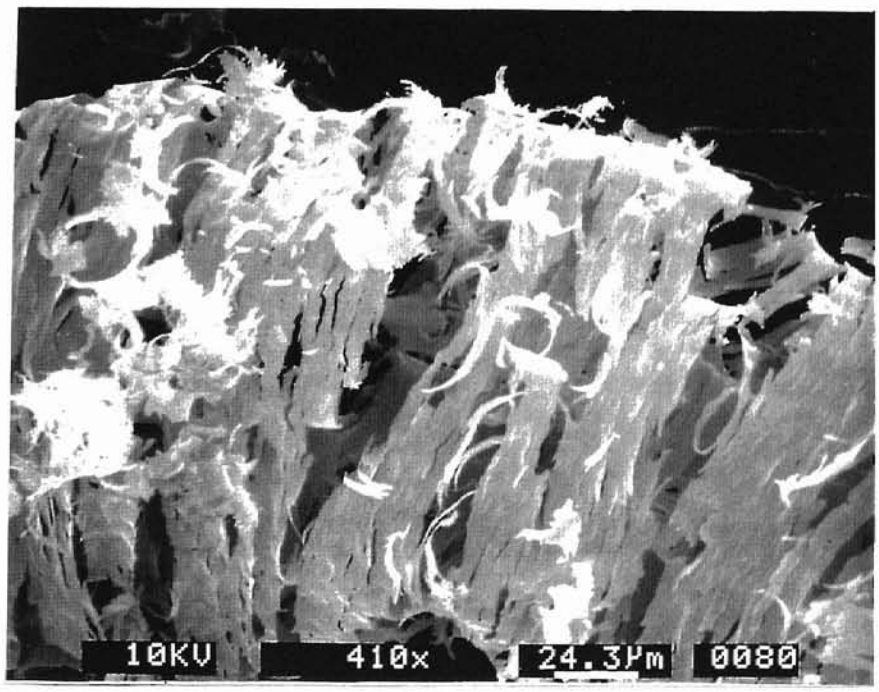

Figure 43. Form B chip at 410X magnification. This chip was collected at a t_o of 80 nm. Note the heavily degenerated Form and compare with the powder bundles pictured in Figure 29, Figure 30, Figure 47, and Figure 46.

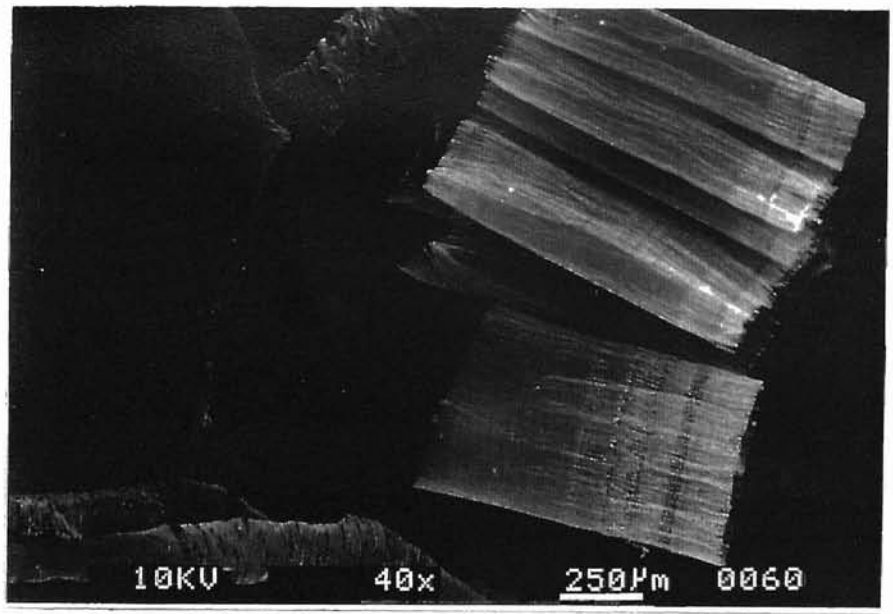

Figure 44. Group of chips collected at a t_o of 60 nm. This illustrates the occurrence of two chip types at one uncut chip thickness. Both the tubular Form B chip and the ribbon structured Form A chip are shown here. Magnification is 40X. The specimen was coated prior to examination.

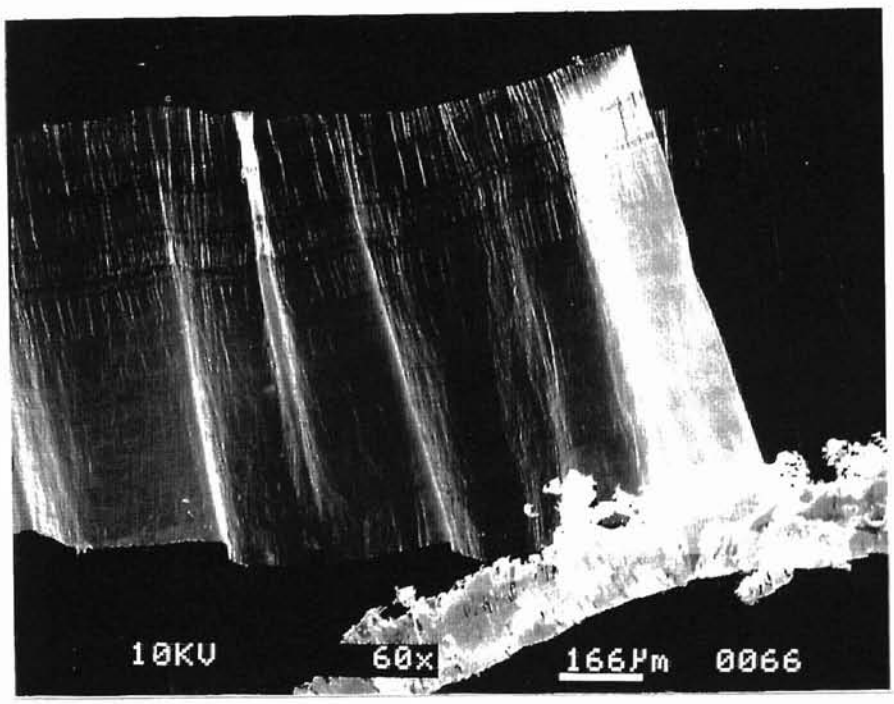

Figure 45. This micrograph illustrates the two chip types present at a 65 nm uncut chip thickness. The Form B chip is badly frayed on the edges and may be a precursor to the further degenerated Form B chips seen at larger t_o's. Note the bands on the surface of the Form A chip which trail off at an angle. These correspond to the knife marks created on the specimen surface. The angle of the marks is due to the arc of the tool's rotation. Magnification is 60X.

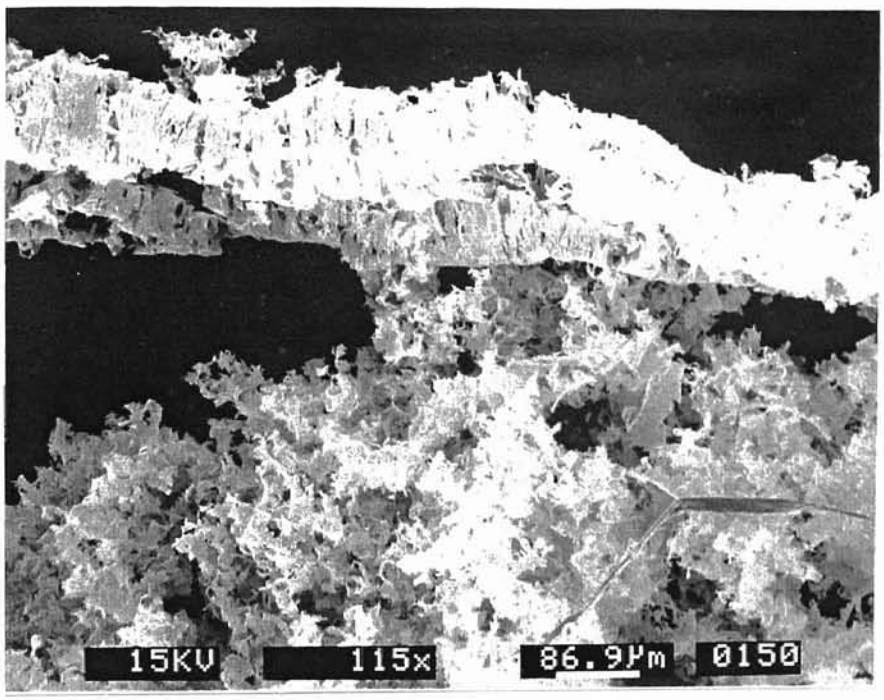

Figure 46. Chips generated at an uncut chip thickness of 150 nm magnified 115X. Pictured here are a Form B chip and a Form C chip. Note that the Form C chip looks like a collection of fragments of a Form B chip. The Form B chip is clearly in transition to the completely fragmented Form C chip.

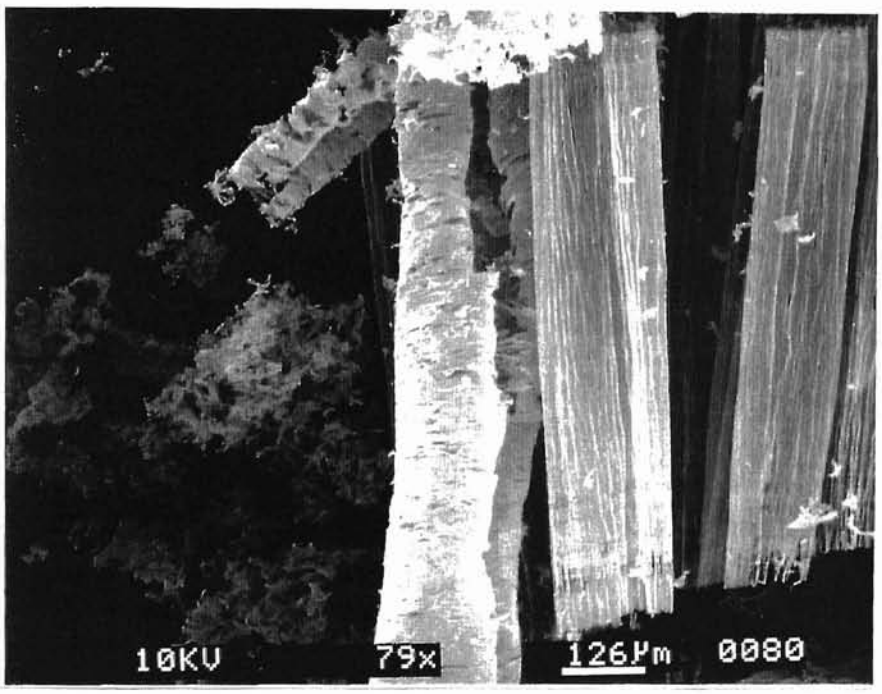

Figure 47. Mixed chips collected at a t_o of 80 nm magnified 79X. Pictured are a Form A chip, two Form B chips, and a Form C chip.

Appendix B: Speculation on the Effect of the Tool Edge Profile

Repeatability

Figure 48-Figure 51, present the magnitudes of each force signal along with the resulting averaged value to give an indication of the spread within the data from a particular experiment as compared to features of the tool. The agreement between different signals at a given uncut chip thickness is generally within a 30 percent total variation. Trends in the spread of the data are consistent from experiment to experiment. The scatter in the data is lowest at the lower uncut chip thicknesses and is typically much lower for thrust forces than for cutting forces except at t_o less than 40 nm, where the consistency between cutting forces is greater than that for thrust forces. There is less variation in the force levels at the higher uncut chip thicknesses, after approximately 500 nm. These trends are evident in the data from each series.

Referring to Figure 48-Figure 51, the spread in the data is reasonably steady up until the end of Region 1, at or about a t_o of 45 nm, after which a significant increase in the variability of the signal step height becomes evident for the cutting force data. The spread in the thrust force data is lowest up to uncut chip thicknesses at or about the magnitude of the tool edge radius after which the spread is generally much greater. There is no corresponding effect from the tool edge radius on the scatter in the cutting force data.

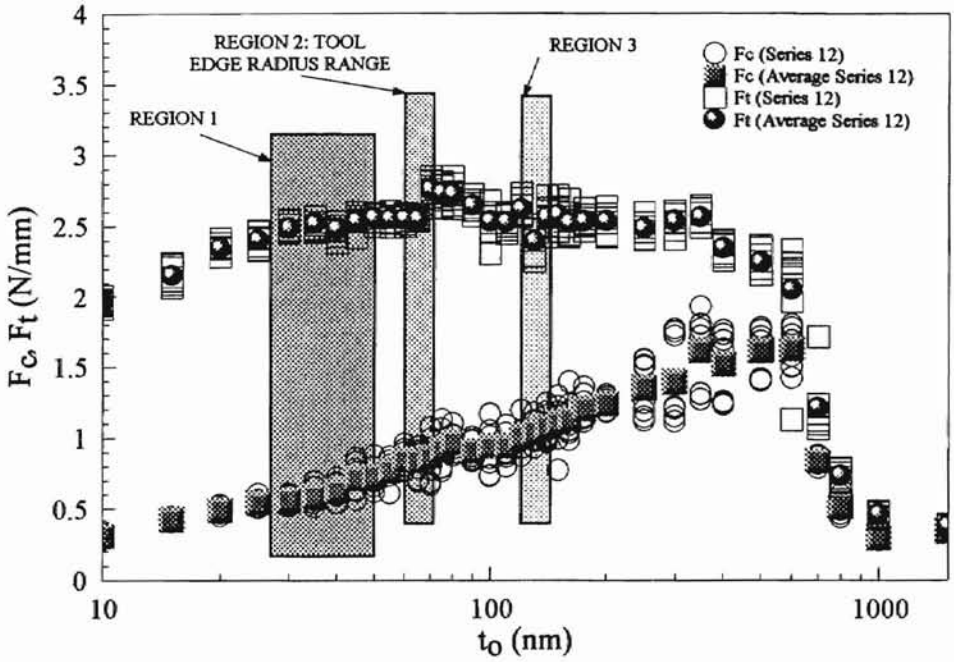

Figure 48. Data recorded during Series 12. This figure illustrates the scatter within the series data as compared to the size of characteristics of the tool edge.

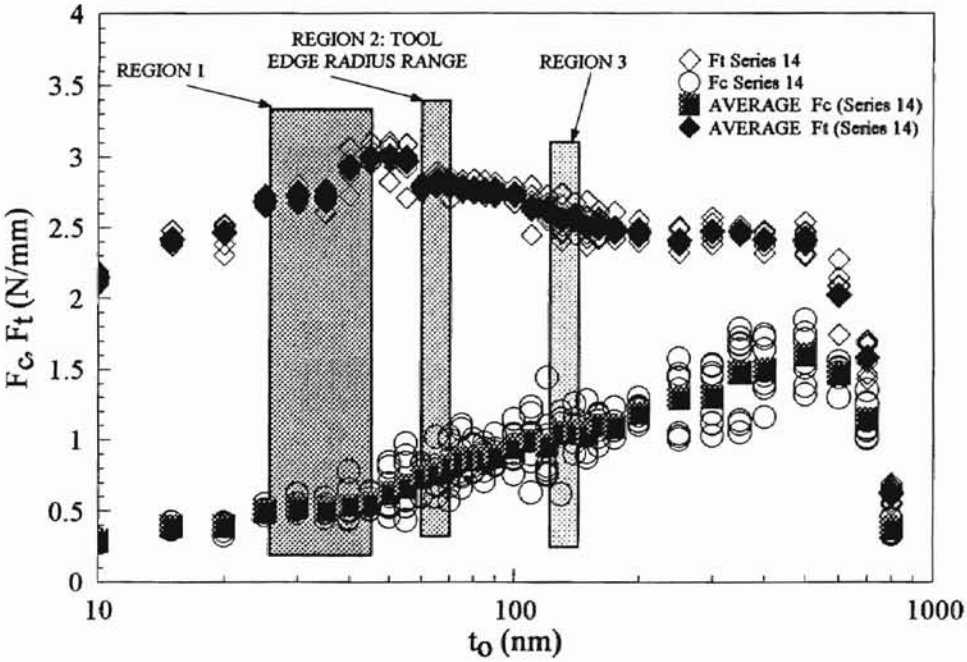

Figure 49. Comparison of the spread in data from series 14 with the size of tool edge characteristics.

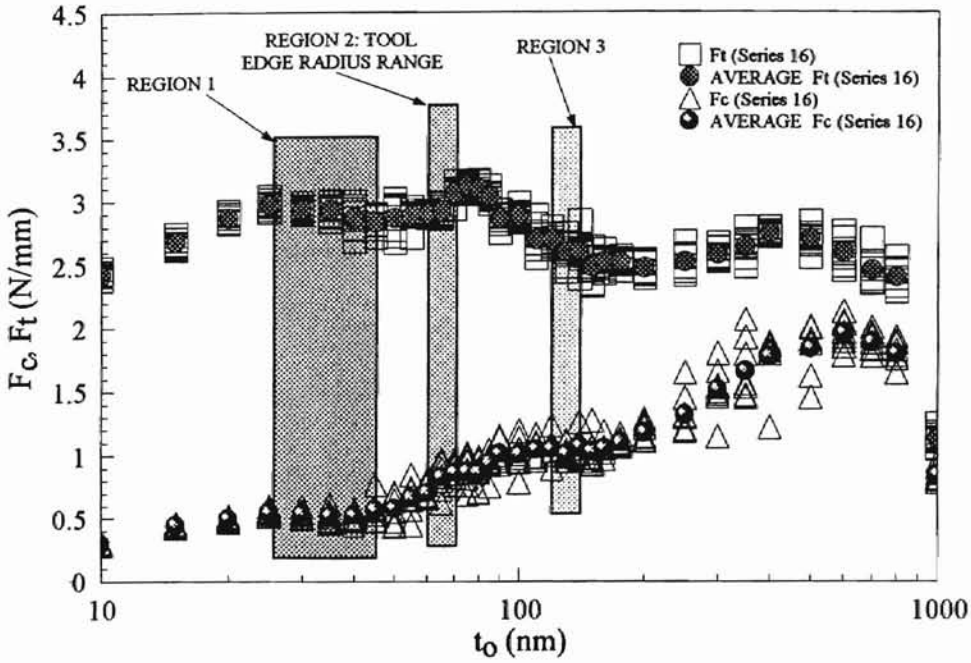

Figure 50. The size of local tool edge features as compared to the variability in data collected from Series 16.

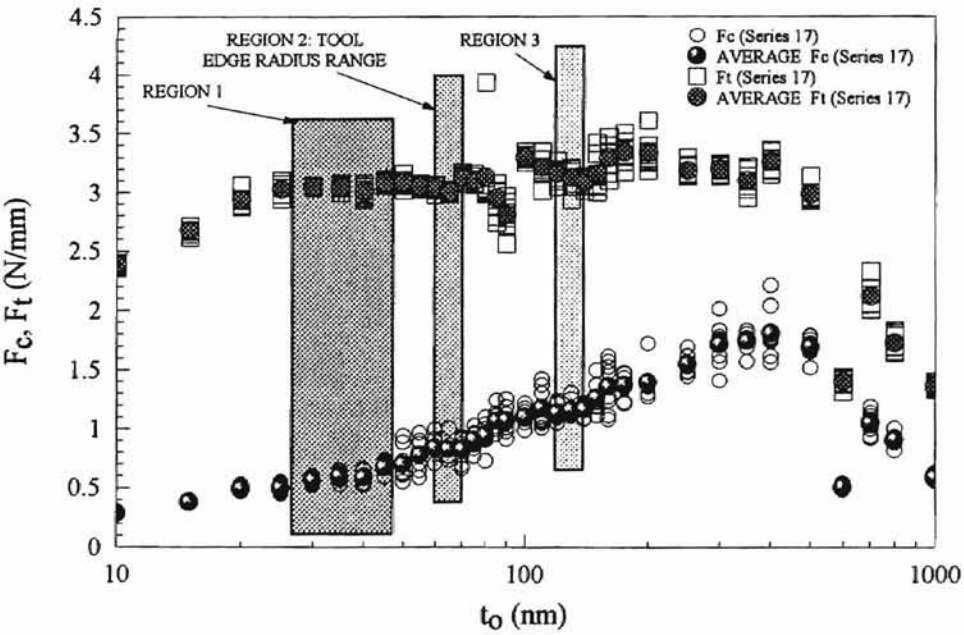

Figure 51. Size ranges for characteristics from the tool edge profile as compared to spread in data recorded during experiment 17.

Cutting Forces

The average cutting force for each series is plotted in Figure 53-Figure 56. These figures indicate specific trends that are consistent between the experiments and compares some of these features with the size of attributes from the tool edge profile. The consistency of these trends from experiment to experiment, as well as through the general scatter in the data, suggests that they are functions of process behavior. The initial trend, at the lower uncut chip thickness range from 10-30 nm, is an approximately linear increase. At approximately the 30 nm uncut chip thickness, a noticeable change in the slope of the curve is evident which in most of the experiments (with the exception of Series 12) resulted in a plateau feature in Region 1 (25-50 nm). Following this plateau feature, another approximately linear increase in the cutting force is evident. In most cases, the slope of this portion of the curve changes at approximately 60 nm and is followed by a small plateau feature which lasts until roughly 70 nm. This second plateau, termed Region 2, is particularly relevant considering that, as shown in the figures, this is the range of the actual tool edge radius (60-70 nm) which was obtained from AFM scans. That there is a consistent leveling of the data on, or about, this range is, perhaps, an important clue about the interaction of the tool with the workpiece.

The tool edge plateau is generally followed by another practically linear increase which ends in Region 3, the last of the plateau formations. The occurrence of this final event, or feature, is less consistent from series to series. Although each series has the third plateau region following the increasing slope from the tool edge plateau, the occurrence is not consistently in the same range of uncut chip thicknesses or of the same duration. The

last plateau is most pronounced for series 16 and least pronounced for series 14, where the slope levels but is not horizontal. The last plateau generally occurs in a uncut chip thickness range which corresponds to approximately twice the measured tool edge radius (120-140 nm). This is also the approximate range for the estimated length of the wear flat shown in Figure 13. The measured value for the slider length is approximately 140 nm ; however, the actual value is expected to be less due to the distortional effects during scanning discussed earlier. The comparison between the 150 nm uncut chip thickness and the 70 nm tool edge radius in Figure 38 shows that this is the approximate point where the global tool geometry begins to dominate over the local edge geometry. One or both of these possibilities may explain the consistent appearance of the third plateau feature and the following inflection point in Region 3. The final two generalized stages or regions are a steady increase ending at a uncut chip thickness of approximately 600 nm and the following dramatic drop in force values. These trends have been broken down into a generalized cutting force curve which is presented in Figure 52. The consistency between the generalized features and the actual data is illustrated in Figure 57 where the generalized curve is traced onto the actual data from series 16.

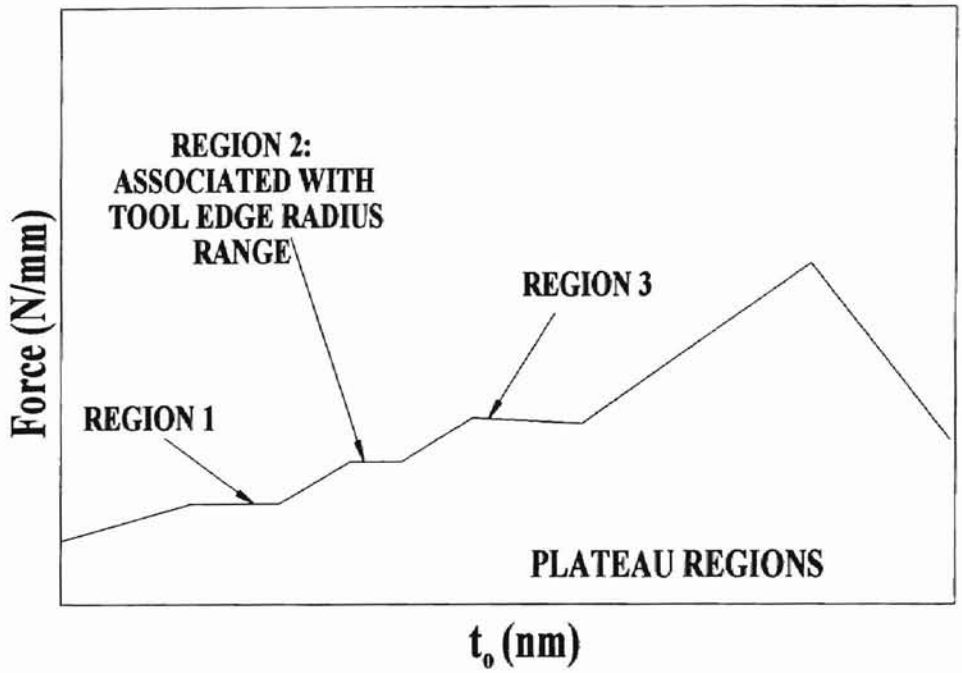

Figure 52. Generalized cutting force curve illustrating the consistent trends between the various cutting force curves. Regions are highlighted that correspond to the size of features from the tool edge profile and consistent points of interest.

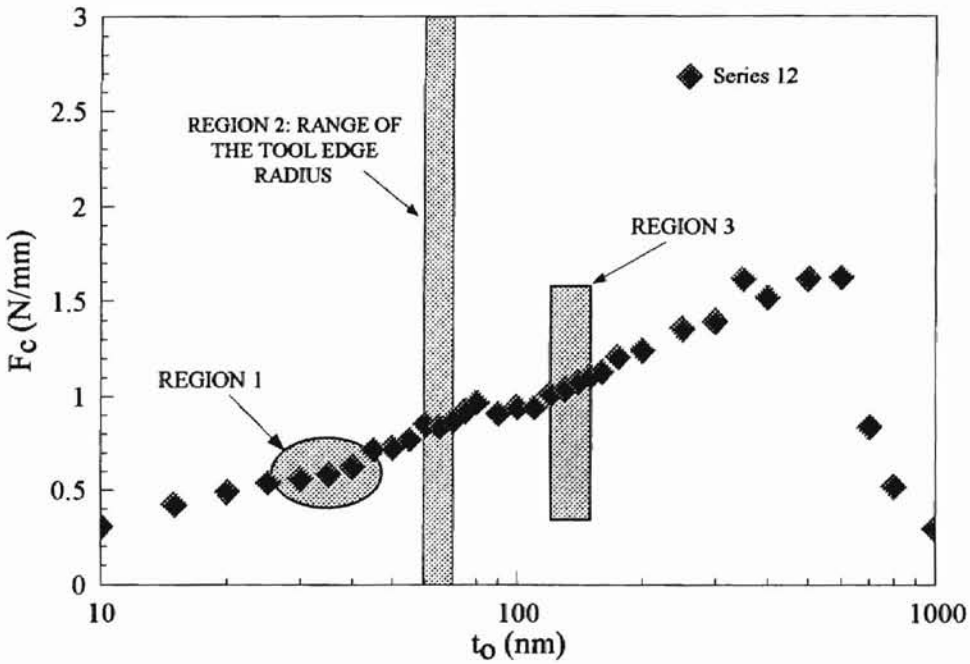

Figure 53. Cutting force data from data series 12. The correspondence between this curve and the generalized curve is quite good. Notable differences include the slight slope of the plateau in Region 1 and the appearance of the plateau prior to Region 3, the range noticed for the other curves.

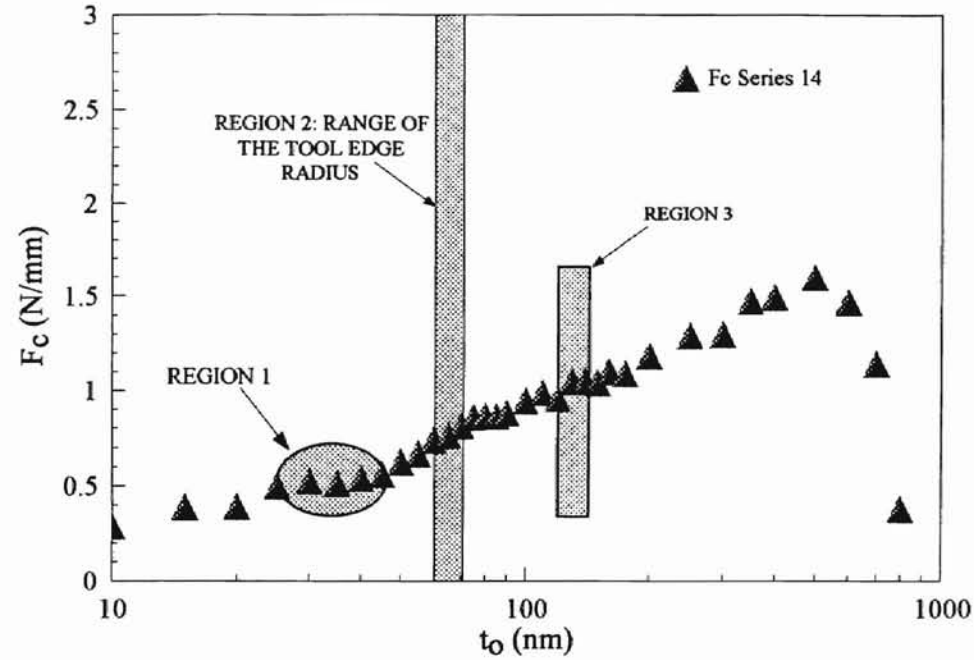

Figure 54. Cutting force curve for data series 14. This curve is in good agreement with the generalized cutting force curve. The major points of disagreement are that the tool edge plateau starts after the range of the tool edge radius and the third plateau is significantly off of the horizontal.

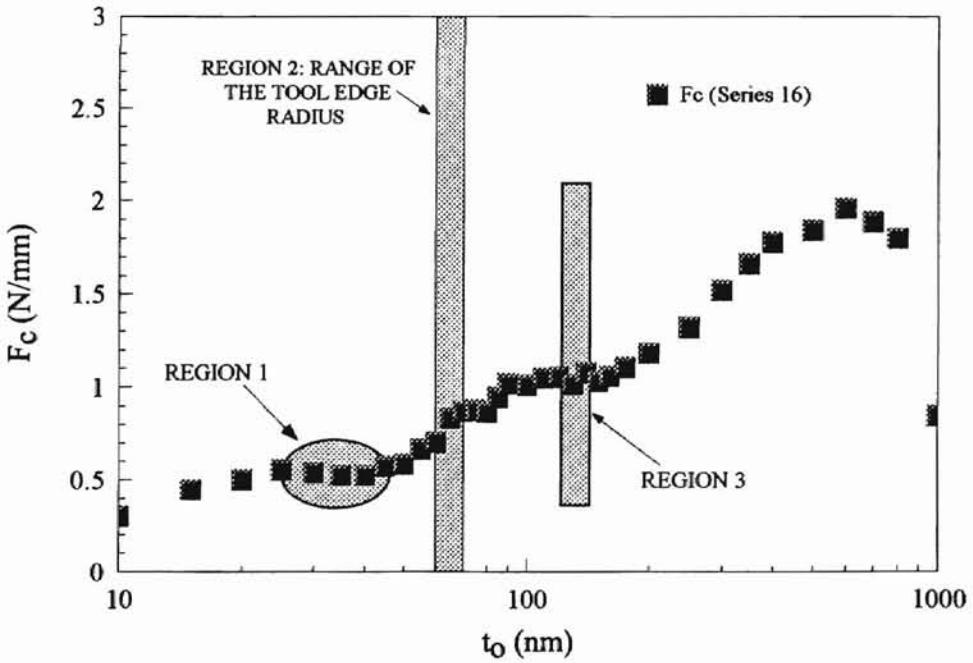

Figure 55. Cutting force data recorded for Series 16. This curve is in very close agreement with the generalized cutting force curve presented in Figure 52. The third plateau feature is most pronounced for this series and corresponds nicely to Region 3.

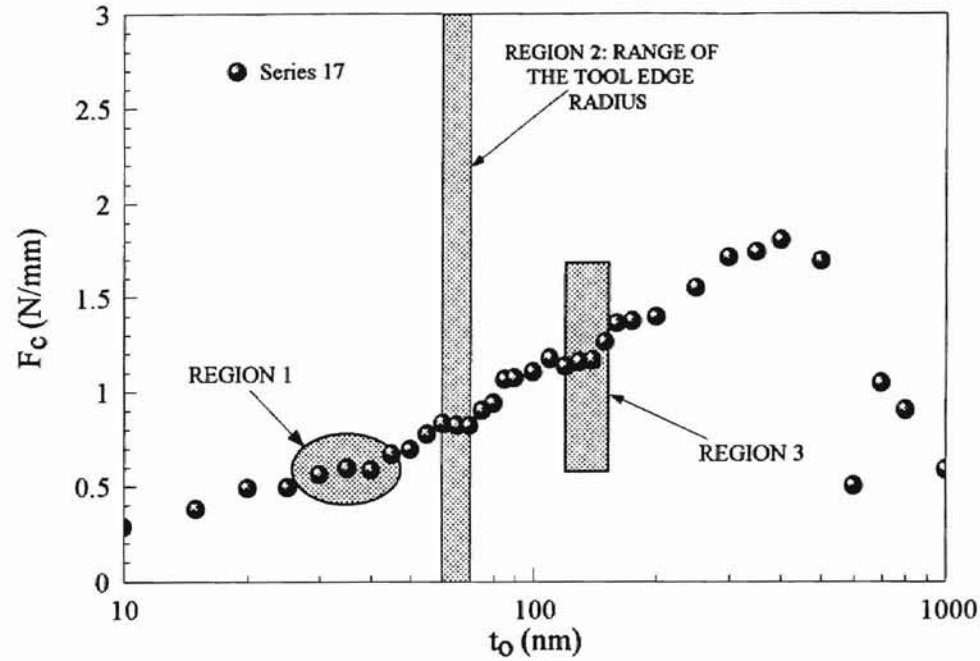

Figure 56. Cutting force curve for data Series 17.

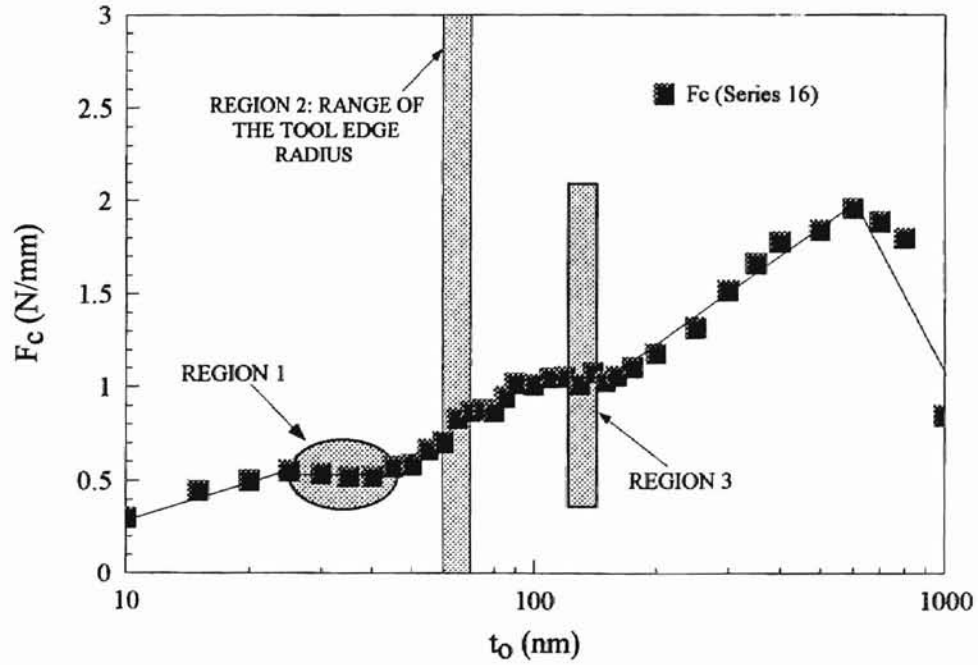

Figure 57. Comparison between an actual data curve and the generalized curve shown in Figure 52.

Thrust Forces

The following section of figures present the thrust force data for each series as compared to the size of tool edge features. The thrust force data is less consistent in the trends apparent from experiment to experiment, especially at the larger uncut chip thicknesses, than the cutting force data. The typical behavior is a steady generally linear increase up to approximately 30 nm which is followed by a plateau that typically extends to a t_o of approximately 45 nm, noted as Region 1. A discontinuity usually appears at the end of Region 1, at 40-45 nm, where either a slight change in slope or a jump in force level that starts another plateau feature occurs. The second plateau section, which is in some cases slightly angled, ends in another discontinuity in the vicinity of Region 2. After this point, the consistency between the curves from each experiment decreases. Generally, there is a roughly linear decrease in the magnitude of the force until Region 3, approximately 110-140 nm, where an inflection in the curve occurs. As noted previously, Region 3 corresponds to both the expected or estimated length range of the wear flat on the tool edge, as well as being twice the value of the radius of the tool edge. The last is significant since, as shown in Figure 38, this is the approximate range where global tool geometry should begin to dominate the cutting process. Region 3 is followed by either a leveling or a gradual increase in the curve force level. The final stage in the thrust force curve is a dramatic decline in force values.

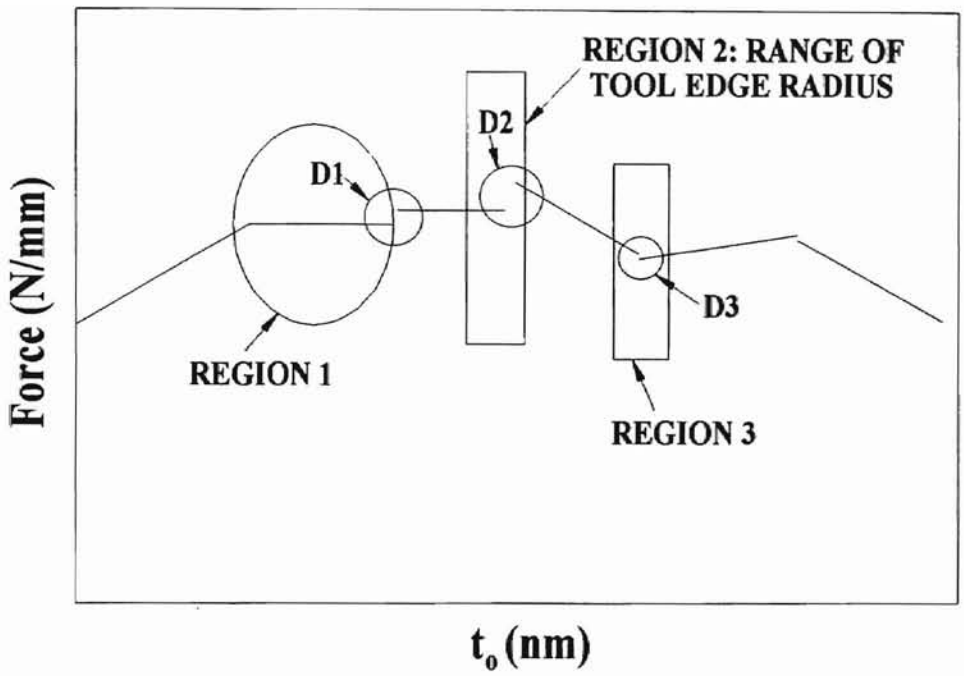

Figure 58. Generalized thrust force curve. Positions D1 and D2 represent discontinuities that typically occur at or about these points. D3 is the inflection point that occurs in Region 3 which corresponds to both the estimated wear flat length and a value twice the tool edge radius.

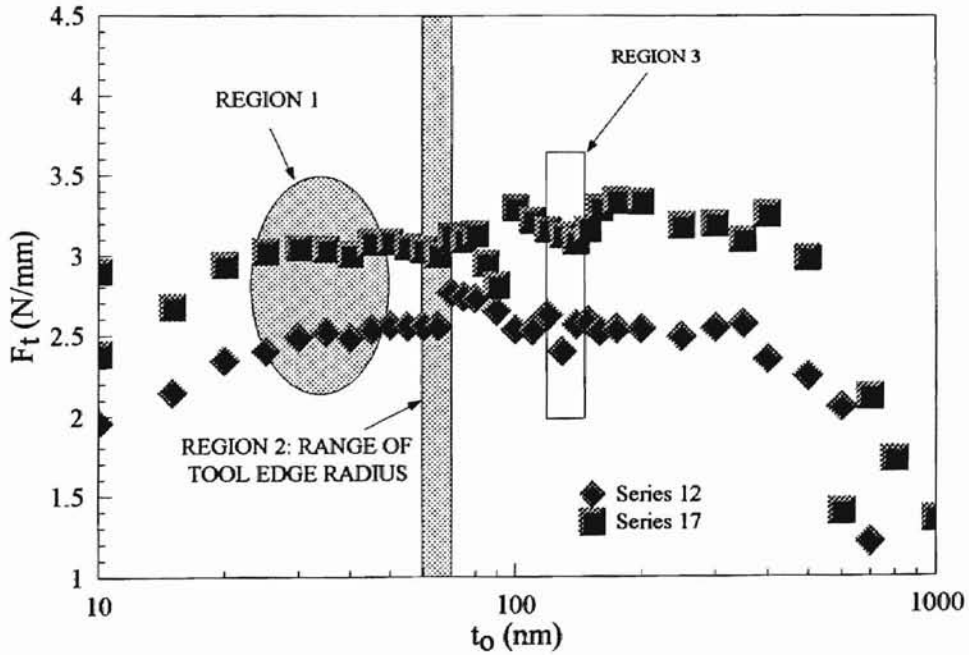

Figure 59. Comparison of the generalized thrust force curve with the thrust force curves from data series 12 and 17. The agreement between the actual and the generalized curve is generally good except at the higher uncut chip thicknesses where the trends are similar but the data is erratic.

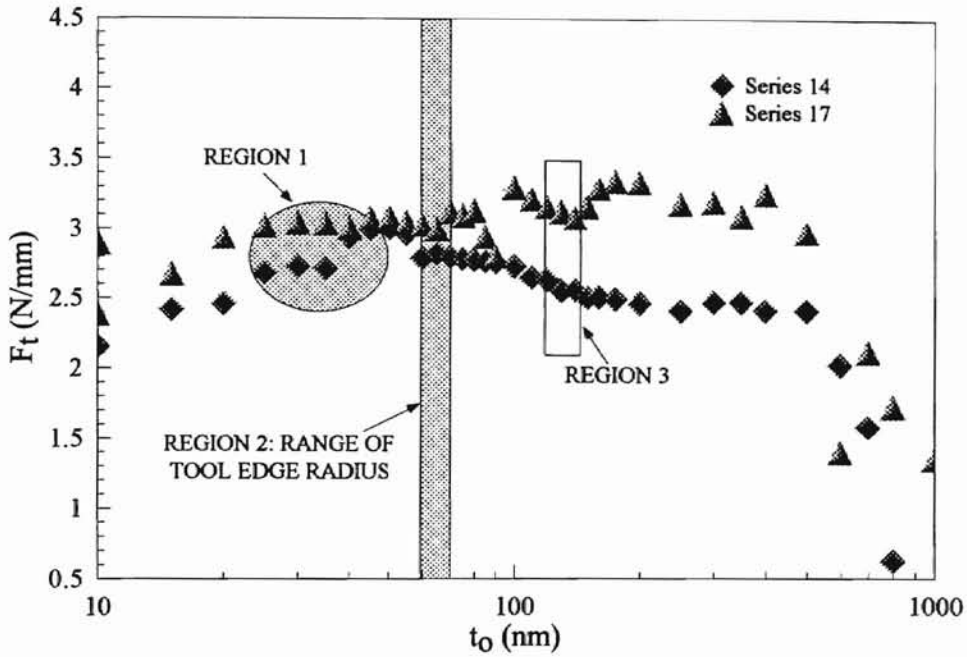

Figure 60. Thrust force curves for data series 14 and 17. Note the consistency of the l features noted in the generalized force curve.

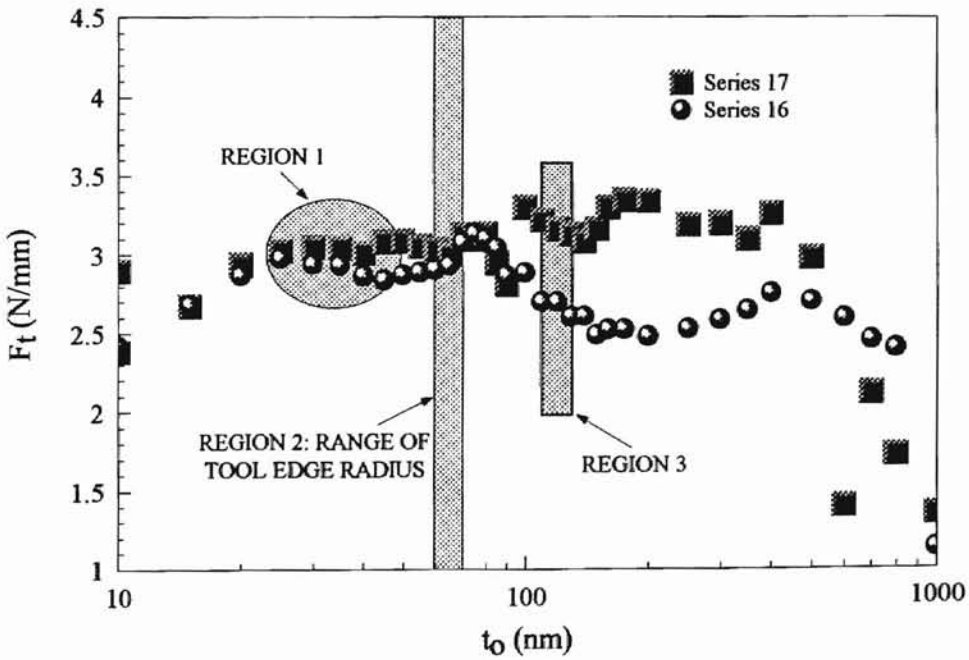

Figure 61. Comparison of thrust force data from series 16 and 17 as related to the size of feature of the tool edge.

Specific Energy and Force Ratio

The following data present the specific energy as a function of t_o and the size of features of the tool edge profile for each series of data. There is a dramatic increase in specific energy at small uncut chip thicknesses which is consistent with behavior seen in ductile materials.

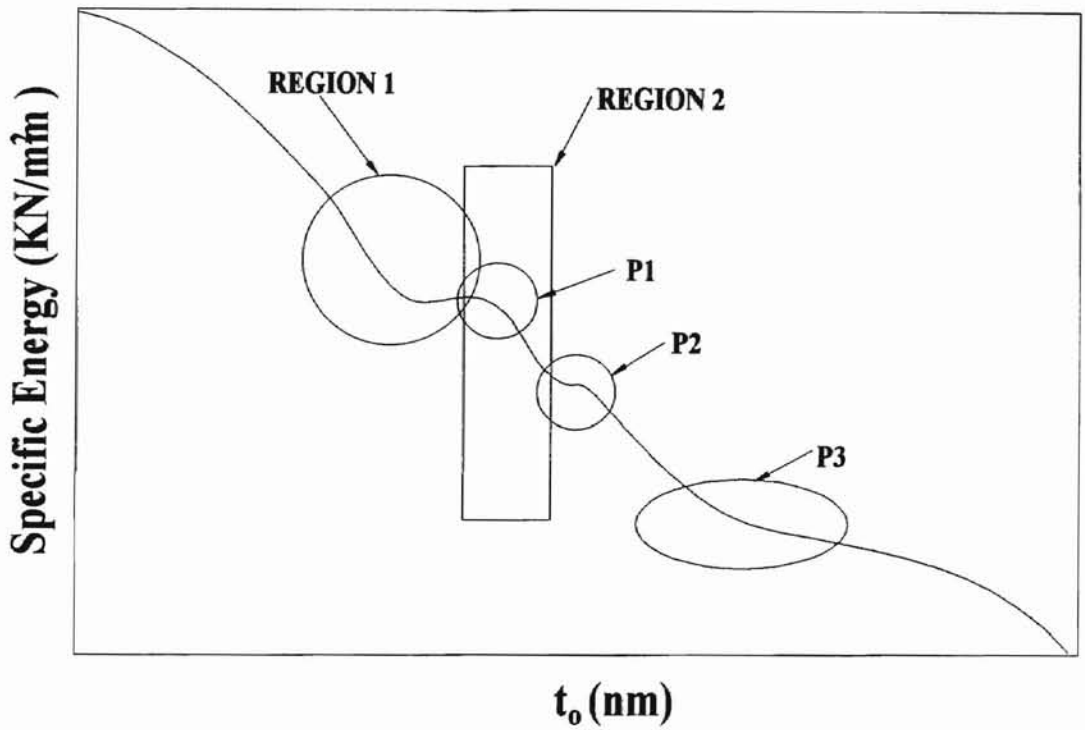

Figure 62. This is a generalized specific energy curve highlights the consistent features between the specific energy curves for data series 12, 14, 16, and 17. P1-P3 are features of interest. P1 occurs in the vicinity of Region 2, the range of the tool edge radius. P3 occurs in the range of 80-110 nm and P4 occurs at or about Region 3 which is approximately twice the value for the tool edge radius.

Comparison of the specific energy data curves from each experiment yielded the generalized curve features shown in Figure 62. The general data trends show a dip in the curve in the range of Region 1. Following Region 1 is a small plateau in the curve, noted as P1, which roughly corresponds to the range of Region 2. P2, which directly follows, is

a small discontinuity in the curve which occurs in the range of 80-100 nm. The final point of interest, P3, is an inflection in the curve which is closely associated with the range of Region 3. Each of these regions and events is evident in the data from each series, however, in some cases the curve appears to be slightly shifted to the right so that the events occur at the boundaries of the cited ranges (e.g. the curve for series 14 is shifted over slightly).

The following plots show the specific energy curves for data gathered during experiments 12, 14, 16, and 17. The various events noted in the general specific energy curve are pointed out in each plot, as well as the size ranges for characteristics of the tool edge.

Comparisons between specific energy data presented in Chapter 4 and reported in the literature, both for ductile materials [Seo, 1993] and polycrystalline Ge [Furukawa, 1988], are made in Figure 67. At low uncut chip thicknesses, the behavior between the tellurium copper curve and the curves reported here is very similar. At almost every point in the reported range, the specific energy for experiments 12, 14, 16, and 17 is greater than that reported by Seo for Te-Cu. Comparison, between the data for polycrystalline Ge reported by Furukawa and the specific energy for the single crystal Ge reported here, shows a similar trend, with the specific energy for the polycrystalline material being typically lower.

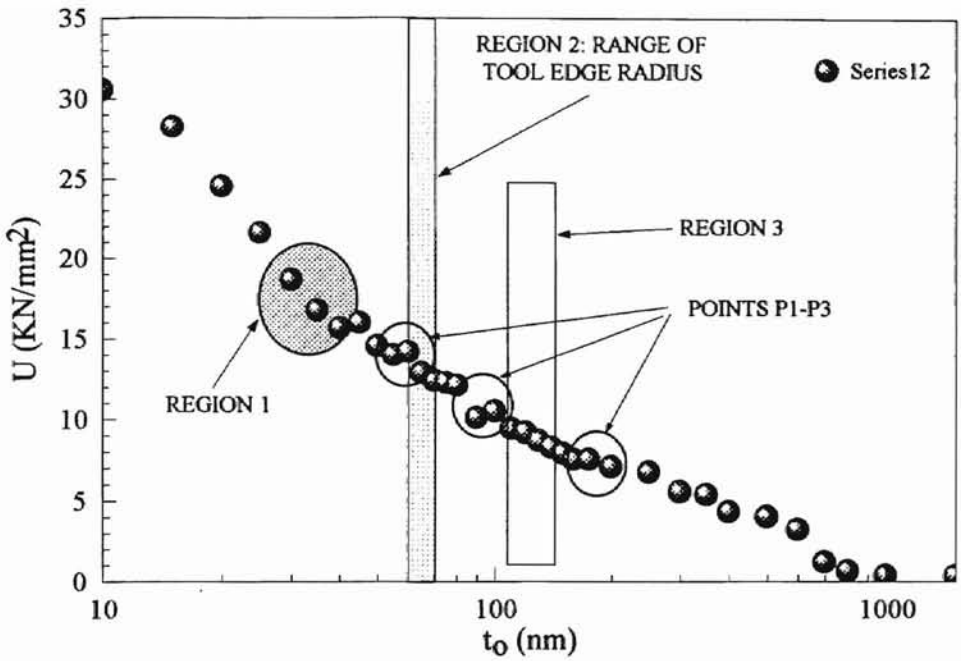

Figure 63. Specific energy curve for data series 12. Note that many of the curve characteristics are not well established. Of the curves from each series this one is in least agreement with the generalized curve shown in Figure 62.

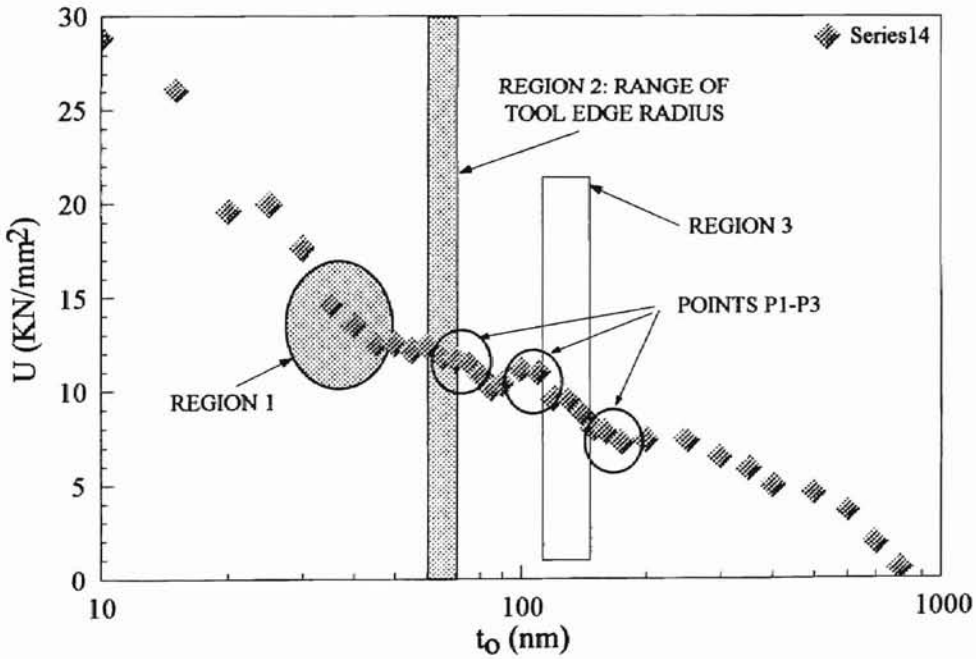

Figure 64. Specific energy curve for data series 14. This curve is in good agreement with the generalized curve except for being slightly shifted to the right such that many of the features occur approximately 10-20 nm to the right of where those same events occur in other curves.

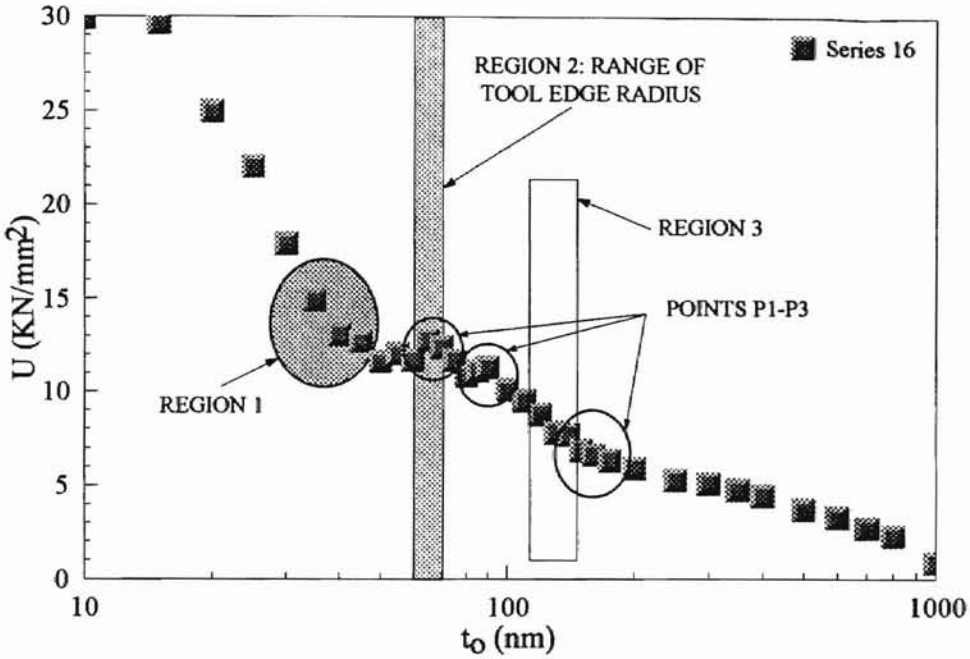

Figure 65. Specific energy curve for series 16. This curve is in excellent agreement with the generalized curve. P3, the inflection point near Region 3, implies changing behavior in the process. That it occurs at a t_o approximately twice the size of the tool edge radius suggests that the this may be where the global tool geometry begins to dominate over the local edge geometry.

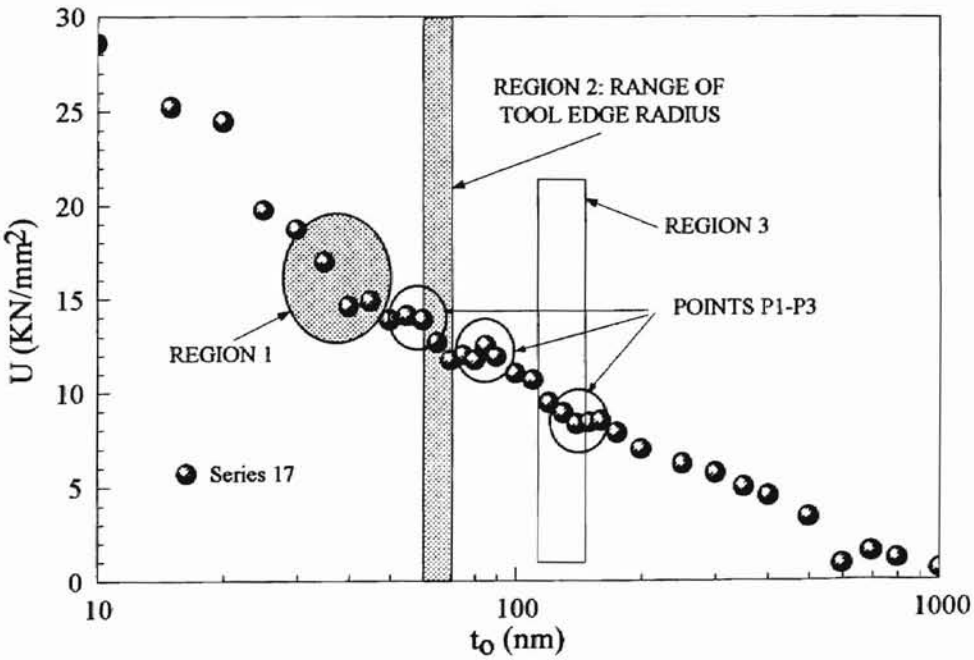

Figure 66. Specific energy curve for data series 17 as compared to the size of features of the tool edge profile. This curve is in good agreement with the generalized curve.

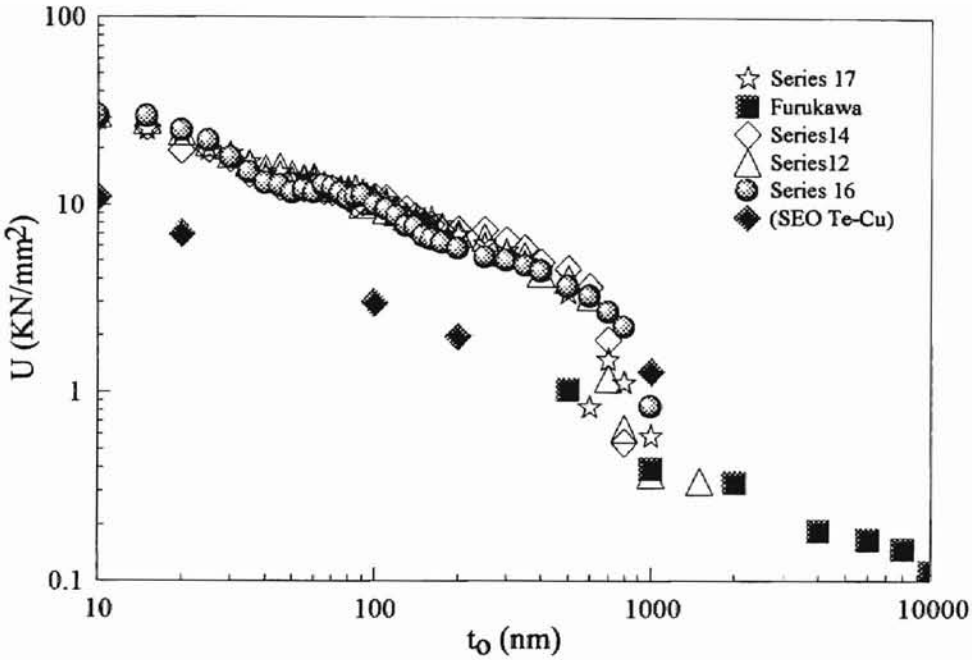

Figure 67. Comparison between specific energy curves from each experiment with those reported by Seo [1993] for ductile materials and Furukawa [1988] for Ge.

The generalized force ratio curve illustrates the features consistent between the various experiments. As has become the typical case, many of these features coincide with the size of attributes of the tool edge profile. The initial stage is a sharp decline in the force ratio that tapers off to a plateau (Region 1) which is followed by a continuing decline in the magnitude of the force ratio. This decline stops in Region 2, the region corresponding to the range of the tool edge radius. Here, the slope of the curve becomes positive, briefly, before declining again. The curve continues on a tapering decline which ends in a slight increase. A discontinuity in the curves is evident in Region 3 where a slight step is usually noticeable.

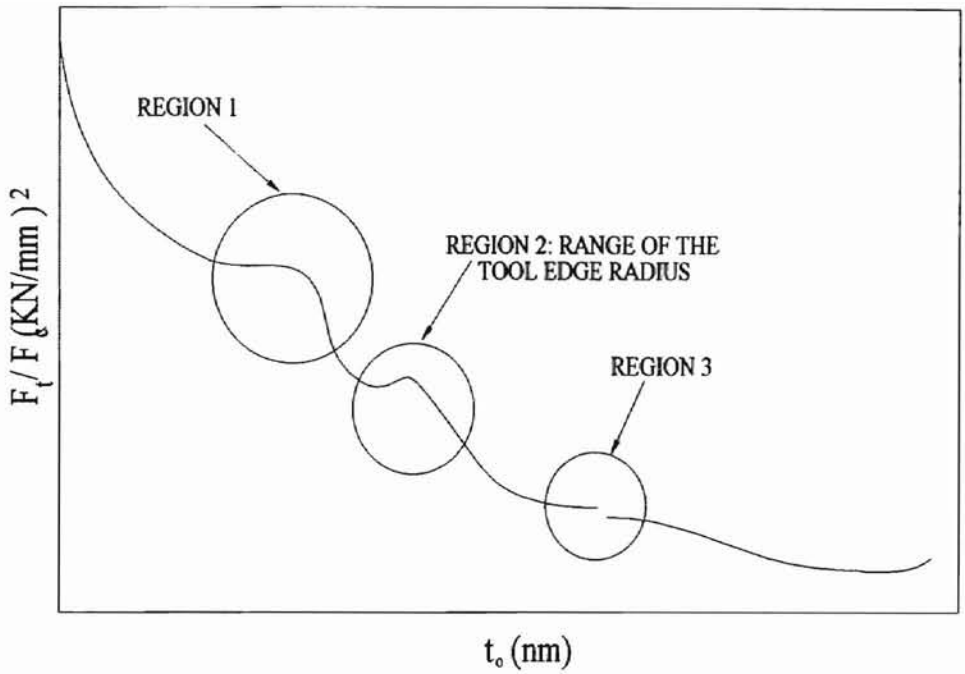

Figure 68. Generalized force ratio curve showing the features most consistent between curves from experiments 12, 14, 16, and 17. As has become typical there are definite features at points corresponding to the size of tool edge features.

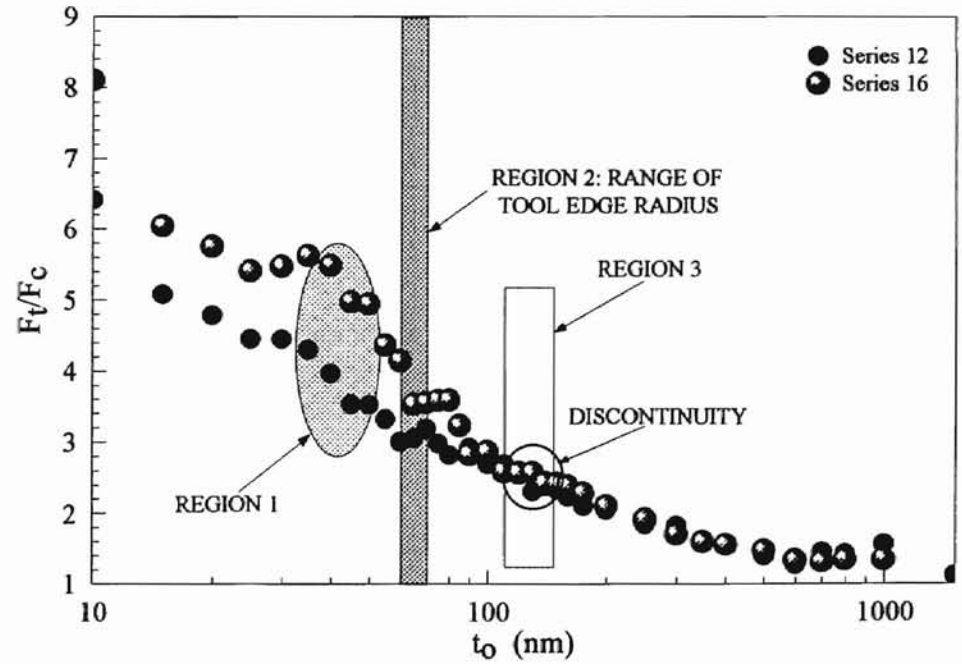

Figure 69. Force ratio curves as functions of uncut chip thickness for data series 12 and 16. Here the curves are compared with the size of features from the tool edge profile. There is excellent agreement between these curves and the generalized force ratio curve even to the location of the discontinuity which occurs in Region 3.

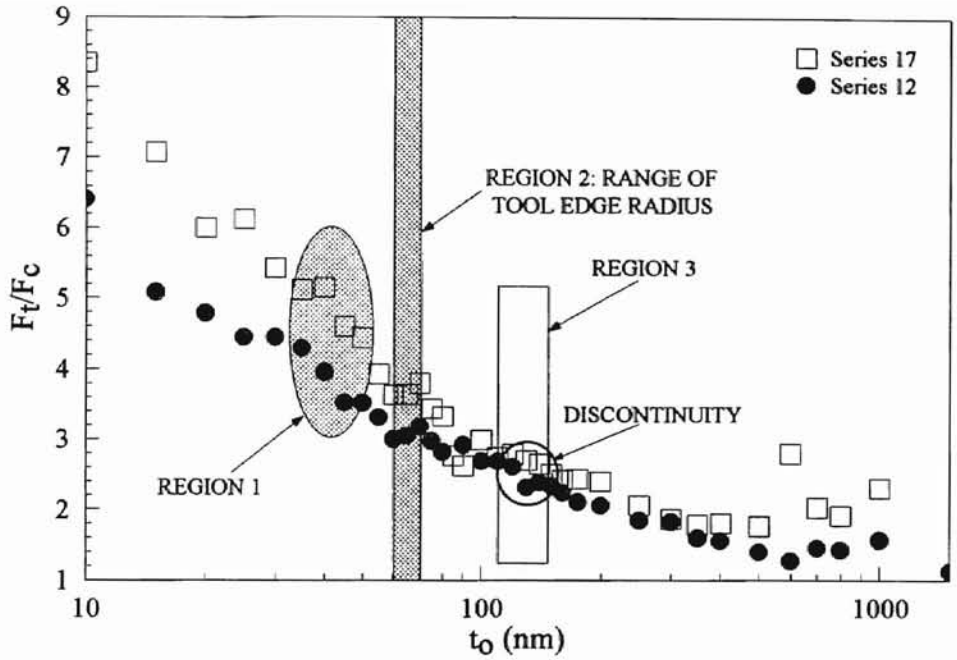

Figure 70. Force ratio curve for data series 17 and 12 as functions of tool edge features as well as the uncut chip thickness. The curve for series 17 is the most erratic of the four experiments and as a result it has the least agreement with the generalized force ratio curve.

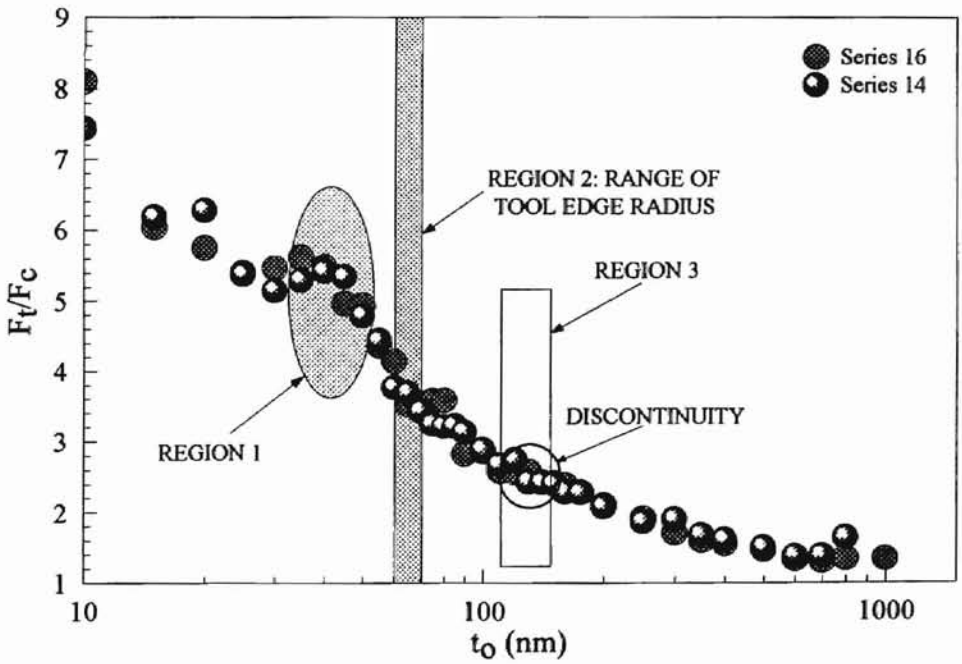

Figure 71. Force ratio curves for data series 14 and 16 as compared to features from the tool edge profile. Here again there is considerable concordance not only between the curves but also with the generalized force ratio curve.

Morphologies of the Chip and Surface

Comparisons of some representative force data with the size of tool edge features, as well as ranges of surface and chip forms, are presented in Figure 72 and Figure 73. The first of these compares thrust force data from series 12 and 17 with tool edge features and the ranges of chip types. The mixed chip region extends from the end of Region 1 to the approximate range of Region 3, 110-150 nm. Figure 73 illustrates the comparison between surface quality, tool edge features, and the force ratio curves from series 12 and 16. Here, it is shown that the mixed surface region extends from the end of Region 1 to a point just after Region 2 at approximately 90 nm. In both cases, mixed regions begin at the approximate point where Region 1 ends and encompass the tool edge range.

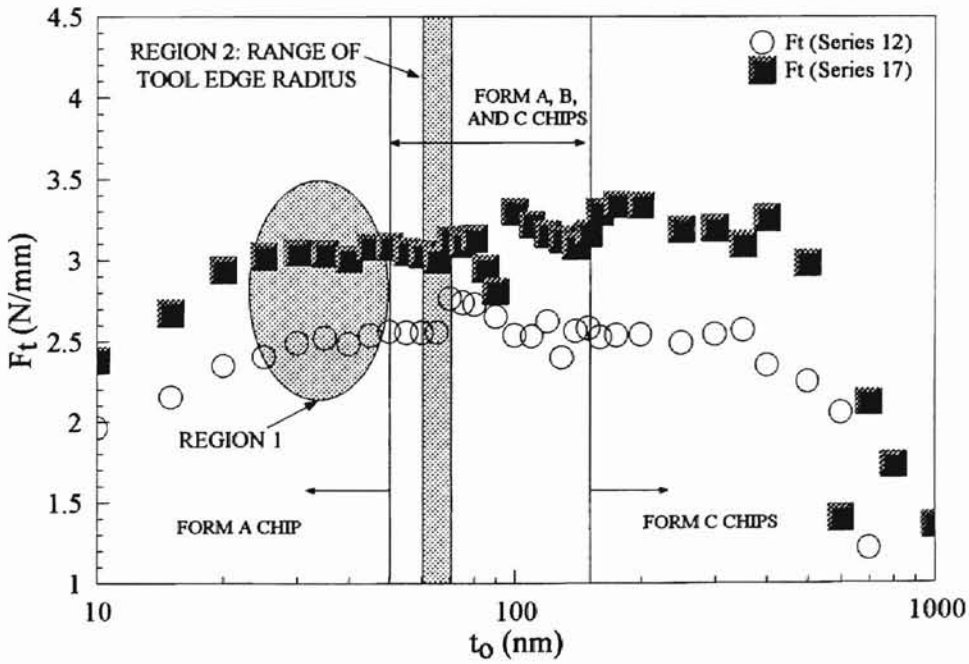

Figure 72. Comparison of thrust force data with features of the tool edge and ranges of chip morphologies. The mixed chip region starts at the end of Region 1 and ends at approximately within the range of Region 3.

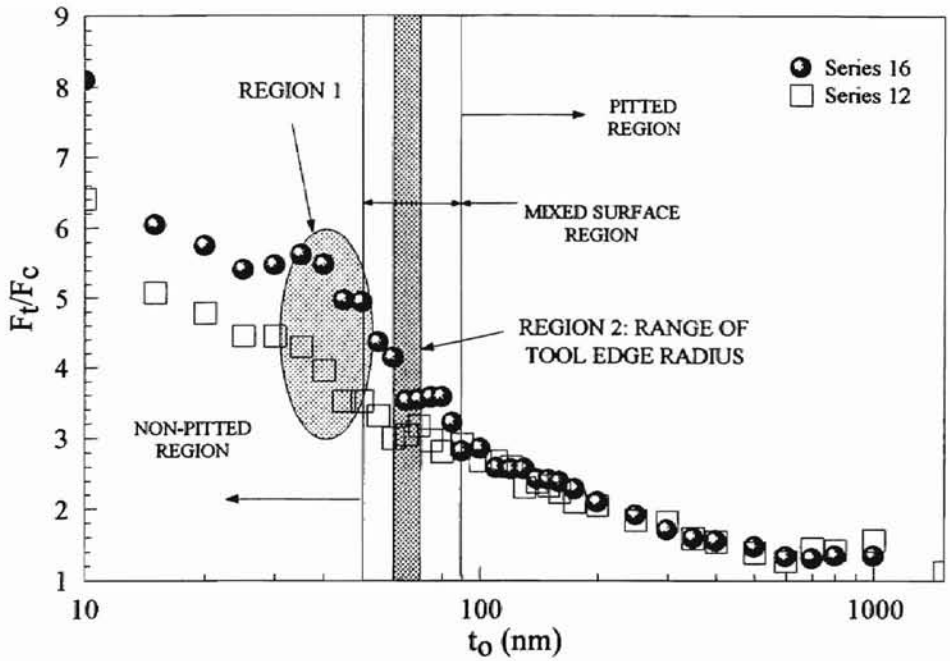

Figure 73. Force ratio curves as compared to the different regions of surface quality and the size of features from the tool edge profile.

Vita

Charles Babcock

Candidate for the Degree of

Master of Science

Thesis: ENERGY DISSIPATION IN ORTHOGONAL ULTRAPRECISION MACHINING OF GERMANIUM

Major Field: Mechanical Engineering

Biographical:

Personal Data: Born in Norman, Oklahoma, on January 18, 1967, to Mrs. Susan Babcock and Mr. Terry Babcock.

Education: Graduated from Douglass High School, Oklahoma City, Oklahoma in May 1985; received Bachelor of Science degree in Mechanical Engineering with a minor in Mathematics from Oklahoma State University, Stillwater, Oklahoma in July 1992. Completed requirements for the Master of Science with a major in Mechanical Engineering at Oklahoma State University in July 1995.

Experience: Employed by Oklahoma State University Mechanical and Aerospace Engineering Department as an undergraduate and graduate teaching assistant for Material Science and as a graduate research assistant 1991-1994. Performed as substitute lecturer for Mechanical Metallurgy and Manufacturing Processes 1994.

Professional Memberships: American Society of Mechanical Engineers 1990-present, Pi Tau Sigma Mechanical Engineering Honors Fraternity 1990-present.